GRAPHENE OPTOELECTRONICS FROM THE VISIBLE TO THE MID-INFRARED

By:
Michela BADIOLI

Supervisor:
Professor Frank H. L. KOPPENS

UNIVERSITAT POLITÈCNICA DE CATALUNYA

ICFO - THE INSTITUTE OF PHOTONIC SCIENCES
Nano-Optoelectronics Group
2015

Alle mie nonne.

Acknowledgements

It is truth universally acknowledged that si vols fer experiments, cal entrar al laboratori. Doncs, moltes gracies a Monica, Mercè i Maria Jose que somrient m'han canviat la targeta per entrar a ICFO casi cada matí: segur que sense no podría haver fet cap experiment! A big thank you goes also to all the ICFO units that make everyday life easier in any aspect, in particular to Santi, Magda y Elena, Adrià y Jonas, el omnipresente Carlos, los chicos de los mechanical y electronics workshops, y los recursos humanos.

I would like to thank Frank for his outstanding intuition for intriguing scientific projects and for the constant drive towards achieving good results. Also, he managed to set up an awesome team that I literally saw growing from the birth. Great people to discuss physics, and have several drinks. Many thanks to all the past and present members of the NOE group, in particular to Sebastien, Peter, Stijn, Mathieu, Mark, Romain and Francisco. Thanks to Louis who guided me on the first measurements of the PhD ("l'hai rotto??") and could tell my mood just by one look while crossing the corridor; to Klaas, probably my favourite person to discuss science and sailing with; to Marko, our medusas on the wall were among the funniest moment of my PhD; to Achim, the best companion of many long days in the lab and many more beers; to Gabi, days were brighter with our girly afternoon teas after a long time spent working in the clean room (and cleaning up the boys' mess!); to my lieutenant Ivan, who is going to give me a rose for Sant Jordi now? To Antoine, tactful listener always with the best advice, from how to approach the thesis writing to the coolest concerts in town; and to Kevin, who manages to put a smile on the grumpiest face.

Among the many people I collaborated with, a special thank goes to Javier for the stimulating discussions and to Tobias for his extraordinary availability, patience and detailed explanations.

I am really indebted to my "clean room angels" for their help, support and friendship. Grazie a Davide per essere stato come un fratello maggiore; e a Johann per le risate, i pranzi in spiaggia e per essere la mia bibbia del barri d'Hostafrancs.

Ha sido genial cruzarse en el pasillo, en la sala blanca y más bien en el Raval con los chicos de los pasillos amarillo y naranja: Marta, Daan, Riccardo, James, Anshu, Pablo, Alex, Michael (todavía tenemos pendiente las clases de surf), Jan R., Esteban, Mariale, Jon, Pelayo (grapheeeene), Dominik, Fabian, Miriam, Marc, Luis y Javier.

El tiempo en ICFO no habría sido lo mismo sin Fede (que siempre consigue convencer a la gente a hacer algo ridículo ...), Gonzalo (... feliz de hacer algo ridículo), Nadia y Philipp (meine lieben Tänzer), Pablo y Elsa (los mejores compañeros para viajes last-minute), il capitano Anna, Carlo, Alessio, Alejandro, Candan (never mind I'll find someone like youuuuuu), Giacomo.

Nunca podría haber acabado el doctorado sin la compañía de todos los amigos conocido en estos años en Barcelona. Grazie ad Ari che mi ha dato il benvenuto in città, a Nat e Fra che mi fanno sentire a casa. Gracias a Maria y Gio por haber sido mi familia, con cenas, risas y critos ... y más risas y más critos ... y todavía más risas! Muchísimas gracias a todos Los Italianos® and Friends de todos los tiempos: Francesco (chissà com'è "l'assorzione" del sole in Danimarca), Nicolò (il migliore per ridere e piangere, deh!), Mauri (ubi maior ...), Gianvito (daje Roma daje), Stefania, Nicola, Constantina, Fabio (mi querido perroflauta fan de Raffaella), Emanuele il saggio (se non gioca la Juve), Michele (il mio orgoglio nei mari), Furbish (ovvero l'energia dei gggiovani), Roberta, Nello, el grande Falk, Thomas, Paco y Carlos.

During the years in Barcelona it was always nice to get fresh energies going home or visiting friends abroad. Thanks to Anna, Toney, Silvia, Sakeena, Shane (the guy who suggested to come to ICFO). Grazie ai romani, sempre presenti anche solo per un breve saluto, Matteo, Alessandra, le galline, i gab-

biani (!!!). Grazie anche a Valeria e Michele che hanno reso piacevoli questi mesi da post-doc non proprio doc. Ma soprattutto grazie alla mia famiglia, e ai miei splendidi genitori che mi hanno sostenuto in questi anni da lontano e da vicino, ascoltando le mie chiacchiere sul grafene, studiando spagnolo e arrivando a conoscere la città quasi meglio di me.

Finally, I am much obliged to the people that helped proof-reading the thesis: Anna, Achim, Alex, James, Toney, Tom, Kevin, Mark (who got the joke in Chapter 9).

Contents

Preface

Just five days after the beginning of my PhD, A. Geim and K. Novoselov were awarded the Nobel prize in Physics "for ground-breaking experiments regarding the two-dimensional material graphene". This great news boosted my enthusiasm as I was starting to work with such extraordinary material in a research field completely new to me. Indeed, since its discovery in 2004 graphene has attracted huge interest from the scientific community due to its unique electronic, mechanical, and optical properties.

The application of graphene remarkable properties and the rapid development of graphene-based devices paves the way to the birth of disruptive new technologies. The innovative power and the highly technological relevance of graphene research has fuelled the birth of several graphene research centres around the world and has been acknowledged by the European Union (EU). The EU invested the unprecedented sum of 1 billion euros in the Graphene Flagship, a 10 year project started in October 2013, with the collaboration of research institutions and industrial partners on a multidisciplinary basis, The aim of the Flagship is to bring graphene-based technology, where an important role is played by the optoelectronics applications, from academia to products of everyday-life.

Indeed, while most of the earliest studies focused on electronic transport, in recent years the fields of graphene photonics and optoelectronics have thrived. Graphene tunable optoelectronic properties, high electronic mobility, broadband absorption and flexibility make it extremely appealing for the development of graphene-based optoelectronics with new functionalities.

The goal of this thesis is to explore the use of graphene for novel optoelectronic devices, adopting different approaches to enhance the electrically tunable graphene-light interaction in a broad spectral range, from the visible to the mid-infrared. This includes the investigation of the sub-wavelength interaction and energy transfer between a dipole and a graphene sheet, as well as the development of efficient photodetection schemes.

We address both aspects at the core of optoelectronics, i.e. the control of optical properties with electric fields and the modification of electrical quantities, such as current, with light. Therefore the first part of the thesis (comprising Chapter 3, 4 and 5) is devoted to **graphene nanophotonics and plasmonics**, while the second part deals with **graphene-based photodetection** (Chapter 6, 7, 8 and 9).

Outline of this thesis

In **Chapter 1** we describe graphene tunable optoelectronic properties, which make it extremely appealing for the development of optoelectronic applications with new functionalities.

Concerning the devices, the starting point of the experiments presented in the thesis are graphene field effect transistors of different geometries, whose fabrication and characterization techniques are described in **Chapter 2**. The tunability of the optoelectronic properties via control over the Fermi energy is an essential feature of the fabricated devices. The change in the Fermi level is achieved applying a voltage to a back-gate or a polymer electrolyte top-gate.

In **Chapter 3**, the main concepts at the basis of graphene nanophotonics are presented, such as the electrical tunability and the strong field confinement of the 2D plasmons, as well as the coupling of an optical emitter to graphene plasmons or electron-hole pair excitations. Then we present two experiments showing the control of light by means of static electric fields. In **Chapter 4** we show the electrical control of the relaxation pathways of erbium ions in close proximity to a graphene sheet: the energy flow from the emit-

ters is tuned to electron-hole pairs in graphene, to free space photons and to plasmons by changing the graphene Fermi level. In **Chapter 5** we present the real-space imaging and tuning of highly confined graphene plasmons in the mid-infrared, launched by the dipole of a metallized s-SNOM tip. In this case modifying the graphene Fermi level leads to a change in the plasmon wavelength.

In **Chapter 6** we review existing schemes for graphene photodetectors and the main mechanisms enabling photodetection with graphene, with particular emphasis toward the photothermoelectric effect. Then we present three cases where graphene photoresponse is enhanced exploiting the interaction with surrounding materials. A hybrid graphene-quantum dot photodetector in the visible and near-infrared is reported in **Chapter 7**: a photogating effect after light absorption in the quantum dots leads to extremely high responsivities (over one million A/W). In **Chapter 8** we demonstrate how the excitation of bulk phonons of a polar substrate enhances the mid-infrared photocurrent via a photothermoelectric effect. Also substrate surface phonons, launched by illuminating a metal edge with light polarized perpendicularly to it, lead to an increase in the photoresponse, as described in **Chapter 9**.

Finally, we conclude discussing how the results presented in this thesis open new avenues in the field of graphene-based optoelectronics for active nano-photonics and light-detection.
In the **Appendix A** some of the most used fabrication recipes are reported.

1

Graphene basics

In this Chapter we review the basic concepts concerning graphene tunable electronic and optical properties needed to understand the experimental results presented in the following chapters. We start from the peculiar band structure of graphene and the implications of its linear dispersion relation. Then we discuss some important features regarding its transport properties, the minimum conductivity and the mobility. In the following section we treat the optical properties. In particular we describe the experimental results for the absorption of doped and undoped graphene, and present the main concepts concerning the optical conductivity.

Graphene is a one-atom thick sheet of sp^2 hybridized carbon atoms arranged in a honeycomb lattice. It has been studied theoretically since the middle of the 20th century as the building block to derive the band structure and properties of graphite and other allotropes of carbon with sp^2 hybridization, such as carbon nanotubes [Wallace, 1947; Slonczewski & Weiss, 1958; Reich *et al.*, 2002]. However, its existence as a material on its own was for a long time not considered to be possible, as thermodynamic fluctuations would hinder the stability of strictly 2D crystals [Mermin, 1968].

Nevertheless in 2004 the Nobel Prize winners Geim and Novoselov managed to isolate a single layer of graphene deposited on an oxidized silicon substrate by mechanical cleavage of graphite[1] and to use it as the channel for an ambipolar field effect transistor (FET) [Novoselov *et al.*, 2004], immediately attracting huge interest and fostering tremendous work on the extraordinary properties of this novel material [Geim & Novoselov, 2007]. Experimental and theoretical studies later showed that also unsupported graphene is stable, as it rearranges with ripples in the third dimension [Fasolino *et al.*, 2007; Meyer *et al.*, 2007].

1.1 Electronic properties

A complete review of the electronic properties of graphene and bilayer graphene can be found in Castro Neto *et al.* [2009] and Das Sarma *et al.* [2011], while here we report the main results concerning the band structure and the transport properties.

Band structure

The band structure of graphene is obtained from a tight binding calculation on the out-of-plane *2pz* orbitals [Wallace, 1947]. The hexagonal lattice is treated

[1] Now different techniques of graphene production are available, and a review of the ones relevant for opto-electronics applications is presented in Chapter 2.

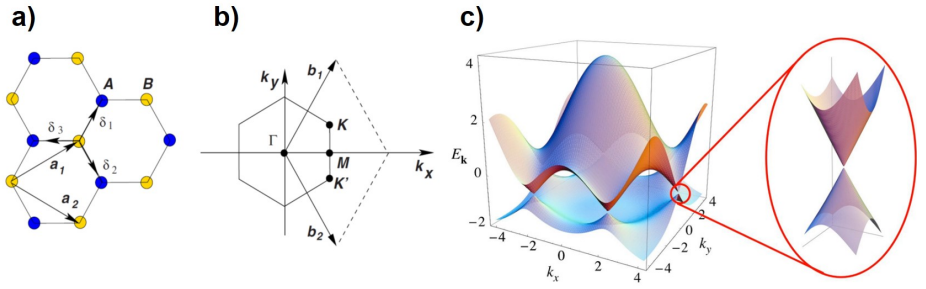

Figure 1.1: a)Hexagonal lattice in real space, the Bravais lattice is triangular with two atom base (in blue and yellow); b) corresponding Brillouin zone; c) full dispersion from tight binding calculation with t=2.7 eV and t'= -0.2t (the asymmetry between valence and conduction bands is introduced by a non-zero value of t'), and zoom on the low energy region at the K point. Figure from Castro Neto *et al.* [2009]

as triangular Bravais lattice with a two atom base (Fig. 1.1a). While the distance between the atoms is $\delta = 1.42$ Å, the lattice constant is a= 2.46 Å.
The electrons can hop to nearest-neighbours (i.e. to a different sublattice, shown in different colour in Fig. 1.1a) with an hopping energy $t \approx 2.8$ eV and to next-nearest-neighbours (i.e. to the same sublattice) with an hopping energy $t' \ll t$.

The full band structure is shown in Fig. 1.1c. Conduction and valence band touch, but only at the **K**$(2\pi/3a, 2\pi/3\sqrt{3}a)$ and **K'**$(2\pi/3a, -2\pi/3\sqrt{3}a)$ points[2] of the Brillouin zone, that is sketched in Fig. 1.1b. Graphene is then considered as a semiconductor with no band-gap, or a semi-metal with no band overlap. If no external perturbation is present, at temperature ϑ=0 K, the Fermi level is exactly at the touching point (also called Dirac point) between valence and conduction band.

The full band can be expanded for values of the **k** vector around the **K** and **K'** points, introducing $\mathbf{q} = k - K$. For $\mathbf{q} << K$, the bands become $E_\pm \approx \hbar v_F |\mathbf{q}|$, where $\hbar v_F = \sqrt{3} t a/2$, and the Fermi velocity is constant: $v_F \approx 10^6$ m/s. Hence

[2]The equivalence of the band structure in these points is referred to as the valley degeneracy.

the valence and conduction bands are approximated by two cones, as shown in Fig. 1.1c.

The fact that the energy dispersion is linear at low energies (up to ~ 1 eV) means that charge carriers behave as a 2D gas of massless particles, i.e. carriers dynamics is described by the Dirac equation for massless particles. Remarkably, an additional charge density n results in a square-root change in the Fermi level with respect to the value at the Dirac point:

$$E_F = \hbar v_F \sqrt{\pi n} \tag{1.1}$$

as opposed to the case of bilayer graphene (whose band structure can be considered parabolic for very low energies) and other two-dimensional electron gases (2DEG) where $E_F \propto n$. The square root dependence was observed measuring the graphene cyclotron mass, and together with the observation of the half-integer quantum Hall effect proved the presence of 2D Dirac fermions in graphene [Novoselov *et al.*, 2005a; Zhang *et al.*, 2005].

Transport properties

Thanks to the two-dimensionality and the gapless nature of the dispersion it is possible to change the number of charge carriers (i.e. to dope the graphene) by the electric field effect[3], adding either electrons or holes to the system, as sketched in Fig. 1.2b. In this way it is possible to tune the electrical (and optical, as explained later) properties of a graphene device. The simple case of the resistance as a function of charge carrier density is shown in Figure1.2a.

We note that at the Dirac point, or charge neutrality point (CNP), there is still conduction, hampering the use of graphene for DC transistors. This is still the case at low temperatures, with experimental values of the conductance minimum on the order of $\sim e^2/h$, and the proportionality factor depending on the specific sample[4] [Tan *et al.*, 2007].

[3] Practical implementations will be presented in the next Chapter.

[4] We note that the theoretical value of the conductivity in the zero frequency limit is not uni-

Importantly we should consider the fact that, at least locally, the charge density never vanishes completely, so the transport close to the Dirac point is due to electron-hole puddles [Martin *et al.*, 2007]. Their distribution has been shown to be related to the substrate by scanning tunnelling microscopy (STM) measurements, with local charge fluctuations of graphene on flat hexagonal boron nitride (hBN) being much smoother and less intense than the charge fluctuations of graphene on SiO_2 [Xue *et al.*, 2011]. However, also for suspended graphene charge puddles have been predicted due to the intrinsic corrugations [Gibertini *et al.*, 2012].

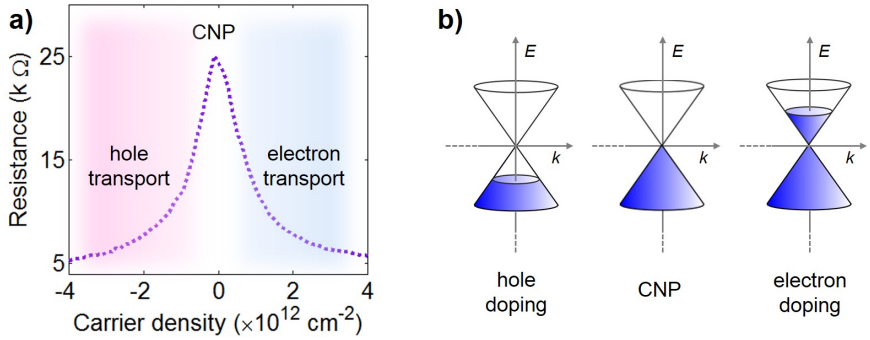

Figure 1.2: a) Resistance of a graphene FET as a function of charge carrier density, showing the ambipolar behaviour. The charge neutrality point (CNP) is also referred to as as the Dirac point or the Dirac peak when considering the resistance curve. b) Graphene linear energy-momentum dispersion (Dirac cones) with different band filling.

versal. It depends on which order certain limits are taken, and on the assumptions on the disorder, even when the same type of calculation of the linear response is implemented [Ziegler, 2007]. Indeed the predicted high frequency conductivity σ, which is frequency independent, and the DC conductivity obtained by starting with the zero frequency limit are different. They are respectively $\sigma = \frac{\pi e^2}{2h} = \frac{e^2}{4\hbar}$ and $\sigma_{DC} = \frac{4e^2}{\pi h}$. Instead, most of the early electrical measurements of the minimum conductivity on good quality samples yielded values closer to $\frac{4e^2}{h}$, suggesting the idea of the minimum of conductance being related to two quanta of conductance. This gave rise to a much discussed debate, the so-called mystery of a "missing pie" [Geim & Novoselov, 2007]. However, a really universal value has not been found experimentally for σ_{DC}.

Thanks to high crystallinity and to the low scattering rate between electrons and intrinsic phonons [Hwang & Das Sarma, 2008; Chen *et al.*, 2008] graphene can exhibit values of the mobility at room temperature far beyond the ones of standard 2D semiconductors and 2DEG, up to the recently demonstrated value of 140000 $cm^2V^{-1}s^{-1}$ [Wang *et al.*, 2013], on a device encapsulated between 2 layers of hBN. However, on the common SiO_2 substrate scattering with the substrate surface phonons limits the mobility to a maximum of $\sim 4 \times 10^4$ $cm^2V^{-1}s^{-1}$ at room temperature in UHV [Chen *et al.*, 2008], while the values in air are lower, typically on the order of few thousands $cm^2V^{-1}s^{-1}$ for the devices used in the experiments presented in this thesis.

1.2 Optical properties

Graphene possesses very interesting optical properties. First of all, the gapless electronic spectrum leads to a very broadband absorption. Furthermore, the tunability of the Fermi energy is reflected in a tunable optical conductivity.

Universal absorption of graphene and 2D systems

As shown in Fig. 1.3a, the optical absorption of undoped suspended graphene has been measured to be 2.3% across visible and near-infrared (NIR) illumination [Nair *et al.*, 2008], This is a very remarkable value for a one-atom thick material, but what is more intriguing is that this value does not depend on material parameters, as it is defined solely by universal constants, i.e. $\pi\alpha$, where α is the fine structure constant ($\alpha = \frac{e^2}{4\pi\varepsilon_0\hbar c} \approx \frac{1}{137}$).

We note that the value of the absorption $\pi\alpha$ is observed with small corrections up to photon energies above the validity of the linear approximation for the dispersion, but it becomes ~ 4 times higher in correspondence with the excitonic peak at the band saddle point at 4.6 eV [Mak *et al.*, 2011]. For few layer graphene (FLG) the absorption grows linearly increasing of $\pi\alpha$ per

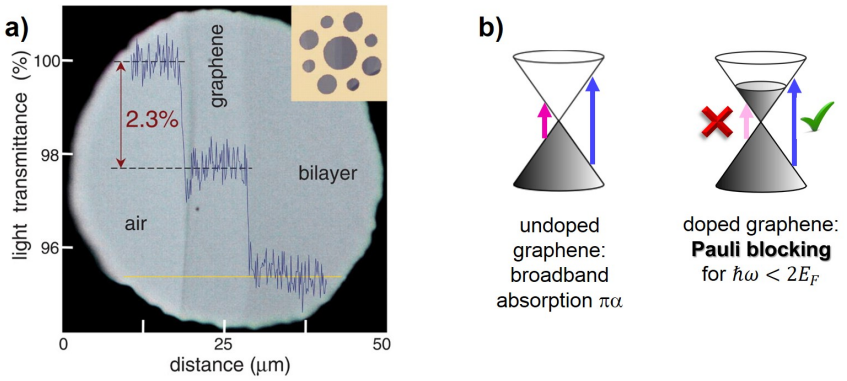

Figure 1.3: a) Microscope image of transmitted white light from suspended single layer and bilayer graphene from Nair *et al.* [2008], showing the percentage of absorbed light (in blue) along the yellow line at the bottom. The graphene flakes were placed on top of a metal structure with different apertures (shown in the inset on the right).. b) Sketch of graphene dispersion with different band filling showing the allowed interband transitions giving rise to broadband absorption for undoped graphene, and the Pauli blocking for doped graphene.

layer [Nair *et al.*, 2008; Kuzmenko *et al.*, 2008]. Indeed, two-dimensionality[5] is key factor for the observation of a "quantized" absorption. Recently, InAs thin membranes on CaF_2 have shown an absorption in steps of 1.6% [Fang *et al.*, 2013a], i.e. compatible with the $\pi\alpha$ value when the effect of the local field due to the substrate is taken into account.

[5]A two dimensional semiconductor can be defined as a material with thickness smaller than its exciton Bohr radius $\alpha_B = \alpha_H \frac{\varepsilon}{m^*/m_e}$ where α_H is the hydrogen Bohr radius, ε is the permittivity, m_e is the electron mass and m^* is the reduced mass.

Indeed, considering a single interface, i.e. if the thin layer is on an infinitely thick material, the correction to the absorption A_0 for a suspended membrane is

$$A = A_0 \left(\frac{2}{1+n_s} \right)^2 \tag{1.2}$$

where n_s is the refractive index of the substrate.

In Stauber *et al.* [2015], a recent theoretical work on the universal absorption of two-dimensional systems, it is demonstrated that the universality holds, except for pre-factors taking into account the spin and valley degeneracy g_s, g_v and the band curvature v:

$$A = g_s g_v \, v |1+r|^2 A_q \tag{1.3}$$

with r being the Fresnel reflection coefficient of an arbitrary multilayer system and $A_q = \pi\alpha/4$. This is shown both for Dirac and Schroedinger fermions in two dimensions, gapless or gapped but for energies close to the band gap, provided that excitonic effects are negligible and the band structures can be described starting from the single particle picture.

We note that the theoretical value for the universal absorption can be derived either by using the relation between the absorption of a 2D film and the optical conductivity, that is:

$$A_0 = \mathrm{Re}\sigma / \varepsilon_0 c \tag{1.4}$$

or by directly calculating the absorption from Fermi's golden rule.

Absorption of doped graphene

We now consider the more general case of graphene with a finite doping, where the absorption is due to both interband and intraband processes. The interband transitions are responsible for the 2.3% absorption for suspended graphene in the visible and NIR, and occur for $2E_0 = \hbar\omega > 2E_F$, while for $E_0 < 2E_F$ they are forbidden by Pauli blocking, as shown in the sketch in Fig. 1.3b [Mak *et al.*, 2008; Li *et al.*, 2008].

Intraband scattering leads to Drude absorption, which is stronger for shorter carrier scattering time τ and for larger E_F. This mechanism is responsible for the absorption in the far-infrared (THz frequencies) [Dawlaty *et al.*, 2008; Yan *et al.*, 2011] and also contributes to the mid-infrared (MIR) optical response [Mak *et al.*, 2008; Dawlaty *et al.*, 2008]. We note that absorption in the MIR region[6] has been attributed also to electron-electron interaction [Li *et al.*, 2008], whereas phonon-assisted absorption has been predicted for graphene on polar substrates [Scharf *et al.*, 2013].

Optical conductivity

Having presented the main experimental evidence concerning graphene absorption, now we proceed to take a closer look at the optical response of a graphene sheet, by analysing the optical conductivity. As we saw from Eq.1.4, the absorption is proportional to the real part of the conductivity; in Chapter 3 and later in Chapter 8 we will see how the conductivity has to be taken into account when considering the reflection and transmission coefficients for graphene on different substrates. Also, very importantly, a large positive imaginary part of the conductivity is related to the presence of plasmons, as it will become clear in Chapter 3.

Several theoretical works have derived the response to an external electric field and have studied screening and self-sustained charge density oscillations (plasmons, explained in detail in Chapter 3). For example, we mention Ando *et al.* [2002], Gusynin & Sharapov [2006], Wunsch *et al.* [2006], and Falkovsky & Varlamov [2007] where the first derivations can be found. In general, either the polarizability or the optical conductivity are obtained in the framework of the linear response theory, using the random phase approximation (RPA). The electrons are considered to move in a field that is the sum of the external field and the self-consistent field induced by all the electrons. In this way the many-body problem of electron-electron interactions is simplified by considering a

[6] The MIR region extends over the ~ 3—$30\ \mu$m wavelength range, which corresponds to ~0.4–0.05 eV and ~3000–300 cm^{-1}.

system of non-interacting quasi-particles[7].

For a complete treatment of the linear response we refer to many-body physics textbooks, for example Fetter & Walecka [2003]. However the main idea is that the linear response of a system to an external perturbation can be expressed in terms of the retarded correlation function of an operator. For example, in the case of the conductivity, the current-current correlation function is calculated. The current operator can be built from the Lagrangian of the system, which is where the band structure comes into play. The conductivity function used in this thesis is based on the Dirac cone approximation for the band structure. However, calculations beyond the Dirac cone have also been implemented in the literature. At optical frequencies Stauber *et al.* [2008] noted that the corrections to the band structure beyond the Dirac cone approximation result in only few percent difference in the conductivity, as confirmed by the absorption experiments that show good agreement with the ideal universal value.

In general the response depends on wavevector and frequency: $\sigma = \sigma(k, \omega)$. In addition, as the Fermi level is tunable, the conductivity is also a function of E_F. For the explanation of the experimental data presented in this thesis we consider the local limit, $k = 0$. Indeed the local $\sigma(k = 0, \omega, E_F)$ provides a description for the optical response and plasmons in good agreement with our experiments, and deviates from the non-local value only in limiting cases. For example, as we will see in Chapter 3, the full k dependence should be considered to study the details of the plasmon decay at the onset of the interband transition region in the (ω, k)-space. Instead the use of the local limit is jus-

[7]The name RPA has historical reasons. It comes from an approximation in the calculation of the equation of motion of the density operator, presented in a paper on the collective description of electron interactions by Bohm & Pines [1953]. However, it has been shown that the similar results can be obtained with diagrammatic techniques [Gell-Mann & Brueckner, 1957], now commonly used to treat many-body problems in different fields, from condensed matter to neutron stars. Therefore, the RPA approximation corresponds to considering the non-interacting diagram, referred to as the "bare bubble", while electron-electron interactions can be dealt with by adding complexity to the diagrams. For example in Abedinpour *et al.* [2011] the first order of electron-electron interactions, the so-called "vertex corrections", are taken into account for the calculation of graphene conductivity.

tified to treat plasmons in the region where they are well-defined excitations [Koppens *et al.*, 2011].

At zero temperature ($\vartheta = 0$) the optical conductivity has a simple analytical expression [Falkovsky, 2008]:

$$\sigma(\omega, E_F) = \underbrace{\frac{e^2 E_F}{\pi\hbar^2}\frac{i}{\omega + i\tau^{-1}}}_{intraband} + \underbrace{\frac{e^2}{4\hbar}\left[\Theta(\hbar\omega - 2E_F) + \frac{i}{\pi}\log\left|\frac{\hbar\omega - 2E_F}{\hbar\omega - 2E_F}\right|\right]}_{interband} \tag{1.5}$$

In the above equation we have highlighted the intraband and interband contribution terms. The Drude-like term arises from intraband processes, while the step function represents Pauli blocking in the interband transitions. For the sake of simplicity in this thesis we generally consider a fixed value for the scattering time τ present in the Drude term on the order of tenths of femtoseconds, compatible with our transport measurements[8]. In some cases when E_F is varied, as for example in Chapter 4, we take into account the variation of τ with E_F considering a fixed mobility μ, then $\tau = \mu E_F/(e\, v_F^2)$.

For the calculations and graphs of this thesis we need to take into account the effects of a finite temperature on the optical conductivity, for example the smoothing of the Pauli blocking step. This is done following the integral formula given in Falkovsky [2008], derived from the calculation of the current operator at finite temperature.

$$\begin{aligned}\sigma(\omega) = {} & \frac{2e^2\vartheta}{\pi\hbar}\frac{i}{\omega + i\tau^{-1}}\log[2\cosh(E_F/2k_B\vartheta)] \\ & + \frac{e^2}{4\hbar}\left[G(\omega/2) + \frac{4i\omega}{\pi}\int_0^\infty d\epsilon\,\frac{G(\epsilon) - G(\epsilon/2)}{\omega^2 - 4\epsilon^2}\right]\end{aligned} \tag{1.6}$$

where

$$G(\epsilon) = \frac{\sinh(\hbar\epsilon/k_B\vartheta)}{\cosh(E_F/k_B\vartheta) + \cosh(\hbar\epsilon/k_B\vartheta)} \tag{1.7}$$

[8] However, when considering plasmons, the scattering time at high frequency and the DC scattering time are not the same, as reported in more detail in Chapter 3.

In particular, for practical purposes we use the integration of Eq. 1.6 provided by the Etot software written by Prof. Garcia de Abajo[9].

Finally, in order to show the conductivity behaviour with respect to ω and E_F we select some experimentally relevant cases that are useful to understand the following chapters of this thesis.In Fig. 1.4 we present examples of graphene optical conductivity at room temperature and with a fixed τ of 50 fs, corresponding to a mobility of 5000 $cm^2V^{-1}s^{-1}$ at 0.1 eV.

In Fig. 1.4a we present the real and imaginary parts of the optical conductivity of graphene as a function of the photon energy E_{ph}, for three doping levels experimentally achievable with the techniques that are described in Chapter 2. As noted before, the graphene absorption is proportional to the real part of the optical conductivity: for $E_{ph} = 2E_F$ we clearly see the step due to the onset of the interband transitions, smeared out by thermal broadening; for low E_{ph} we see the Drude contribution, that becomes more relevant in the MIR range for an higher E_F. We note that the imaginary part of the conductivity is positive and larger than $e^2/(4\hbar)$ for $E_{ph} \lesssim E_F$.

In Fig. 1.4b on the other hand, we show the optical conductivity for fixed E_{ph} in the visible, NIR and MIR as a function of E_F. We see that up to E_F=1 eV real and imaginary part of the conductivity are basically constant for the case of E_{ph} in the visible regime. For E_{ph} in the NIR and MIR at $E_F = E_{ph}/2$ we can see the step due to Pauli blocking, while the imaginary part increases with increasing E_F.

[9]Analytical approximations at small ϑ are also presented in Falkovsky [2008]. In addition, an analytical expression for σ at finite temperature can be obtained introducing the thermal broadening phenomenologically as in Stauber *et al.* [2015]

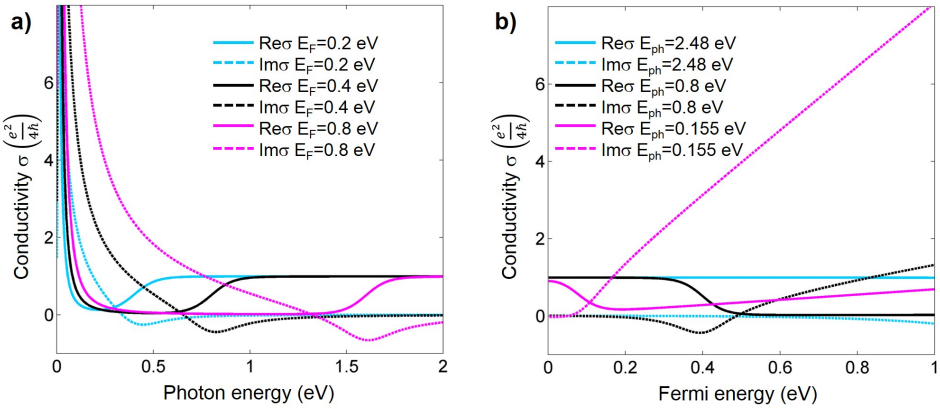

Figure 1.4: Graphene conductivity in the local limit ($k = 0$), using a fixed value of τ= 50 fs. a) Real and imaginary part of the conductivity as a function of photon energy for different values of E_F. b) Real and imaginary part of the conductivity as a function of E_F for incident photons in the visible, NIR and MIR.

2

Fabrication and characterization of the devices

This chapter explains the main fabrication and characterization tools common to all the devices used in the experiments presented in this thesis. We first describe the fabrication of the graphene transistors and the techniques used to control the graphene Fermi energy. Then we describe the electrical and Raman characterization techniques for graphene.

2.1 Fabrication of graphene transistors

The devices used in this thesis are in general based on the graphene transistor device, as the one demonstrated by Novoselov *et al.* [2004], with different shape and size according to the specific requirements of the experiments. Here we describe the typical fabrication procedure, specifying the solutions adopted for samples with different purposes. The detailed recipes for the main processes can be found in the Appendix A.

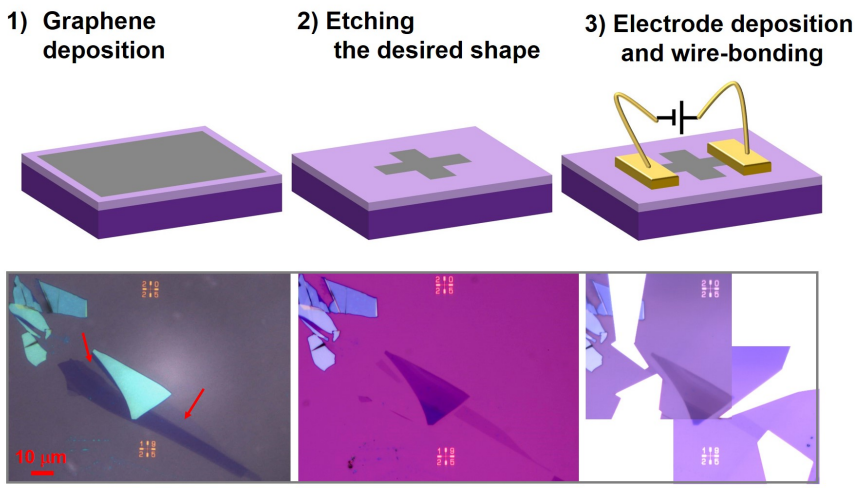

Figure 2.1: Top: sketch of the main steps of the fabrication of a graphene device for electronic measurements. Color code: dark/light violet: substrate, grey: graphene, yellow: metal electrode. Bottom: optical microscope images of a real device; left, flake with areas with different number of layers deposited by mechanical exfoliation on a SiO_2/Si substrate with markers (the arrows indicate the single layer areas, the dark violet area is few layer graphene, and the light blue areas are thicker graphite films); centre, single layer graphene areas are isolated by etching away areas with thicker layers (note that the thicker triangle in the middle is exposed to the etching, and therefore becomes thinner, e.g. dark violet); right, the isolated flakes are contacted with gold electrodes.

In Fig. 2.1 we explain the main steps towards the realization of our graphene devices. The fabrication starts with the graphene deposition on the substrate, often previously equipped with markers. Following the deposition, there is an optional step where the graphene is shaped according to the need (for example, micrometer-sized Hall bars for the experiments on the electrical control of Er^{3+} emission presented in Chapter 4, tapered nanoribbons for the near-field imaging of graphene plasmons presented in Chapter 5, or rectangles and crosses of several tenths of micrometers for the devices used in mid-infrared photocurrent experiments presented in Chapters 8 and 9). Then, the metal electrodes are deposited, and after a chemical cleaning or annealing treatment to reduce the residues from the fabrication process (see the Appendix for more details), the device is wire-bonded to the chip carrier in order to be connected with the electronics of the setup.

Graphene deposition

Large area (several μm^2) graphene for electronics[1] can be produced in three main ways: mechanical cleavage of graphite crystals [Novoselov *et al.*, 2004, 2005b], chemical vapour deposition (CVD) [Kim *et al.*, 2009; Li *et al.*, 2009], and epitaxial growth on silicon carbide (SiC) Si-terminated or C-terminated face [Berger *et al.*, 2004; Hass *et al.*, 2006].

The samples used in the experiments presented in this thesis are obtained mainly by depositing the graphene via mechanical exfoliation or by transferring CVD graphene grown by external sources onto the desired substrate. We worked with different substrates (such as SiC, lithium niobate ($LiNbO_3$) or erbium-doped yttria (Er^{3+}:Y_2 O_3), but the most used substrate for our graphene FETs is a thermally grown film of hundreds of nanometres of silica (SiO_2) on top of a 0.5 mm thick doped silicon wafer, a widely used substrate in microelectronics. A SiO_2 layer thickness of 285 nm or 90 nm allows the optimal contrast (up to $\sim 10\%$) for green light due to constructive interference of the reflection from the SiO_2-Si and SiO_2-air interfaces [Blake *et al.*, 2007; Roddaro

[1] Suitable to be contacted and gated.

et al., 2007; Ni *et al.*, 2007].

Mechanical cleavage of highly ordered pyrolytic graphite (HOPG) has been the first method used to fabricate graphene field effect transistors (FETs) [Novoselov *et al.*, 2004], and it is still widely used in the scientific community often in combination with a transfer step to place the flakes on a specific position or substrate. The graphite crystal is exfoliated by folding and unfolding a tape until the tape is uniformly covered with tenths of nanometre-thick microcrystals, becoming dull grey. As the tape is pressed onto a substrate, single and multilayer flakes are deposited. A critical step in this procedure, which can affect the yield and the size of resulting flakes, is the removal of the tape from the substrate. This has to be done very slowly and carefully, or using a tape that can be thermally released or removed by immersion in a solvent[2].

Mechanical exfoliation, despite having a low yield, is the preferred method when micrometer-size high quality flakes of graphene, bilayer or multilayer graphene are required. This technique can be successfully applied also to obtain thin layers of crystals of other materials where the in-plane bonds are strong while the inter-planar interactions are mediated by the Van der Waals force, for example hexagonal boron nitride (hBN) or transition metal dichalcogenides [Novoselov *et al.*, 2005b].

Chemical vapour deposition (CVD) of graphene (typically using a metal as nickel or copper as a catalyst [Kim *et al.*, 2009; Li *et al.*, 2009]) enables the possibility of having cm^2 large areas of single layer graphene, and has potential for industrial applications, as roll-to-roll production has already been demonstrated [Bae *et al.*, 2010]. For the fabrication of our devices we relied on CVD graphene on copper acquired from external sources[3] and transferred onto the substrate after etching away the copper with the procedure shown in Fig. 2.2.

In addition, to conclude this section on graphene deposition, we want to point out that it is possible to place exfoliated graphene flakes in a specific position with micrometer precision with different transfer methods, either wet, i.e. where the graphene gets in contact with water, or dry, as shown in Fig. 2.3.

[2] For example the methyl isobutyl ketone, MIBK.
[3] In particular the Spanish company Graphenea.

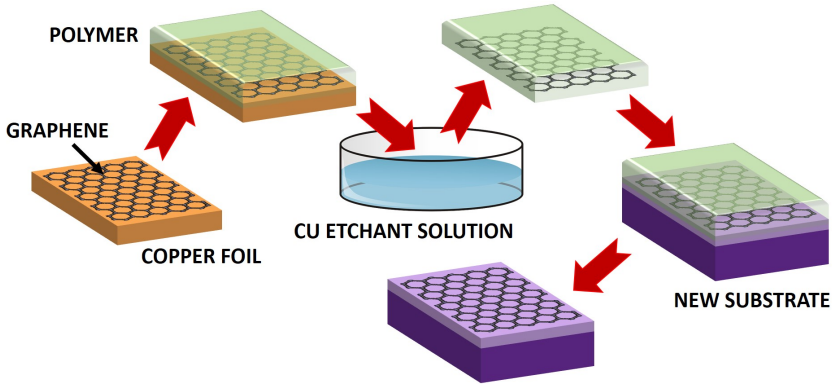

Figure 2.2: Scheme of the transfer process of CVD graphene grown on copper as in ref. Li *et al.* [2009]: a polymer (typically PMMA) is spin coated on top of the copper foil with graphene; the structure is then immersed in an etchant solution (iron chloride or ammonium persulfate) until the copper is completely removed and only the polymer with the graphene is left floating in the solution. The polymer is then deposited on the final substrate and dissolved with acetone, leaving the clean graphene on the substrate.

In Fig. 2.3a,e we show the basic concept and an example of wet transfer, or wedging. Graphene (or nanostructures of a different material) placed on top of a hydrophilic substrate is coated with an hydrophobic polymer, and then detached from the substrate exploiting water infiltration between the hydrophilic surface and the hydrophobic polymer [Schneider *et al.*, 2010]. In this way the polymer containing the flake is left floating in the water and can be carefully placed in a specific position with the help of a micro-manipulator. Working with the polymer floating in water is a disadvantage of this method, both for the final quality of the device[4] and for the difficulty of the positioning.

[4]Water molecules can induce (inhomogeneous) doping of the graphene, and the evaporation of water trapped between the graphene and the substrate can lead to bubble formation or tear the graphene apart.

However, it allows big flexibility on the choice of the flake since it is possible to first deposit flakes on the substrate where the contrast is optimum, and then select the best for the transfer.

Dry transfer methods that avoid graphene contact with water are also currently widely used. In particular, one option is to deposit the mechanically exfoliated flakes directly on top of PMMA (or MMA) layer on a transparent substrate [Dean *et al.*, 2010]. After finding the desired flake with an optical microscope, one can position it with a micro-manipulator, and then raise the temperature to make the polymer melt and detach from the transparent substrate, leaving the graphene on the desired spot on the new substrate, as shown in Figures 2.3c,e.

A resist-free procedure has been recently developed, particularly advantageous in the case of fabrication of stacks of different 2D materials. The process, shown in Fig. 2.3d, involves picking up flakes of graphene previously deposited on a substrate relying on the adhesion to a hBN flake on top of PDMS [Wang *et al.*, 2013].

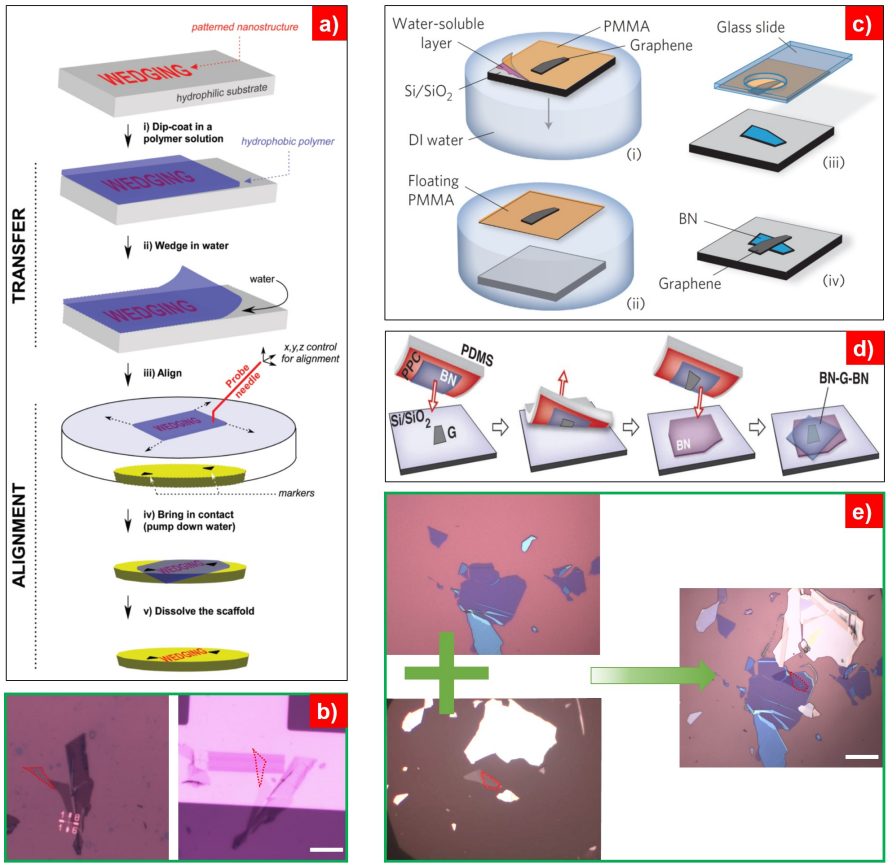

Figure 2.3: a) Wedging transfer procedure for graphene and nanostructures from Schneider *et al.* [2010]. b) Microscope pictures of an example of the wedging procedure: a graphene flake (indicated by the red dashed triangle) is positioned on top of a gold pad with nanostructures. The scale bar is 10 μm. c) Graphene dry (graphene not in contact with water) transfer procedure with PMMA from Dean *et al.* [2010]. d) Graphene pick-up procedure from Wang *et al.* [2013]. e) Microscope reflection images of an example of dry transfer following the procedure in Dean *et al.* [2010] but with graphene exfoliation on a different substrate. Top left, hBN flakes exfoliated on a SiO_2/Si substrate. Bottom left, graphene exfoliated on top of MMA (indicated by the red triangle), with a stack of a glass slide, a layer of PDMS and tape as support substrate. Right, result of the transfer of the graphene flake (red triangle) on hBN. The scale bar is 10 μm.

Etching the desired shape

When the graphene has been deposited on the final substrate, it is possible to give it any form needed for the specific measurement by etching away the unwanted part. This is done by patterning a resist previously spin-coated on top of the sample with a lithographic technique, as explained in Fig. 2.4. The exposure to either an electron beam or UV light modifies a selected area of the resist, which therefore becomes soluble in a developer. After development, a treatment with a mild oxygen plasma is performed in a Reactive Ion Etching (RIE) system (Oxford Instruments), enabling the removal of the graphene in the areas that have been developed.

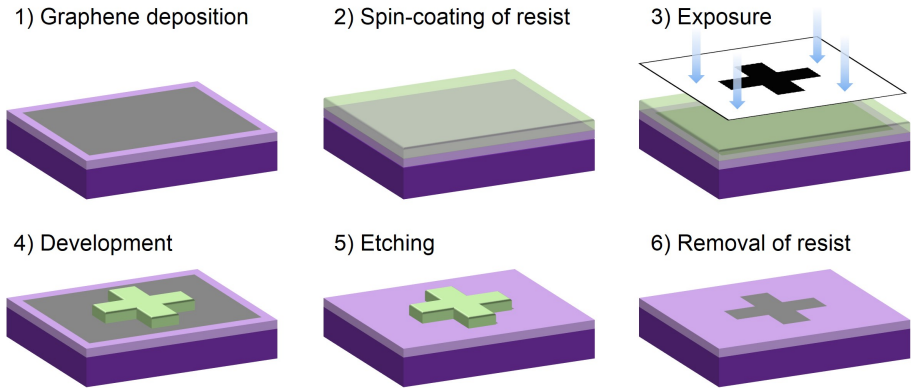

Figure 2.4: Sketch of the steps for etching the desired shape out of a graphene sheet. Color code: dark/ligh violet: substrate, grey: graphene, light green: resist.

In order to pattern the graphene, we used three lithographic processes according to the needs in terms of feature resolution, writing time and design flexibility:

Electron beam lithography (EBL) performed with Elphy plus and Quantum Raith systems. The de Broglie length of an electron accelerated with a 30 kV tension is ~ 7 pm, however EBL resolution is limited by charging ef-

fects, secondary electron generation and forward scattering in the resist, as well as aberrations[5] and therefore reaches a few nanometres. This is the technique chosen to obtain nanostructures, for example nanoribbons with widths down to few tenths of nanometres (see Fig. 2.5). Since it allows to directly write any pattern, it is flexible to be used to expose the areas to contact or etch graphene exfoliated flakes. In addition the resist used, PMMA, allows for a water-free process, is generally thinner and leaves less residues than the resist used for optical lithography. The main disadvantage of this technique is the very long writing time. For example, to write an area A of 1 mm^2 using a typical dose D of 300 $\mu C/cm^2$ and beam current[6] I of 1 nA it would take t=D*A/I=3*10^3 s, i.e. 50 minutes, without even considering the extra time needed to move the stage and to deflect or blank the beam. When using this technique extra-care should be taken when exposing a non-conducting substrate to avoid the charging effects, in the Appendix we report the procedure both for the standard doped Si substrate and for $LiNbO_3$, a non-conducting piezo and pyro-electric substrate.

UV-mask lithography performed with a Quintel Q4000 mask aligner. This optical lithography technique allows to pattern large areas (typically 1x1 inch, but up to a 4x4 inch wafer) at once in just few seconds using a physical mask, with a minimum feature size of a few micrometers. Edge roughness can be introduced if the alignment between the mask and the sample surface is not optimal. However, ocasionally we have used it before a further step of EBL on CVD graphene in order to isolate the areas which are identified for subsequent patterning of nanostructures. The main drawback of this UV lithography for our purposes is that it relies on a mask, made after a custom design, that is acquired from an external source. This makes it not flexible enough to deal with frequent design changes needed in the process of sample optimization.

[5] Magnetic lenses are used to focus.

[6] We generally used currents between 3.5 and 0.045 nA, achieving higher resolution with lower current, which corresponds to a smaller aperture for the electron beam.

Laser writing performed with a Microtech LW405B system. This optical lithography technique patterns the resist by scanning the UV beam over the sample and, as in the case of EBL, allows to directly write the desired design. It reaches feature size down to $\sim$ 1-2 μm, and it is advantageous when a combination of flexibility and acceptable writing times are sought. For example, a 1 mm^2 area can be written in $\sim$ 30 s with the typical settings for the best resolution[7].

More details on the specific recipes and the different resists used can be found in the Appendix A, while in Fig. 2.5 we show examples of samples fabricated using these three different lithographies.

[7] Lens 5, Dstep 2.

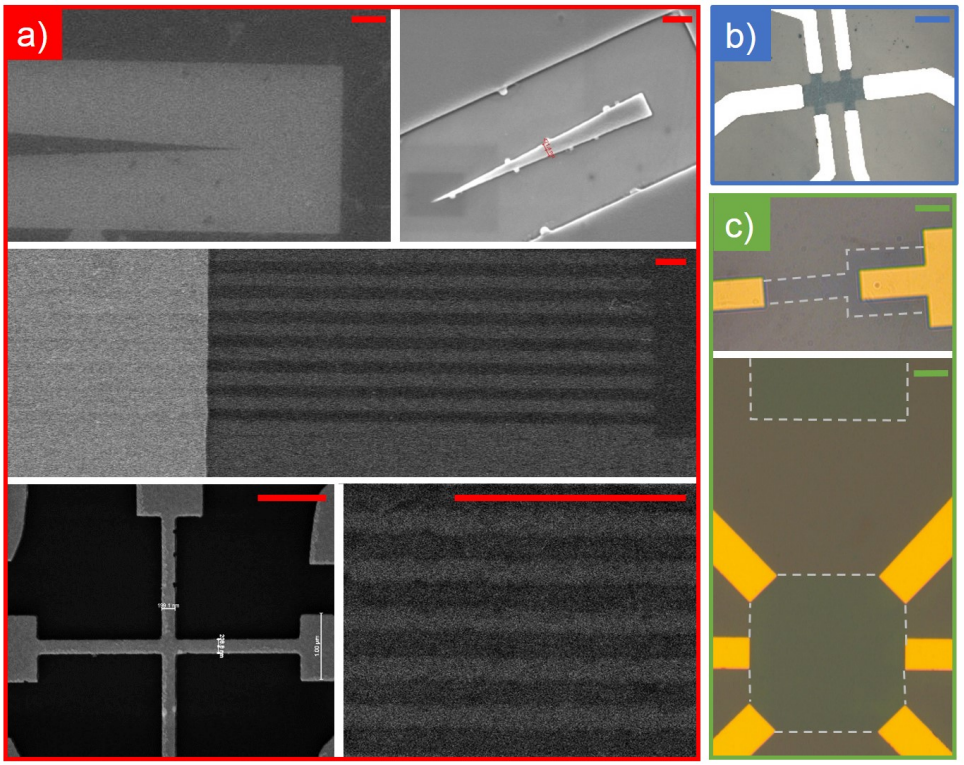

Figure 2.5: a, red frame) Scanning electron microscope (SEM) images of devices obtained by patterning with EBL, the scale bars represent 1 μm. Top left: tip of a graphene triangle on SiO_2/Si, (dark areas: graphene, lighter areas: substrate). Top right: triangle of PMMA on SiC, imaged for a dose test after a thin gold film (<5 nm) evaporation. Centre: contacted graphene ribbons, (dark grey areas: graphene, grey areas: substrate, light grey areas: gold). Bottom left: gold marker (light grey) on SiO_2/Si (black). Bottom right: graphene ribbons. b, blue frame) Optical microscope image of a Hall bar obtained by patterning with the UV mask aligner, the scale bar is 10 μm. c, green frame) Optical microscope images of devices obtained by patterning with the laser writer, the scale bar is 50 μm. The grey dashed lines indicate the graphene areas. Note the flexibility of the design: for example, the bottom image shows how the graphene area to be contacted can be chosen after the etching.

Electrode deposition and wire-bonding

Once the graphene is deposited and has been etched into its final shape, a lift-off procedure is used to fabricate the electrodes. This procedure starts with a new step of lithography for defining the pattern of the electrodes. The development leaves the resist (sacrificial layer) everywhere except in the areas where the electrodes have to be. After development, metal is deposited with the evaporator Univex 350 (Leybold - Oerlikon), and the resist outside the electrode areas is subsequently removed (see the Appendix for more details). The electrodes in our samples typically consist of 3 nm of titanium as adhesion layer, deposited with electron beam evaporation, and 100 nm of gold, deposited with thermal evaporation.

Also for the definition of the pattern of the electrodes it is possible to use the three options for lithography mentioned above, using a procedure to align the pattern to be written with the markers previously defined on the sample. The pattern overlay with EBL can easily reach an accuracy better than 50 nm, while the optical lithography techniques provide micrometer precision in the alignment.

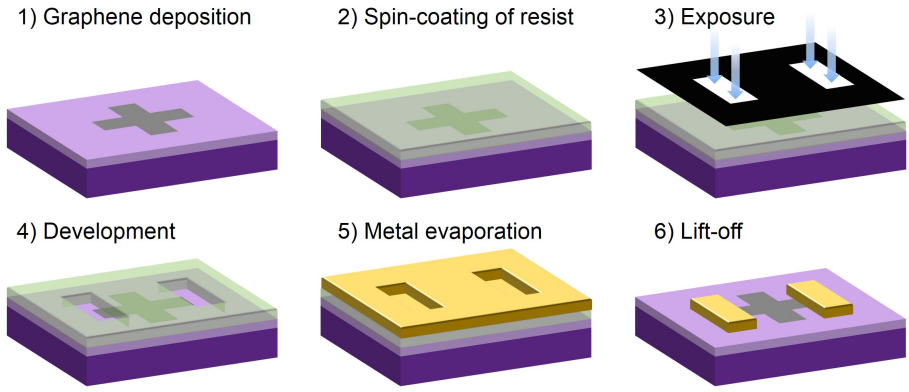

Figure 2.6: Sketch of the steps for the electrode fabrication. Color code: dark/ligh violet: substrate, grey: graphene, yellow: metal electrode.

The electrodes are then connected to the chip carriers used in the optoelectronic setups via wire-bonding (see Fig. 2.7). For the devices used for this thesis, ball and wedge-bonding with gold wire with a Leica S6 and wedge-bonding with aluminium wire with a West bond Luxury II have been exploited, with the latter wire-bonder giving far better throughput (close to 100 %). The issues that might rise in the wire-bonding process are the risk of damaging the electrodes and the risk of damaging the underlying oxide layer, inducing a leakage.

If the electrodes have adhesion problems[8] bonding can prove quite critical. An alternative that we employed in such cases is using silver-paste for the bond on the sample: a droplet of silver paste is deposited on the electrode with the bonding wire, whose other end is then bonded to the chip-carrier after the silver paste has dried.

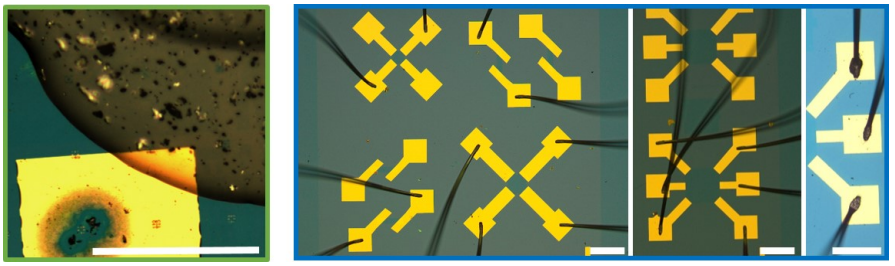

Figure 2.7: Left, green frame: damaged electrode contacted with silver paste. Right, blue frame: examples of wire-bonded devices. The scale bars represent 200 μm.

2.2 Controlling the graphene Fermi energy

There are several ways of controlling the graphene Fermi energy (i.e. the graphene doping), either with techniques that allow in-situ tunability or with

[8]For example if there is some resist left underneath the electrode, which is often the case if large areas of graphene are not etched away underneath the metal pad.

methods which result in a fixed charge carriers concentration[9]. For most of the experiments presented in this thesis we employ tunable techniques, where the tunability is achieved by controlling the voltage applied to a gate. In particular, the most used techniques are back-gating and electrochemical gating, whose principles of operation are shown in Fig. 2.8.

The easiest way to electrostatically tune the graphene doping is by means of a doped silicon back-gate with a thermally grown SiO_2 film on top, as widely used in semiconductor electronics. In a simple capacitor picture, when a potential difference is applied between graphene and a gate, charges of opposite sign accumulate at the two ends of the capacitor. Clearly the same concept can be applied using a different gate dielectric, for example choosing a material with a higher permittivity, and a different material or geometry for the gate, for example using a metal or even graphite as a back or top-gate.

The graphene Fermi level that is reachable employing these configurations is limited by the breakdown voltage of the gate dielectric. As a rule of thumb, in the standard SiO_2/Si case one can safely apply up to 30-40 V per 100 nm. The relation between the induced carrier density and the applied voltage is simply

$$n_{BG} = \frac{C_{\text{ox}}}{e}|V_{BG} - V_D| \tag{2.1}$$

where C_{ox} is the oxide capacitance, and V_D is the charge neutrality point, or Dirac point. Replacing eqn.2.1 into eqn. 1.1, we have

$$E_F = \hbar v_F \sqrt{\pi \frac{C_{\text{ox}}}{e}|V_{BG} - V_D|}$$

therefore, with a 300 nm thick SiO_2 layer, if $V_D = 0$ V it is possible to modify the Fermi level up to ± 0.3 eV applying ± 100 V.

[9] So-called chemical doping, already shown in the Supplementary information of Novoselov *et al.* [2005b], where molecules adsorbed on graphene modify the charge carrier density. Also intercalation, a technique widely used to modify the properties of graphite [Dresselhaus & Dresselhaus, 2002], has been successfully applied to obtain strongly doped few layer graphene [Khrapach *et al.*, 2012].

In order to reach higher levels of doping, even up to $\sim 1eV$, we rely on electrochemical doping. An electrolyte is put in contact on one side with graphene and on another side with a gate. When a voltage is applied to the gate, the ions in the solution will move in towards the electrode with the opposite polarity. The equilibrium distribution is determined by the Coulomb force as well as the solution concentration gradient. This results in the accumulation of the ions in thin Debye layers of opposite polarity close to the gate and above the graphene surface, inducing charges of the opposite sign in graphene, as shown in Fig. 2.8.

We employed a polymer electrolyte, more stable and easier to handle than an aqueous solution, following the successful implementation of this method used in polymer electronics [Sirringhaus *et al.*, 2000; Dhoot *et al.*, 2006] to carbon nanotubes [Lu *et al.*, 2004] and graphene [Das *et al.*, 2008]. A methanol-based mixture of PEO- $LiClO_4$ is drop-casted on top of the device, and the potential difference is applied between the graphene and a metal gate close to the graphene (more details in the Appendix).

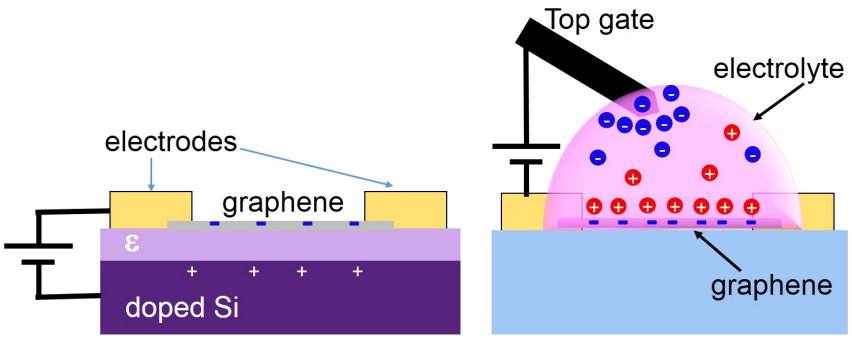

Figure 2.8: Left: back-gating. Right: electrolyte gating

2.3 Electrical characterization

After the fabrication we proceed to an electrical characterization of the devices in order to determine the intrinsic doping and evaluate the mobility. We measure the source-drain current applying a small bias voltage (typically 1 mV) while sweeping the gate to change the carrier density. The charge neutrality point, or Dirac point V_D, is the gate voltage where the conductance shows the minimum. For graphene on SiO_2, V_D in air is generally away from 0 V, and lies in the positive (or negative) voltage range, indicating an intrinsic hole (or electron) doping.

In the inset of Fig. 2.9a we show a typical measured conductance as a function of back-gate voltage V_{BG}. When the system capacitance is known, it is simple to get an estimate of the mobility even from a two probe measurement as the one presented here. The measured conductance is described by

$$G = \frac{1}{R_c + \frac{A}{e\mu n}} \tag{2.2}$$

where R_c is the contact resistance, μ is the mobility, n the charge carrier density, and A is the aspect ratio (length/width) of the device. We assume the mobility to be independent of the carrier density.

We can plot the intrinsic conductance subtracting from Eq. 2.2 a value for R_c, which in our samples in the order of ~ 1 kΩ. We will have a correct value for R_c when the graph shows a linear relation between back-gate voltage and conductance (except close to the CNP), as shown in Fig. 2.9a. Away from V_D the carrier density follows eqn.2.1, therefore it is straightforward to obtain an estimation of the mobility by looking at the slope of the intrinsic conductance: $\mu = \frac{dG}{dV_{BG}} * A/C_{ox}$.

Alternatively, one can directly fit the conductance and get an estimate for both the mobility, the contact resistance and the residual charge density at the Dirac point n_0 by inserting in eqn.2.2 the empirical formula [Meric *et al.*,

2008]:

$$n_{emp} = \sqrt{n_0^2 + (\frac{C_{ox}}{e} V_{BG})^2} \tag{2.3}$$

A result of this kind of fit is presented in Fig. 2.9b, showing good agreement with the measured data.

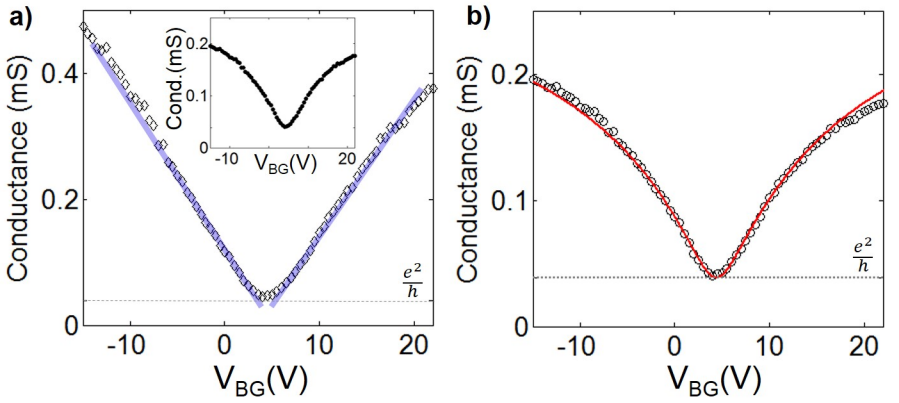

Figure 2.9: a) Intrinsic conductance plot, $1/G - R_c$, of a single layer graphene device with aspect ratio 6.5 on a SiO_2(90 nm) /Si substrate. R_c=3kΩ is estimated from the resistance plot. The blue lines are guides to the eye to show the linearity. In the inset the raw data are plotted. b) Black circles: measured conductance of the device in a). Red line, fit to the conductance using Eq. 2.2 and Eq. 2.3. The values obtained from the fit are μ= 4250 $cm^2V^{-1}s^{-1}$, R_c= 3.1 kΩ and n_0=4.2×10^{11} cm^{-2}. In both panel the dotted horizontal line indicates the value of e^2/h.

2.4 Raman spectroscopy

Raman spectroscopy is a powerful tool to assess many characteristics of graphene devices, such as the layer thickness, the intrinsic doping and presence

of defects, and it is a non-invasive measurement that can be performed before or after the fabrication process [Ferrari *et al.*, 2006; Ferrari, 2007; Ferrari & Basko, 2013].

Raman spectroscopy relies on inelastic (Raman) scattering of light. When VIS or NIR radiation impinges on a material, a small fraction[10] of the scattered light is frequency-shifted by a quantity that depends on the vibronic states of the system. If the incident light is not resonant with the electronic transitions of the system, the vibrational frequencies are probed (phonons in the case of solids).

In graphene, incident light in the VIS and NIR always leads to an electronic transition, therefore Raman spectroscopy is not only a probe of vibrational states but also of electronic properties and electron-phonon interactions. The three main peaks that provide us with useful information on the samples are the G peak, at ~ 1580 cm^{-1}, the D peak at ~ 1350 cm^{-1}, and the 2D at ~ 2700 cm^{-1}.

The G peak originates from a stretching mode of carbon atom pairs. This mode corresponds to the optical phonon at $\mathbf{q}$=0 (Γ point). As shown in Fig. 2.10 (adapted from Das *et al.* [2008] and Yan *et al.* [2007], the width and the position of the G peak are strongly affected by the Fermi level. Indeed, the width is given by the intrinsic width plus a contribution related to the decay into e-h pairs. When the Fermi level is increased up to half of the energy of the phonon, Pauli blocking occurs and therefore the phonon width is reduced, as shown in Fig. 2.10. The energy of the transition, i.e. the position of the G peak, also depends on the electronic levels and changes with doping, shifting to higher frequencies for stronger doping. Furthermore, the G peak can probe strain, as illustrated in figure 2.11 from Frank *et al.* [2011]. Uniaxial strain breaks the symmetry of the system, leading to a broadening and shifting towards smaller energies for little strain up to a clear splitting of the G peak into G^+ and G^- peaks for stronger strain [Mohiuddin *et al.*, 2009; Huang *et al.*, 2009].

The D peak originates from the breathing mode of the carbon ring and

[10] Several orders of magnitude, $\sim 10^6$, smaller than the incident light intensity.

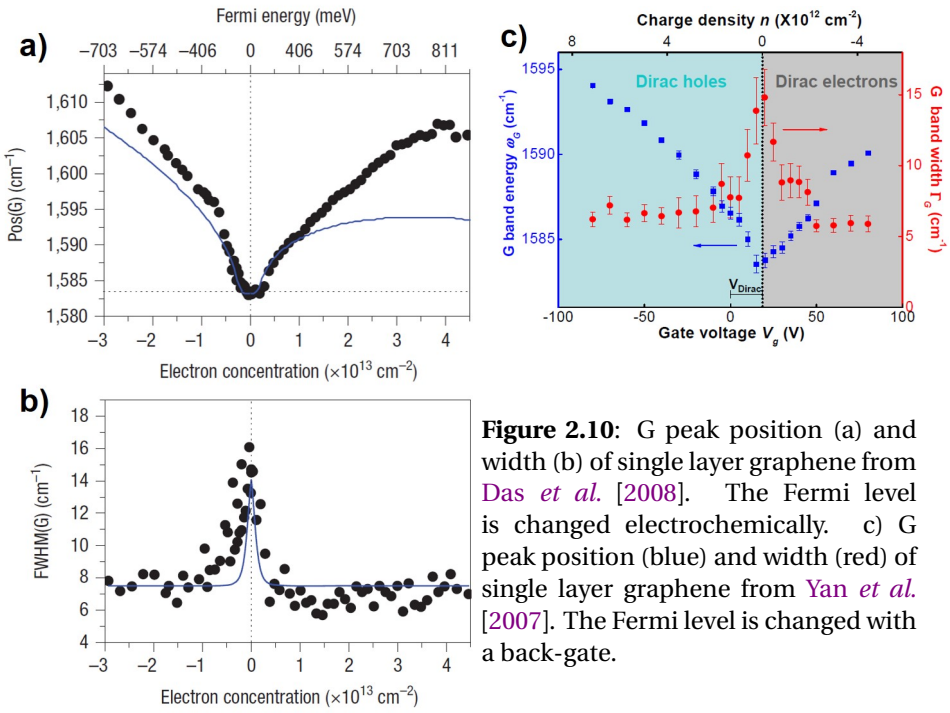

Figure 2.10: G peak position (a) and width (b) of single layer graphene from Das *et al.* [2008]. The Fermi level is changed electrochemically. c) G peak position (blue) and width (red) of single layer graphene from Yan *et al.* [2007]. The Fermi level is changed with a back-gate.

it is activated by the presence of defects.[11] The ratio I(D)/I(G) shows a non monotonic behaviour in carbon materials, and it reaches the maximum at the threshold between crystalline graphite and amorphous carbon [Ferrari & Robertson, 2000]. Monitoring the D peak and the less intense D' peak at ~1620 cm^{-1} can give information not only on the quantity but also on the nature of the defects [Eckmann *et al.*, 2012].

Finally, the 2D peak is the second order of the D peak, but being a two-

[11]The D peak arises from a double resonance process a the K point, where an e-h pair is created, a momentum q=K is exchanged in an electron-phonon scattering event (inter-valley scattering), then defect scattering occurs with the emission of the phonon at frequency ω_D, followed by e-h recombination. When a similar process occurs, but within the same valley (small exchanged q) the D' peak arises [Thomsen & Reich, 2000; Ferrari, 2007].

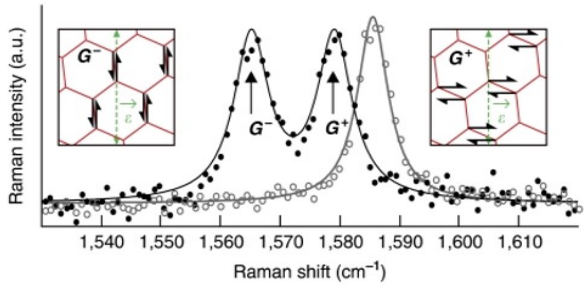

Figure 2.11: Graphene spectra from Frank *et al.* [2011], in white without any strain, in black with 1% uniaxial strain. In the insets the two modes whose degeneracy is lifted by the strain are shown.

photon process it does not require the presence of a defect for its activation[12], and therefore it is always present.

Importantly, single layer graphene shows a 2D peak whose line-shape is a single Lorentzian with fwhm ∼30 cm^{-1}, and a higher intensity of the 2D peak with respect to the G peak. These very distinct features allow fast identification of a single layer among flakes of different thickness. In bilayer graphene the 2D is broader and has a characteristic shape as it consist of 4 peaks [Ferrari *et al.*, 2006].

A detailed analysis and fit of the 2D peak can give information on the layer thickness for few layer graphene and also on the stacking orientation for few layer graphene [Lui *et al.*, 2011]. Changing the doping affects the 2D peak in a less dramatic way than the G, however it has been shown that its position shifts to smaller frequencies for hole doping and to higher frequencies for electron doping [Yan *et al.*, 2007; Das *et al.*, 2008]. Strain also affects significantly the 2D peak position, with a red-shift as large as 30 cm^{-1} for a 1% applied strain

[12]Indeed, considering the same double resonance process that gives rise to the D peak, the momentum is conserved if the momentum of the two emitted photons is opposite. Like in the case of the D peak, the exact position depends on the frequency of the incoming light that determines the e-h pair creation.

[Ni *et al.*, 2008; Mohiuddin *et al.*, 2009; Huang *et al.*, 2009].

It is worth noting that the layer thickness can be also determined from the position of a recently observed C peak, originating from the shear mode between layers [Tan *et al.*, 2012]. However this mode is at 30 cm^{-1}, therefore at a frequency generally not reachable with a typical commercial Raman spectrometer.

To perform the Raman measurements on our samples we used a commercial Renishaw system, with 532 nm of excitation wavelength and a 1800 mm/groove diffraction grating. The power was set always below 2 mW not to damage the sample [13]. As an example, in Fig. 2.12 and 2.13 we show the most remarkable cases where Raman spectroscopy helps to asses the kind and quality of our samples.

In the case of CVD graphene from two different samples, in Fig. 2.12a we compare the spectra in the 1280-1700 cm^{-1} range to monitor the amount of defects: the absence of the D peak in the light-blue spectrum indicates a defect-free graphene sheet. In Fig. 2.12b we show the clear difference of the 2D peak in single layer and bilayer graphene.

It is possible to perform scanning Raman maps of the samples, in order to analyse a specific characteristic over a wide region: for example, the presence of charged impurities can be detected [Casiraghi *et al.*, 2007]. In Fig. 2.13 we present a study of the local doping variation in a large area of CVD graphene, obtained by measuring a spectrum in the range 1300-1800 cm^{-1} every 0.5 μm over the entire sample. The G peak position and width maps are obtained by fitting the data with a single Lorentzian[14], after having confirmed the absence of the D peak.

As expected from the origin of the G peak previously explained, we clearly see a correlation between the width and the position of the peak. We observe a quite uniform background and single isolated spots with a remarkably

[13] On the standard SiO_2/Si where the graphene has optimum visibility the interference also increases the Raman signal, therefore a spectrum with a good signal to noise can be acquired in just few seconds. On different substrates longer time or many accumulations are needed.

[14] For the fits we used the map analysis tool of the Renishaw Wire 3.3 software.

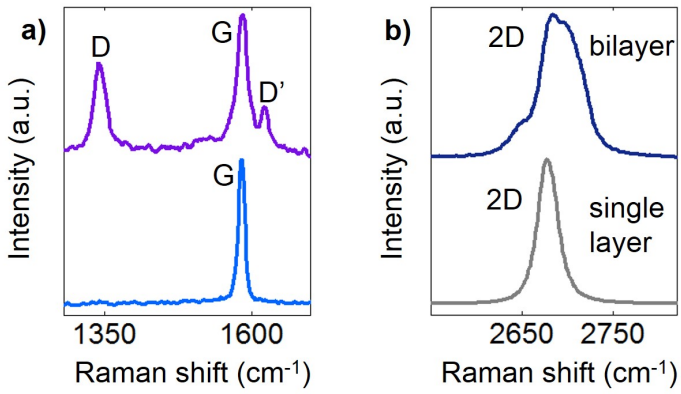

Figure 2.12: a) Spectra of different samples of CVD graphene in the range 1280-1700 cm^{-1}, offset for clarity. The spectrum at the bottom exhibits only the G peak, while the defect-activated D and D' peaks are clearly visible in the top spectrum. b) Spectra of exfoliated graphene flakes in the range 2550-2820 cm^{-1}, offset for clarity. Bottom: 2D peak of single layer graphene. Top: 2D peak of bilayer graphene.

lower frequency. This behaviour is reflected also in the distribution: the position distribution clearly shows a double peak, where the main peak has only $\sim$1.5 cm^{-1} fwhm, while in the width distribution we observe a broader peak with a tail towards larger widths[15]. Comparing the measured G position with the values reported in Fig. 2.10, we observe that the position of the main peak of the distribution at $\sim$ 1587 cm^{-1} is compatible with the intrinsic doping determined from electrical measurements, where we found V_D=-60V.

[15]The fact that we cannot resolve a double peak in the width distribution is probably due to the fact that we neglected the gaussian contribution to the peak by performing a simple Lorentzian fit.

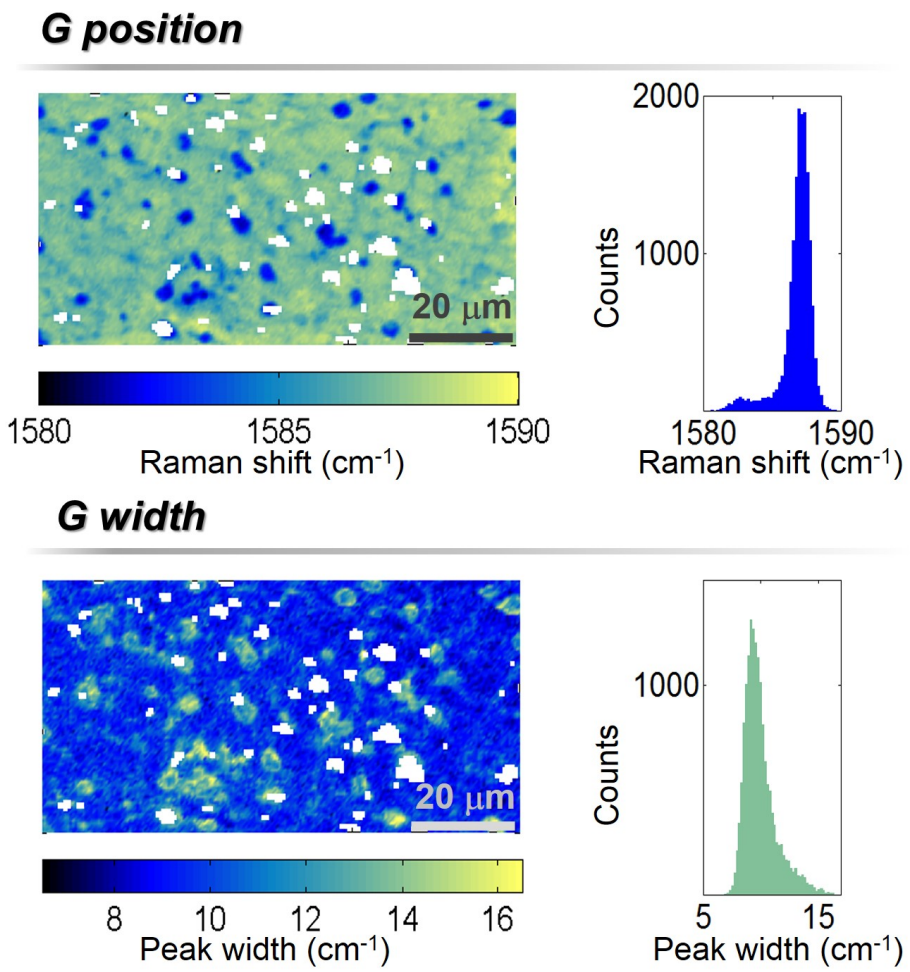

Figure 2.13: Left: Raman maps of position and width of the G peak for a large area of CVD graphene, obtained by fitting point by point using the specific tool in the Renishaw software Wire. The white areas denote the points where the fitting procedure did not work. Right: distribution of the G peak position (top) and width (bottom).

Part I

Graphene nanophotonics and plasmonics

3

Manipulating light at the nanoscale with graphene

In this chapter we discuss two fundamental topics in nanophotonics: plasmons and the coupling between an optical emitter and its environment. In particular, we concentrate on graphene nanophotonics. We present the basics of graphene plasmonics, and we address the in-situ tunable near field coupling between optical emitters and graphene.

Tailoring the properties of nanostructured materials or thin films enables the manipulation of light at the nanoscale, which is highly desirable in several applications of nanophotonics. Particularly important in this regard is the control over surface plasmons[1], electromagnetic waves confined at a metal-dielectric interface, that can also be viewed as collective oscillations of charge density at the surface of a conductor. These modes allow subwavength optics and strong enhancement of the electric field, useful for biosensing and photovoltaics. Furthermore, as we will discuss later, the presence of such modes can be used to change the spontaneous emission rate of a dipole by acting on the optical density of states.

3.1 Surface plasmons

For a complete treatment of surface plasmons and localized surface plasmon resonances[2], we refer to one of the many reviews, for example Barnes *et al.* [2003], Maier & Atwater [2005] or Giannini *et al.* [2010]. Here, we emphasise some important aspects necessary for the introduction of graphene plasmons, following Jablan *et al.* [2013].

The surface plasmon dispersion is obtained from Maxwell's equations, matching the boundary conditions at the interface between two materials with dielectric constant ε_1 and ε_2. Self-sustained oscillations are possible when the dielectric constants have opposite signs: surface plasmons are the case of a metal-dielectric interface, but analogous oscillations involve polar materials, in that case called surface phonons[3]. Indeed the boundary conditions lead to $\varepsilon_1 k_{\perp 2} + \varepsilon_2 k_{\perp 1} = 0$, where $k_{\perp 1,2} = \sqrt{\varepsilon_{1,2} k_0^2 - k_\parallel^2}$ is the wavevector in the plane perpendicular to the surface, $k_\parallel$ is the in-plane wavevector and $k_0 = \omega/c$ is

[1] Or, more correctly, surface plasmon polaritons.

[2] They occur when the surface plasmons are confined in a nanostructure whose size is comparable to the plasmon wavelength

[3] Or better surface phonon polaritons.

the free-space wavevector. Therefore the dispersion becomes:

$$k_{\parallel} = \frac{\omega}{c}\sqrt{\frac{\varepsilon_1 \varepsilon_2}{\varepsilon_1 + \varepsilon_2}} \tag{3.1}$$

In a realistic situation losses (i.e. the imaginary part of the dielectric function) have to be taken into account, so $k_{\parallel}$ is a complex quantity: the plasmon wavelength is defined as $\lambda_{sp} = 2\pi/\mathrm{Re}k_{\parallel}$, while the propagation length is $L = 1/\mathrm{Im}k_{\parallel}$, i.e. the distance where the amplitude of the SP wave is decreased of $1/e$. In order to compare plasmon properties of different materials the inverse damping ratio $\gamma^{-1} = \mathrm{Re}k_{\parallel}/\mathrm{Im}k_{\parallel}$ is also used in literature as a quality factor.

We stress that the main feature of surface plasmons is the fact that they are non-radiative waves bound to the surface. This implies that in order to be excited the momentum mismatch between the plasmon and free-space light has to be overcome, for example with the use of a particular geometry or with the wavevector distribution in the near-field of a dipole. But this wavevector difference also leads to a reduction of the plasmon wavelength with respect to the wavelength of light at the same frequency in free space, paving the way to the miniaturization of photonic circuits. In addition, the electric field in the vertical direction decays exponentially away from the interface. These properties are general characteristics that apply also to the description of graphene plasmons, even if the energies, dispersion relation, and the typical values of field confinement are very different form the ones found in metal plasmonics, as we shall see in the next section.

Wavelength reduction and propagation length

In metal-plasmonics the frequencies of interest lie in the visible range, where it is possible to reach a compromise between propagation length and wavelength reduction (and field confinement). However, given the dispersion relation in Eq. 3.1, the highest wavelength reduction occurs at a frequency where light does not propagate (for ω_R such that $\varepsilon_2(\omega_R) = -\varepsilon_1$), while longer propagation lengths are obtained at frequencies with very little wavelength reduction.

To get an idea of the actual quantities, let us consider an ideal (perfectly flat) glass-silver interface (glass with refractive index $n = 1.5$ and silver with wavelength dependent permittivity taken from Babar & Weaver [2015]). In this case the resonance frequency is at $\lambda_0 = 360$ nm, and there the wavelength reduction is $\lambda_{sp}/\lambda_0 = 0.27$, while the propagation length is only $L_{sp} = 0.38\lambda_{sp}$, and $\gamma^{-1} = 2.39$. At $\lambda_0 = 750$ nm, the propagation length reaches $L_{sp} = 177\lambda_{sp}$, with $\gamma^{-1} = 1111.6$. But in this case the wavelength reduction is $\lambda_{sp}/\lambda_0 = 0.64$, so barely lower than the value due to the glass refractive index[4].

Plasmons in a thin slab

If instead of an infinite metal we consider a metallic slab of thickness d, we will have surface plasmons at the two metal-dielectric interfaces. For this more complicated system a convenient (and equivalent to what we did in the previous case) way to retrieve the surface plasmon dispersion is by looking at the poles of the reflection coefficient (valid for both p and s polarizations): $r_{s,p} = \frac{r_{1,2}+r_{2,3}e^{ik_{\perp 2}d}}{1+r_{1,2}+r_{2,3}e^{ik_{\perp 2}d}}$. For a slab of thickness smaller than the penetration depth in the metal, the surface plasmon modes couple and this results in greater wavelength reduction and increased field confinement. However, in the case of metals, drastically reducing the thickness can result in a change of the optical properties. Also, if we consider the scenario of high wavelength reduction, then the effect of radiative losses due to surface roughness can play a significant role.

3.2 Plasmons in 2DEGs and graphene

2-dimensional electron gases (2DEGs) are systems where the electrons are confined to two dimensions, with graphene being the ultimate example. Their properties have been experimentally studied in a variety of systems, including

[4] As initially pointed out by Jablan *et al.* [2009].

metal-insulator-semiconductor heterojunctions[5], semiconductor-semiconductor heterojunctions[6] and more recently oxide-oxide interfaces[7]. 2D plasmons in a solid-state device[8], a silicon inversion layer, were observed for the first time by FTIR in the 10-30 cm^{-1} ($\sim$ 0.3-0.9 THz) frequency range, at $\vartheta = 1.2$ K [Allen *et al.*, 1977].

Plasma oscillations in 2D systems involve all the conduction carriers in the material, so they are intrinsically different from surface plasmons, which involve only charge carriers at the surface of an otherwise unperturbed bulk material. This means that adding or removing electrons to the system strongly affects the 2D plasmon properties, therefore plasmon tunability is achieved by tuning the carrier density n. In addition, the 2D nature of the material implies a very tight vertical confinement of the plasmons. A sketch of the basic properties of 2D plasmons is shown in Fig. 3.1, where we depict the charge and electric field distribution in the 2D plane (Fig. 3.1a), the vertical field profile (Fig. 3.1b), and the plasmon dispersion (Fig. 3.1c).

Plasmon dispersion

A simple way to obtain the plasmon dispersion[9], following Jablan *et al.* [2009], is by matching the boundary conditions of a structure where a two dimensional film of surface conductivity σ lies between two dielectrics of permittivity ε_1 and ε_2. Equivalently, one can look for the poles of the Fresnel reflection

[5] a complete review is found in Ando *et al.* [1982]

[6] the observation of the fractional quantum Hall effect in AlGaAs/GaAs heterostructures lead to the 1998 Nobel Prize [Tsui *et al.*, 1982]

[7] more details in Hwang *et al.* [2012]

[8] Earlier studies reported 2D plasmon in the 2DEG at the surface of liquid He [Grimes & Adams, 1976]

[9] We note that an alternative way to derive the plasmon dispersion is to use hydrodynamics equations for the oscillation of the charge density as in A. N. Grigorenko , M. Polini [2012].

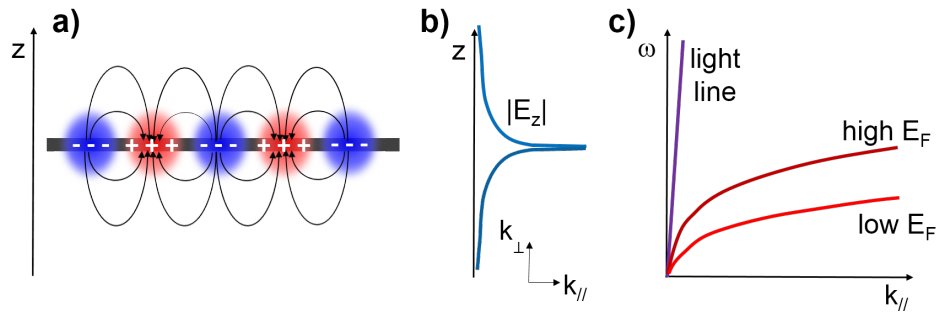

Figure 3.1: Sketch of the main features of graphene plasmons. a) amplitude (red and blue for positive and negative values) and field lines of the in-plane electric field. b) out-of-plane electric field confinement. c) plasmon dispersion.

coefficient r_p of such structure, where r_p is[10]

$$r_p = \frac{\varepsilon_2 k_{\perp 1} - \varepsilon_1 k_{\perp 2} + \frac{\sigma k_{\perp 1} k_{\perp 2}}{\varepsilon_0 \omega}}{\varepsilon_2 k_{\perp 1} + \varepsilon_1 k_{\perp 2} + \frac{\sigma k_{\perp 1} k_{\perp 2}}{\varepsilon_0 \omega}}$$

A good approximation for the conductivity is to use the Drude model, i.e. $\sigma = D\frac{i}{\omega + i/\tau}$, where D is the Drude weight, which is $D = \frac{e^2 n}{m^*}$ for a conventional 2DEG, and $D = \frac{e^2 E_F}{\pi \hbar^2}$ for graphene[11].

Clearly, in the case of graphene, the validity of the Drude model for the conductivity is limited to a range of energies where the interband transitions (for any $k_\parallel$, not only $k_\parallel = 0$) are not allowed. As we discuss more in detail later, this means that the Drude model can be used only in the region where the energy of the plasmon or/and incoming photon is comparable or smaller than

[10] For completeness we add that $r_s = \frac{k_{\perp 1} - k_{\perp 2} - \frac{\sigma k_0}{\varepsilon_0 c}}{k_{\perp 1} + k_{\perp 2} + \frac{\sigma k_0}{\varepsilon_0 \omega}}$.

[11] In this case m^* is the density dependent cyclotron mass $m^* = E_F / v_F^2$. This holds more in general for two dimensional system of Dirac fermions, which can be found for example in topological insulators. See Di Pietro *et al.* [2013] for more details on plasmons in such systems.

the Fermi energy: $E_{\text{ph}} \lesssim E_F$. More in general, the plasmon dispersion that we are deriving is valid only in the region free from interband and intraband transitions as depicted in Fig. 3.2a, for $k \ll k_F$.

Concerning the plasmon dispersion then, the starting point is the relation: $\varepsilon_1 k_{\perp 2} + \varepsilon_2 k_{\perp 1} + \frac{\sigma k_{\perp 1} k_{\perp 2}}{\varepsilon_0 \omega} = 0$. Then we consider the limit $k_\parallel \gg k_0$, therefore[12] $k_{\perp 1,2} \approx i k_\parallel$. In this way we arrive to $k_\parallel \approx i(\varepsilon_1 + \varepsilon_2)\varepsilon_0 \omega/\sigma$. If we consider the real part, which is related to the plasmon wavelength as we saw before, we obtain[13] :

$$\omega \approx \sqrt{\frac{k_\parallel D}{\varepsilon_0(\varepsilon_1 + \varepsilon_2)}} \tag{3.2}$$

The square root relation between frequency and wavevector is very peculiar of 2D plasmons[14]. This translates into the fact that the 2D plasmons can be very deeply subwavelength modes (i.e. the dispersion is very far away from the light line as shown in Fig. 3.1c), even if they are dispersive modes, i.e. $\frac{\partial \omega}{\partial k_\parallel} \neq 0$. They therefore allow a better trade-off between wavelength reduction (and field confinement) and propagation length, as we discuss for the case of graphene in the next section.

In order to excite 2D plasmons optically, as in the case of surface plasmons, one needs to match the momentum of light in free space and that of the plasmons. This can be achieved by breaking the symmetry of the 2D systems by engineering ribbons[15] (or other nanostructures) and shining far-field light perpendicularly polarised with respect to the longitudinal axis of the ribbons. This gives rise to a standing wave that forms across the ribbon when a resonance condition between the width w and the plasmon wavelength λ_p is matched ($w \approx \lambda_p/2$) [Nikitin *et al.*, 2012]. This has been shown in the case of 2DEG for THz [Allen *et al.*, 1977] and graphene for THz [Ju *et al.*, 2011] and MIR

[12] This means that the vertical confinement is simply $\delta \sim \lambda_{\text{sp}}/2\pi$.

[13] Some factors taking into account the finite size in real 2DEG systems are introduced in the plasmon dispersion when comparing it with experiments [Allen *et al.*, 1977].

[14] If we compare 2D plasmons with 3D (bulk) plasmons, we remark that the 3D plasma frequency is a fixed property of the solid, not depending on the wavevector.

[15] Either by cutting out a single ribbon from the 2D sheet, or by implementing a ribbon design on the doping pattern.

[Yan *et al.*, 2013; Brar *et al.*, 2013]. In addition, 2D plasmons can be launched by coupling the near-field radiation of an optical emitter to the 2D system. We discuss the case for graphene in the last section of this Chapter and we present experimental implementations in Chapters 4 and 5.

Comparison between graphene and 2DEG plasmons

Even starting from the same simple model for the plasmon dispersion given above, we can identify some important differences between conventional 2DEG plasmons and graphene plasmons. Most of them make graphene plasmons more appealing for technological applications. Indeed the fabrication and operation of graphene devices are simpler, and graphene plasmons cover a wider part of the electromagnetic spectrum. Indeed, we remark that plasmons in conventional 2DEGs have been observed in the THz range, while graphene plasmons have been demonstrated from the THz to the NIR [Ju *et al.*, 2011; Brar *et al.*, 2013; Fang *et al.*, 2013b; Tielrooij *et al.*, 2015b].

Dependence on the charge carrier density From Eq. 3.2, considering the expression for the Drude weight for 2DEGs, we obtain $\omega \sim \sqrt{n}$ for 2DEG plasmons. Instead, recalling Eq. 1.1, in the case of graphene we find $\omega \sim n^{1/4}$. This behaviour has indeed been observed with FTIR transmission measurements of graphene microribbons in the THz range [Ju *et al.*, 2011].

Achievable charge carrier density Even though the frequency dependence on n for graphene is weaker than for a 2DEG, graphene doping techniques are more flexible (see Chapter 2), therefore higher n, up to $\sim 10^{14}$ cm^{-2} can be achieved [Das *et al.*, 2008; Khrapach *et al.*, 2012]. This contributes to the observation of graphene plasmons at higher frequencies.

Effective mass In addition, for a broad range of n values typically reachable in 2DEG ($n \sim 10^{12}$ cm^{-2} for silicon inversion layers) at the same $k_{||}$ the frequency of graphene plasmons is generally higher due to a favourable difference in the effective mass: for a silicon inversion layer, $m^* \approx 0.21\, m_0$,

with m_0 the electron mass, while for graphene $m^* = E_F/vf^2 \approx 0.02m_0$ for $n \sim 10^{12}\text{cm}^{-2}$.

Substrate The versatility in graphene fabrication allows the use of different substrate materials, also with a different permittivity than that used in other 2DEGs.

Temperature Graphene plasmon resonances are commonly observed at room temperature, while 2DEG experiments are generally performed at low temperature.

Ambipolarity The possibility of gating graphene ambipolarly, unlike other 2DEG systems, means that either electron or hole plasmons can be excited.

Two dimensionality Furthermore, the real two dimensionality of graphene leads to a higher confinement. No finite-size effects should be added in the dispersion of an actual 2DEG system with thickness d to match with experiment, as in the case of real 2DEGs. [Allen *et al.*, 1977].

3.3 Graphene plasmonics

The relationship between the plasmon wavelength λ_p and the free space wavelength λ_0, after some manipulation of Eq. 3.2 becomes:

$$\lambda_p \approx \alpha\lambda_0 \frac{E_F}{E_{\text{ph}}} \frac{4}{\varepsilon_1 + \varepsilon_2}. \tag{3.3}$$

Since E_F is tunable, it can adjusted to be $E_F \sim E_{\text{ph}}$ to achieve a smaller λ_p. In addition, as $\varepsilon_1 + \varepsilon_2$ is generally not much different from 4 (for example for graphene on SiO_2 is ∼5), we see that λ_0/λ_p is on the order of $1/\alpha$ so $\gtrsim 100$. Therefore very high wavelength reduction and strong field confinement can be achieved with graphene plasmons.

Plasmon losses

Concerning the plasmon propagation length and lifetime in the region where the resonance is well-defined, the simplest evaluation considers the DC scattering time τ_{DC}. This first approximation has to be modified when dealing with frequencies above the graphene optical phonon at 0.2 eV, where plasmons have a relaxation pathway into an optical phonon and an electron-hole pair [Jablan *et al.*, 2009; Yan *et al.*, 2013]. However, recent studies have shown that τ_{DC} and the plasmon lifetime are not necessarily correlated [Fei *et al.*, 2012; Principi *et al.*, 2013b,a], and that intrinsic acoustic phonons can strongly affect the plasmon lifetime [Principi *et al.*, 2014].

While a full treatment of plasmon damping mechanisms is beyond the scope of this thesis, we highlight that experimentally on hBN-graphene-hBN heterostructures a propagation length of $\sim 4\ \lambda_p$ has been observed, remarkably high considering that it is accompanied by a ~ 150 times reduction in wavelength in the MIR at $\lambda_0 \approx 10.6$ [Woessner *et al.*, 2014]. For such devices the quality factor γ^{-1} is 25, and the plasmon lifetime[16] τ_p has been found to be 500 fs, more than one order of magnitude higher than for silver [Lamprecht *et al.*, 1999].

[16] $\tau_p = (\mathrm{Im}\, k_\parallel)^{-1}/v_g$, where the group velocity v_g is $(d\,\mathrm{Re}\, k_\parallel/d\,\omega)^{-1}$

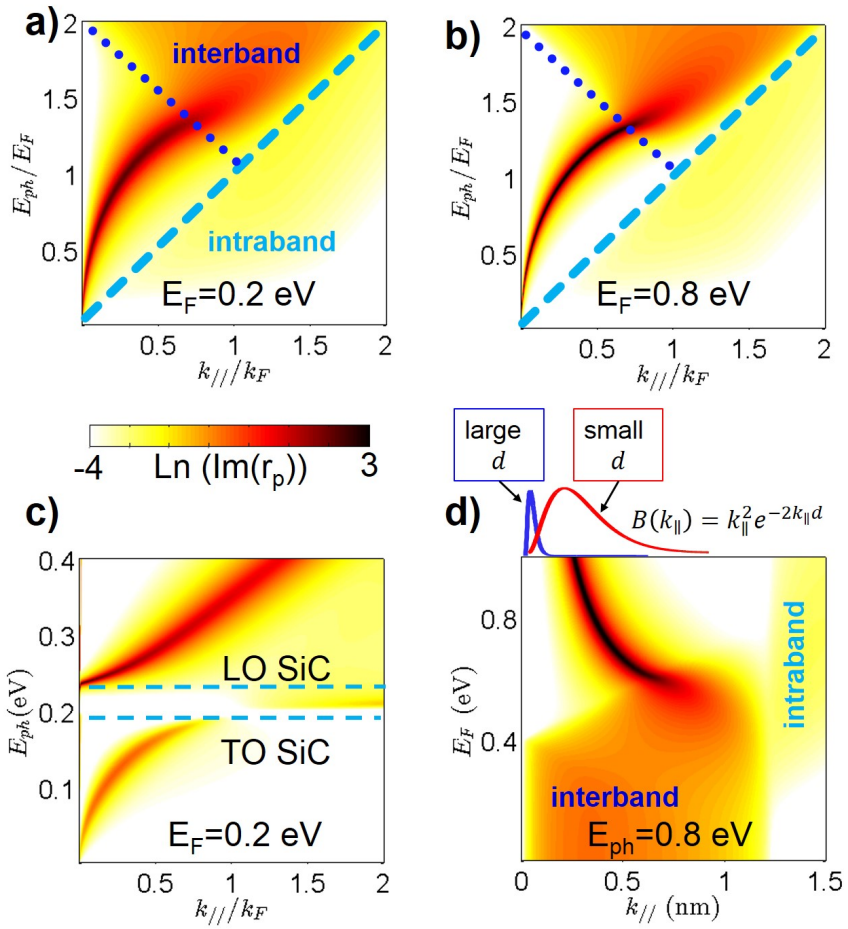

Figure 3.2: Imaginary part of r_p: a,b) as a function of parallel wavevector and incoming photon energy for suspended graphene with E_F=0.2 eV and E_F=0.8 eV. c) for graphene on SiC, with E_F=0.2 eV. The dashed lines indicate the frequencies of the transverse optical and the longitudinal optical (LO) phonons in SiC. d) as a function of Fermi energy for E_{ph} = 0.8 eV. On top:, sketch of the wavevector distribution for dipoles at different distances d from the graphene.

Visualizing the plasmon dispersion beyond Drude

As previously mentioned, simply considering the Drude model is not sufficient to get the whole picture, which must include plasmon losses due to the excitation of electron-hole pairs. Indeed, graphene plasmons are long-lived excitations only in the region where decay pathways via interband or intraband transition are forbidden.

Several theoretical works have studied 2D plasmons in graphene analysing the self-consistent linear response function[17] in the random phase approximation [Wunsch *et al.*, 2006; Hwang & Das Sarma, 2007]. As a way to visualise the plasmon dipsersion and losses, in Fig. 3.2 we present, following García de Abajo [2014], the loss function, i.e. the imaginary part of the reflection coefficient r_p for p-polarized light, using the $k_\parallel$ dependent conductivity $\sigma = \sigma(k_\parallel, \omega)$.

In Fig. 3.2a,b we show the loss function as a function of photon energy and wavevector for two different values of the Fermi level. We see that in the triangular area where both interband and intraband transitions are forbidden, there is a resonance that follows the square root behaviour previously derived. For higher values of photon energy and wavevector, however, the behaviour changes and the resonance is strongly suppressed. We note the fact that the resonance, even in the damping region, can always be found above the $E_{\mathrm{ph}}/E_F = k_\parallel/k_F$ diagonal line, which is a direct consequence of the $k_\parallel$ dependence of the conductivity.

In Fig. 3.2c we instead analyse the effect of a frequency dependent permittivity of a substrate. In this case plasmon-phonon hybridization occurs, therefore modifying the simple square root dispersion, as shown in the case

[17] The response of an electron system to an external potential is given in the Fourier space by $\chi_{\mathrm{ext}} = \frac{\chi}{1-V\chi}$, where χ is the response to the full (external + screening) potential, and V is the Fourier transform of the electric potential. Plasmons are self-sustained oscillations of the system, so they occur for zero external potential, i.e. they can be found by looking at the poles of χ_{ext}. This is generally implemented by using χ_0 the instead of χ, where χ_0 is calculated taking into account the lowest order of electron-electron interactions. Therefore plasmons are investigated by looking at the poles of $\chi_{\mathrm{RPA}} = \frac{\chi_0}{1-V\chi_0}$.

of a SiC substrate. Such behaviour has been experimentally shown by several experiments using different techniques, such as s-SNOM [Fei *et al.*, 2011; Chen *et al.*, 2012] and FTIR [Yan *et al.*, 2013; Brar *et al.*, 2013].

Finally, in Fig. 3.2d we present the plasmon resonance behaviour when the photon energy is fixed and E_F is varied, as in the experiments presented in Chapter 4. On top, we show the wavevector distribution for a dipole placed at a distance d from the graphene plane [18], peaked at $k_{||} = 1/d$, for two different values of d. Clearly, for small enough d the plasmon resonance can be excited, as discussed in more detail in the following section.

3.4 Emitter-graphene coupling

As pointed out by Purcell back in 1946, the spontaneous emission (decay) rate of an emitter can be modified by varying the emitter environment, thus changing the local density of optical states (LDOS) which determines the interaction between the emitter and the surroundings [Purcell, 1946]. This topic has been the subject of extensive studies aiming to unravel fundamental properties of light-matter interaction.
In analogy to the local density of states used for the characterization of electrons in solids, the LDOS can be defined as a sum over photon states of energies ω_j [Agarwal, 1975; Glauber & Lewenstein, 1991; Di Stefano *et al.*, 2010]:

$$\mathrm{LDOS} = \sum_{\mathrm{j}} |\mathbf{E}_{\mathrm{j}}(\mathbf{r}) \cdot \hat{\mathrm{n}}|^2 \delta(\omega - \omega_{\mathrm{j}}) \tag{3.4}$$

where $\mathbf{E}_j(\mathbf{r})$ is the normalized electric field at the position $\mathbf{r}$, and $\hat{n}$ the unit vector along which to project the LDOS, which has to be selected since photons are vectorial quantities (as opposed to the scalar case for electrons).

A modification of the decay rate of an optical emitter by altering the LDOS has been realised in a variety of ways as sketched in Fig. 3.3, and can be de-

[18] The same function can be used to model the wavevector distribution in the near field that arises from illumination of a metallized AFM tip of radius d [Fei *et al.*, 2011].

tected by fluorescence measurements. For example, the emitter lifetime can be manipulated by placing an emitter at different distances from a metallic surface, as shown on right of Fig. 3.3 from Amos & Barnes [1997]. Many other systems have also been used, including metallic nanostructures [Novotny & van Hulst, 2011], optical cavities[Gérard *et al.*, 1998; Raimond *et al.*, 2001; Englund *et al.*, 2007; Hennessy *et al.*, 2006], and photonic crystals Lodahl *et al.* [2004]; Englund *et al.* [2005]. Generally in these implementations the decay rate changes with respect to the decay rate in vacuum are determined by the geometry and the kind of materials used with limited tuning possibilities.

Instead, graphene enables *in situ* electrical control of the decay rate of an emitter placed at a subwavelength distance from the graphene sheet. The emitter energy can be channelled into different pathways depending on the graphene Fermi energy, therefore tuning the LDOS that govern the emitter's relaxation, as we will show in Chapter 4.

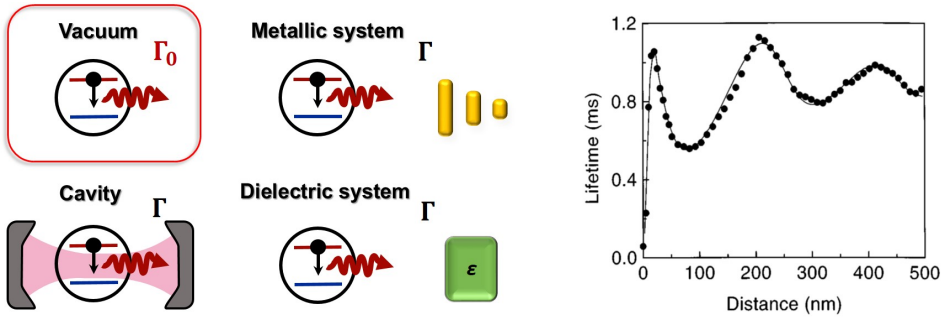

Figure 3.3: Left: sketch of modification of an optical emitter decay rate by changing the emitter environment. Right, image from Amos & Barnes [1997]: measured (black dots) and calculated (black line) lifetime of Eu^{3+} ions as a function of distance from a 200 nm thick silver mirror, showing strong quenching by plasmons below 30 nm, and damped oscillations over 30 nm. The lifetime of the Eu^{3+} ions was obtained from time resolved fluorescence measurements [19], exciting the sample with 5 ns pulses of UV light and collecting the fluorescence at 614 nm.

[19] In a similar fashion to the experiments presented in Chapter 4.

Fluorescence near interfaces

An exhaustive review on fluorescence near interfaces can be found in Barnes [1998], while a complete treatment of spontaneous decay and of dipole emission close to a surface is given in Novotny & Hecht [2006]. Here, we highlight the most important concepts in the classical and quantum treatment of spontaneous emission, following these texts.

In the classical description, the power radiated by a dipole with dipole moment $\mathbf{d}$ is given by:

$$P = \frac{\omega}{2}\mathrm{Im}\{\mathbf{d}^* \cdot \mathbf{E}(\mathbf{r})\}$$

where $\mathbf{E}(\mathbf{r})$ is the electric field at the dipole position. In a non homogeneous environment, $\mathbf{E}(\mathbf{r})$ can be split in two components:

$$\mathbf{E}(\mathbf{r}) = \mathbf{E}_\mathrm{p}(\mathbf{r}) + \mathbf{E}_\mathrm{ind}(\mathbf{r})$$

i.e. the primary field radiated by the dipole $\mathbf{E}_\mathrm{p}(\mathbf{r})$ and the induced field $\mathbf{E}_\mathrm{ind}(\mathbf{r})$ due to the scattering from the environment (for example in the presence of an interface). Therefore:

$$P = P_\mathrm{p} + \frac{\omega}{2}\mathrm{Im}\{\mathbf{d}^* \cdot \mathbf{E}_\mathrm{ind}(\mathbf{r})\}$$

where

$$P_\mathrm{p} = \frac{|\mathbf{d}|^2}{4\pi\varepsilon_0\varepsilon}\frac{\omega k^3}{3}$$

is the power radiated by a dipole in an homogeneous environment of dielectric constant ε.
In the quantum treatment of the spontaneous emission, we start from the Fermi's golden rule. For the decay rate Γ we have:

$$\Gamma = \frac{2\pi}{\hbar^2}\sum_f |\langle f|\hat{H}|i\rangle|^2 \delta(\omega_i - \omega_f)$$

where the interaction Hamiltonian of the system is given by $\hat{H} = -\hat{\mathbf{d}}\cdot\hat{\mathbf{E}}$. This means that $\Gamma \sim |\mathbf{d}|^2 \times \mathrm{LDOS}$, and for an emitter placed in vacuum the decay is

simply given by:

$$\Gamma_0 = \frac{\omega^3 |\mathbf{d}|^2}{3\pi\varepsilon_0 \hbar c^3}$$

Very importantly, it can be shown that:

$$\frac{\Gamma}{\Gamma_0} = \frac{P}{P_0}$$

where P_0 is the power radiated by a dipole (P_p) in vacuum. Therefore one can obtain the (quantum) decay rate Γ from the classical equivalent description of the dipole.

In the relevant case of a dipole in vacuum close to a surface with reflection coefficients r_s and r_p one obtains:

$$\frac{\Gamma}{\Gamma_0} = 1 + \frac{3}{4k_0^2|\mathbf{d}|^2} \int_0^\infty \mathrm{Re}\Big\{\big[|\mathbf{d}_\parallel|^2(k_0^2 r_s - k_\perp^2 r_p) + 2|\mathbf{d}_\perp|^2 k_\parallel^2 r_p\big]\frac{e^{2ik_\perp z}}{k_\perp}\Big\} k_\parallel dk_\parallel \quad (3.5)$$

From inspection of this formula we can see that if the dipole is at a subwavelength distance from the surface, and therefore $k_\parallel \gg k_0$, only r_p is relevant and the Γ is affected by the coupling of the dipole with evanescent waves at the surface. Instead for $k_0 \gg k_\parallel$ we retrieve the oscillatory behaviour shown in Fig. 3.3.

Effect of graphene on a nearby emitter

Now we can apply Eq. 3.5 to study the decay rate of an emitter close to a graphene sheet. In Fig. 3.4 we show examples for the case of emitters close to a graphene sheet in vacuum obtained using software written by Prof. García de Abajo that integrates Eq. 3.5 and also calculates the graphene optical conductivity, . We note that here we used the long wavelength limit of the conductivity ($\sigma(k_\parallel = 0, \omega)$), which gives good agreement with the experimental results presented in the next chapter. We point out however that the full $k_\parallel$ dependence of σ should be taken into account if a quantitative treatment is sought when the limit $k_\parallel \lesssim k_F$ is not valid.

In Fig. 3.4a we present a sketch of the main results: when an emitter is close to a graphene sheet, its decay rate can be varied by varying the graphene Fermi level. In particular, the emitter-graphene coupling can be tuned so that the decay occurs in three main regimes: the excitation of an electron-hole pair in graphene, the emission of a photon, and the excitation of a plasmon [Koppens *et al.*, 2011; Nikitin *et al.*, 2011; Velizhanin & Efimov, 2011].

In Fig. 3.4b we show a comparison of the decay rate as a function of Fermi energy for three different emitters, with emission frequency in the visible, NIR and MIR. The three curves are chosen so that the decay rate value due to the excitation of electron-hole pairs is the same. As we can see this happens for different emitter-graphene distances depending on the emitter emission frequency. We observe a very strong enhancement of the decay rate with respect to the decay rate in vacuum. In addition, we see that the peak related to the coupling with the plasmon resonance is shifted to higher Fermi energies for higher frequencies of the emitters, in accordance with the previously discussed properties of graphene plasmons.

These features are even more clear when we consider the three emitters separately and analyse the decay rate at different distances (2 to 56 nm) from the graphene sheet, as shown in Fig. 3.4c,d,e. Here, the distinctive distance dependence of the different regimes emerges. The enhancement of Γ due to the non-radiative decay through the generation of electron-hole pairs is still present at relatively long distances, while the plasmon coupling is more relevant when the emitter is closer to the graphene, as the plasmon field decays exponentially from the surface.

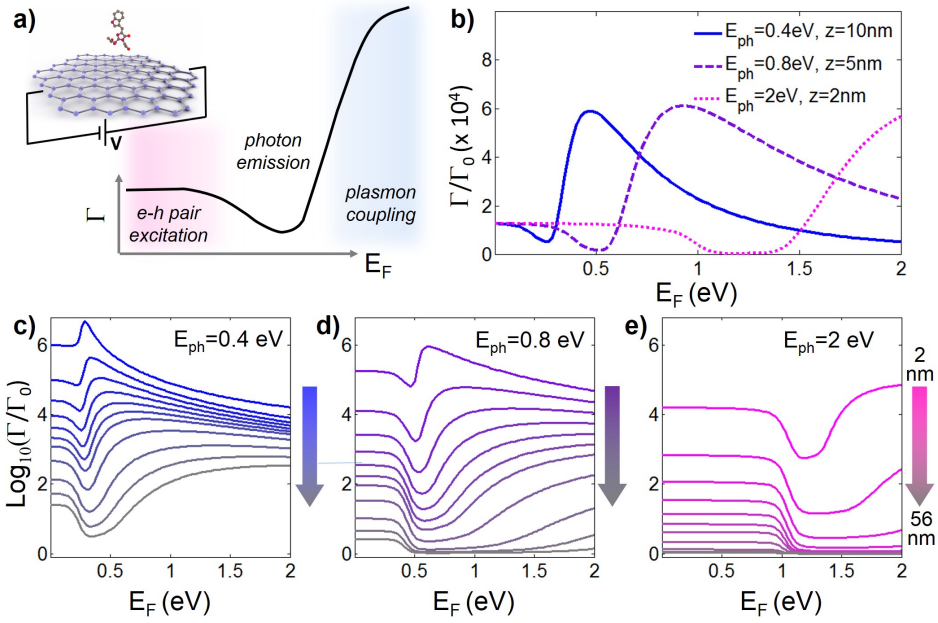

Figure 3.4: a) Sketch of a molecule close to a gated graphene sheet (3D image courtesy of Dr. R. Sapienza) and of the typical decay rate of an emitter close to graphene, highlighting the 3 different regions of e-h pair generation, photon emission, and plasmon coupling. b) Comparison between the decay rates of emitters with different emission energies at subwavelength distances to graphene (E_{ph}= 0.4, 0.8 and 2 eV, corresponding to λ= 3 μm, 1550 nm and 620 nm) as a function of the graphene Fermi energy; the distances are chosen so that the decay rate due to e-h pair excitations is the same. c,d,e) Decay rate as a function of graphene Fermi energy for a dipole emitting at E_{ph}= 0.4 (c), 0.8 eV (d) and 2 eV (e), at distances ranging from 2 nm (bright colour) to 56 nm (grey). The curves are shown for the distances (in nm): 2, 5, 8, 11, 14, 17, 20, 26, 36, 46, 56.

4

Electrical control of energy flow from an optical emitter

Graphene-mediated electrical control over the energy relaxation pathways of erbium ions is demonstrated. We measure the fluorescence from erbium emitters placed at a sub-wavelength distance from a graphene sheet while varying the graphene Fermi energy with a top gate. The energy flow from the emitter can be tuned to three regimes: excitation of electron-hole pairs in graphene (low doping), photon emission (intermediate doping) and excitation of near-infrared graphene plasmons (high doping).

In this Chapter we show an *in-situ* electrical control of the local density of optical states (LDOS) which governs the interactions between an emitter and its environment. As we mentioned in the previous Chapter, graphene offers the possibility to control *in-situ* the LDOS since the optical excitations that occur for a specific emission energy of a nearby emitter can be electrically modified. Indeed, from the gapless nature and the electrostatically tunable Fermi energy it follows that graphene can effectively behave as a semiconductor, a dielectric, or a metal. In this Chapter we exploit these material characteristics to electrically control the relaxation rate and energy transfer processes of a dipolar emitter at subwavelength distance from the graphene, that can be tuned through three regimes. For low graphene Fermi energy, the dipolar emitter can decay exciting electron-hole pairs in graphene. When the Fermi energy is increased and Pauli blocking occurs, the emitters decays through photon emission. Finally, for higher Fermi energy, graphene plasmons are excited.

Specifically, we demonstrate *in-situ* tuning of the relaxation pathways from optically excited erbium ions, emitters for near-infrared light that are used as a gain medium in telecommunication applications [Polman, 1997; Snoeks *et al.*, 1995]. The ability to electrically tune the energy flow from the erbium ions and to excite extremely confined near-infrared graphene plasmons opens new avenues in the fields of optical communications and active photonics.

4.1 Experimental implementation

To demonstrate the *in-situ* tunable coupling between emitters and graphene, we use fluorescence as a probe for the energy relaxation pathways of hybrid erbium–graphene devices.

Devices

The devices consist of graphene deposited on a thin layer (< 60 nm) of Er^{3+} emitters embedded in an oxide matrix on top of a silicon substrate, as shown

in Fig. 4.1a. The erbium emitters are in subwavelength proximity of the graphene, therefore the physics are governed by their near-field coupling.

We have chosen erbium due to its technological relevance in telecommunication applications [Polman, 1997] and because the emission energy E_{em} of 0.8 eV is relatively low compared to most emitters. In this way, using a polymer electrolyte top gate as described in Chapter 2, we can access the regime where $E_F > E_{\mathrm{em}}/2$, which is required for strong modification of the energy transfer rate and for access to the plasmon regime.

We employ two different kinds of erbium emitter layers from two different sources [1], obtaining qualitatively the same results. One type of device contains a layer of erbium-doped yttria (Er^{3+}:Y_2 O_3, 1-3% atom. concentration) with a thickness of 45–60 nm produced using Metal Organic Decomposition [Andriamiadamanana *et al.*, 2013] and another type contains erbium in a SiO_2 matrix (<1% atom. concentration) with a thickness of ~25 nm, fabricated using co-sputtering [Cesca *et al.*, 2012].

Concerning the graphene device fabrication, we use CVD graphene grown on copper [2] transferred on top of the erbium layer with the wet transfer method described in Chapter 2. Laser writing optical lithography is used to pattern graphene into micron-scale Hall bars and to define the electrical contacts and the gates. To get a longer stability of the samples over time, we often protected the Ti(2 nm) /Au (100 nm) electrical contacts to the graphene with few nanometres of SiO_2 deposited with electron-beam evaporation. For the gates we either used the same metal as for the electrical contacts to the graphene, or platinum to minimize the chemical reactions with the electrolyte. The devices are designed such that the polymer gate leads are within 10 microns of the Hall bar with the intention that the proximity will provide more effective doping as less of the field is screened by the leads between the graphene and the gate contact.

[1] CNRS-Chimie Paristech, France and University of Padua, Italy.
[2] Source: Spanish company Graphenea.

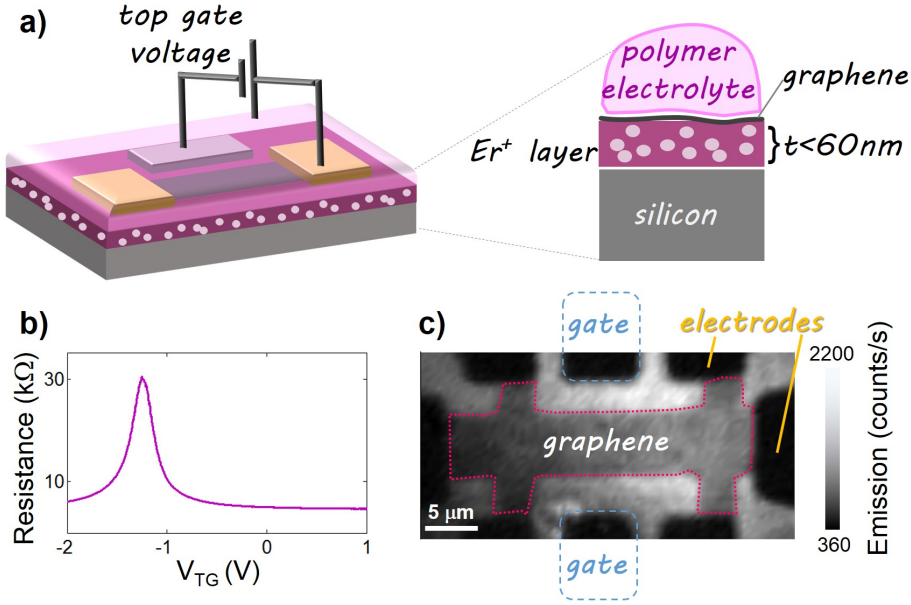

Figure 4.1: a) Sketch of the device geometry. On the right the layer structure of the sample is depicted. The layer with the emitters has a thickness t much smaller than the emission wavelength. b) Typical resistance curve of a device gated with the polymer electrolyte technique. c) Typical fluorescence emission map of the sample at 1.5 μm, obtained raster scanning the device with 532 nm light focused to ∼1 μm. The graphene is shaped into an Hall bar, as indicated by the magenta dotted line. In the graphene area a fluorescence quenching is observed. The black areas correspond to the metallic gates and electrodes.

Experimental setup

We excite erbium emitters with green light and measure the near-infrared erbium emission using a home-built scanning confocal microscope setup. The excitation and fluorescence collection are performed from the top of the sample[3], using an infrared objective (Olympus LCPLN-50*X*-IR, numerical aperture 0.65). The sample is illuminated with ~ 1 mW of focused CW light at 532 nm and the 1.5 μm emission of the photoexcited Er^{3+} ions is collected, spectrally filtered (long wave pass filters of 1100 and 1400 nm) and directed into a near-infrared (near-IR) single photon detector (Princeton Lightwave PGA-600 or ID Quantique id210) through an optical fiber. Spatially resolved fluorescence maps like the one shown in Fig. 4.1d are obtained by raster scanning the device with the focused excitation beam using galvo mirrors. We estimate the spatial resolution to be $\sim$1 μm.

The sample is mounted in a vacuum chamber that is kept at a pressure of 5-10 mbar for optimal operation of the polymer electrolyte gate. The device is connected to a number of electrical wires that allow the application of a potential difference between graphene and the gate (on the order of 1 V), in order to control the Fermi energy, as well as a potential difference over the graphene sheet (typically 10 mV), in order to measure the device resistance at the same time as the emission is measured. A typical resistance curve of a device as a function of the applied top gate voltage is presented in Fig. 4.1c. The topgate was generally swept at a 10 mV/s rate in order to minimize possible hysteresis and risks of damaging the devices.

4.2 Electrical control

As shown in Fig. 4.1d, the fluorescence F_g for emitters in the region with graphene is quenched by about a factor 2-3 compared to the fluorescence from erbium emitters F_0 without graphene on top. Similar quenching was observed earlier for visible light emitters coupled to graphene and attributed to the en-

[3]The polymer electrolyte is transparent at the wavelengths of interest.

ergy transfer from the emitters into excited e-h pairs [Treossi *et al.*, 2009; Chen *et al.*, 2010; Gaudreau *et al.*, 2013]. Here, graphene effectively behaves as a semi-conductor. We now show the ability to electrically control the emitter–graphene coupling, and thus the energy flow pathways, by tuning the Fermi energy of the graphene using the gate voltage of the polymer electrolyte.

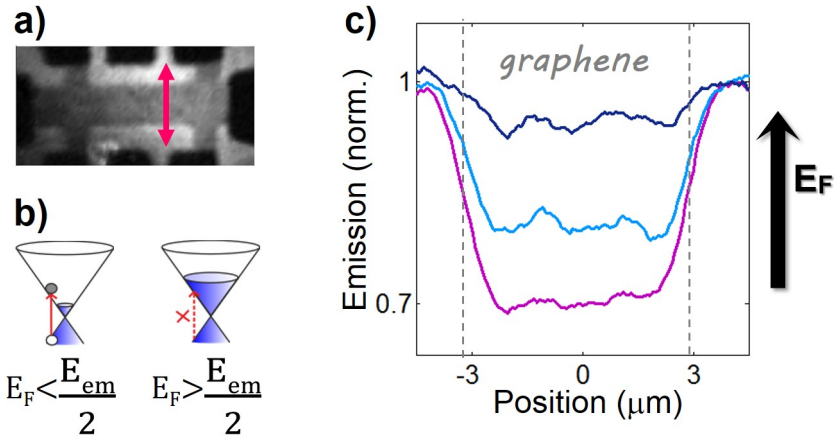

Figure 4.2: a) Fluorescence emission map, where the magenta arrow indicates the direction of the linecuts taken as a function of topgate voltage. b) Scheme of the Pauli blocking process. c) Electrical control of the emission quenching: as the Fermi energy is increased the graphene fluorescence quenching is reduced. Violet, cyan and blue line correspond to increasing $V_{TG} - V_D$.

Tunable fluorescence quenching

In order to demonstrate the graphene-mediated electrical control over the emitter relaxation pathways we monitor the fluorescence emission as we change the graphene Fermi energy. We can consider a line across the graphene, as shown in Fig. 4.2a, and monitor the fluorescence along that line at different applied top gate voltages V_{TG}. The result, for a device with ~ 60 nm Er^{3+}:Y_2O_3, is shown in Fig. 4.2c. For V_{TG} close to V_D (violet trace) the emission in the gra-

phene region is quenched. Increasing the Fermi energy the erbium emission in the graphene region approaches the erbium emission outside the graphene region, that instead remains unaffected by the gate voltage.

As depicted in Fig. 4.2b, reaching $E_F > E_{em}/2$ marks the transition from the *e-h pair excitation* regime to the *photon emission* regime. The former regime corresponds to a strong decrease in erbium emission due to the non-radiative energy transfer to electron hole pairs in graphene. In the latter regime instead, the graphene sheet is almost invisible for the emitter, leading to emitter fluorescence as if the graphene were not there. We note that the fluorescence in the graphene region never fully reaches the value outside the graphene. This can be ascribed to the non-vertical transitions, as explained in more detail in the section 4.3.

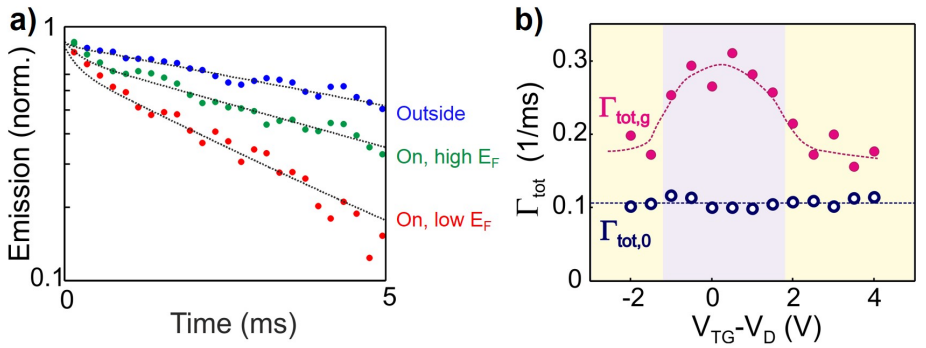

Figure 4.3: a) Normalized emission as a function of time (logarithmic scale) after a 10 ms light pulse for positions inside and outside the graphene for device containing a ~25 nm thick layer of SiO_2 with erbium ions. The dotted lines represent the fits to obtain the decay rate. b) Decay rate outside $\Gamma_{tot,0}$ and inside $\Gamma_{tot,g}$ the graphene as a function of the topgate voltage. The violet and yellow areas represent the region of e-h excitation and photon emission respectively.

Tunable lifetime

The key signature of electrical control of the LDOS is tunability of the decay rate of the erbium emitters, and to demonstrate this, we perform time-resolved fluorescence measurements. The typical emission as a function of time after a 10 ms pulse is shown in Fig. 4.3a for a location outside the graphene region (decay rate $\Gamma_{\mathrm{tot,0}}$), and for a location inside the graphene region (decay rate $\Gamma_{\mathrm{tot,g}}$) for different values of the graphene Fermi energy. We fit these curves with bi-exponential decays and we retain the longest lifetime to determine the decay rate $\Gamma_{\mathrm{tot,0}}$.

The resulting emitter lifetimes, extracted from exponential fits to the decay curves, are shown as a function of gate voltage in Fig. 4.3b. For the energy range around the charge-neutrality point $E_F < E_{\mathrm{em}}/2$, $\Gamma_{\mathrm{tot,g}}$ is about a factor three higher than $\Gamma_{\mathrm{tot,0}}$, while $\Gamma_{\mathrm{tot,g}}$ approaches $\Gamma_{\mathrm{tot,0}}$ for $E_F > E_{\mathrm{em}}/2$. Thus for $E_F > E_{\mathrm{em}}/2$ energy relaxation occurs mainly through photon emission, whereas for $E_F < E_{\mathrm{em}}/2$ a parallel energy relaxation channel opens up, which leads to e-h pair excitation in graphene. Such *in-situ* control of the relaxation rate is a unique feature of this hybrid system.

4.3 Comparison with theory

In order to compare our experimental results with the theoretical model of emitter-graphene coupling described in the previous Chapter, we choose to monitor the fluorescence emission at single selected positions inside and outside the graphene. In this way we are able to sweep the top-gate and avoid hysteresis or shifts in the doping level that might result when a fixed voltage is applied for a long time, as in the case of the spatial linecuts or when measuring the lifetime.

Intuitively, the fluorescence contrast η between a position inside and outside the graphene sheet is related to the ratio of the emitter decay rates in the two positions, $\eta = F_{\mathrm{g}}/F_0 \approx \Gamma_{\mathrm{tot,0}}/\Gamma_{\mathrm{tot,g}}$. In general, the decay rate of an emitter is given by a radiative and a non-radiative contribution, i.e. $\Gamma_{\mathrm{tot}} = \Gamma_{\mathrm{rad}} + \Gamma_{\mathrm{nr}}$.

In the case of erbium emitters, the decay rate in the absence of graphene is $\Gamma_{tot,0} = \Gamma_{rad} + \Gamma_{loss}$, where Γ_{rad} is the radiative decay rate considering the dielectric environment, and Γ_{loss} an intrinsic loss term in the thin emitter film. This intrinsic loss mechanism is likely caused by energy scavenging of (surface) impurities. In the presence of graphene there is another term due to the emitter-graphene coupling: $\Gamma_{tot,g} = \Gamma_{rad} + \Gamma_{loss} + \Gamma_{e-g}$.

Emitter-graphene coupling

As the first ingredient for a model of the fluorescence is Γ_{e-g}, we briefly recall the theory of the emitter-graphene coupling presented in the previous Chapter. As we discussed, the decay rate is proportional to the electric field that is induced by a dipole[4] on itself due to its environment [Novotny & Hecht, 2006]. The latter is well described through the Fermi-energy-dependent graphene conductivity $\sigma(E_{em}, E_F)$ at fixed emission energy $E_{em} = 0.8$ eV, as well as by the substrate permittivity ϵ. To calculate Γ_{e-g} we then use Eq. 3.5, taking a weighted sum of the rate over emitter dipole orientations. In the limit where the distance d between the dipole and graphene is smaller than the emission wavelength, Eq. 3.5 reduces to

$$\frac{\Gamma_{e-g}}{\Gamma_{rad}} - 1 \propto \int_0^\infty d\,k_\parallel B(k_\parallel) \mathrm{Im}\{r_p\}$$

where r_p is the Fresnel reflection coefficient of the interface, and thus contains the graphene conductivity $\sigma(E_{em}, E_F)$. The bell-shaped weight function $B(k_\parallel) = k_\parallel^2 e^{-2k_\parallel d}$, peaked at $k_\parallel = 1/d$, represents the distribution of the wave vectors that contribute to the emitter-graphene coupling when they are separated by a distance d. In our samples the emitters are distributed along the thickness of the oxide film, therefore to model the fluorescence and the decay rate in the presence of graphene we should integrate over the entire thickness,

[4] We note that although the electric or magnetic nature of the dipole associated with erbium emission is still a subject of investigation [Li, 2014], the distance and orientation averages lead to the same emission rates, when assuming the erbium emission is described by either an electric dipole or a magnetic dipole

considering emitters at different distances from the graphene sheet.

Experimental determination of loss and saturation parameters

In order to correctly model the fluorescence one has to take into account the presence of intrinsic losses and the creation of an excited state population, leading to a fluorescence saturation, not negligible for high pump power [Altkorn & Zare, 1984; Engh & Farmer, 1992; Visscher *et al.*, 1994].

The relationship between the fluorescence and the decay rate is given by:

$$F = \frac{A}{1 + \frac{\Gamma_{\text{tot}}/\Gamma_{\text{rad}}}{P_{\text{exc}} C_{\text{exc}}/\Gamma_{\text{rad}}}} \tag{4.1}$$

where A is a constant that takes into account the radiative decay rate Γ_{rad} and the collection efficiency of the emission. P_{exc} is the excitation power, and C_{exc} is the excitation constant that describes the creation of excited state population. Therefore, to obtain a theoretical curve for the erbium fluorescence in presence of graphene, the calculation of the emitter-graphene coupling $\Gamma_{\text{e-g}}$ is not enough, but we should also input values for the loss rate Γ_{loss} and the excitation term $P_{\text{exc}} C_{\text{exc}}$.

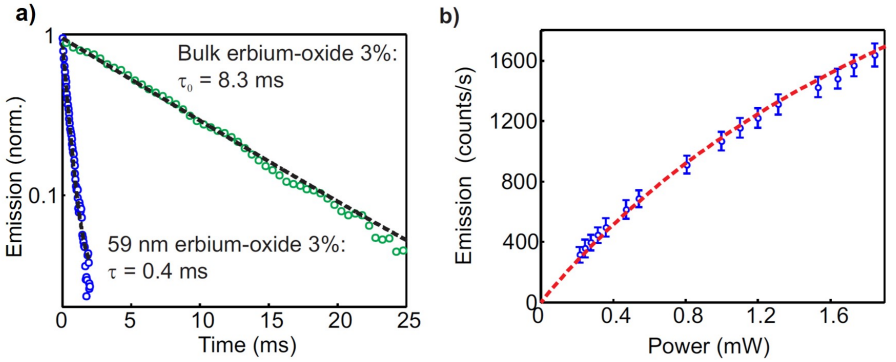

Figure 4.4: a) Normalized emission of Er^{3+}:Y_2O_3 as a function of time (logarithmic scale) after a 10 ms light pulse for the case of bulk (green circles) and for a ∼60 nm thick film (blue circles). The black dashed lines are the fits to extract the lifetimes. b) Emission (F_0) as a function of power. The red dashed line is a fit with Eqn. 4.1.

We focus on the devices where the erbium ions are embedded in yttria, and we experimentally determine these two parameters. We retrieve the loss rate comparing the decay rate outside the graphene region in the thin oxide film with the decay rate of erbium emitters in bulk oxide, which we take as our Γ_{rad}. In Fig.4.4a we show the emission as a function of time for the two cases. We find a 'bulk' lifetime of ∼8.3 ms, very similar to values found in the literature [Polman, 1997]. In contrast, we find a 'film' lifetime of ∼0.4 ms. This means that $\Gamma_{tot}/\Gamma_{rad} = 1 + \Gamma_{loss}/\Gamma_{rad} \approx 21$. Therefore we use the value $\Gamma_{loss}/\Gamma_{rad} = 20$ as input for our theoretical calculation of the emission as a function of Fermi energy.

The last input parameter that we need is $P_{exc}C_{exc}/\Gamma_{rad}$. This parameter describes how strongly we are exciting the erbium layer. We insert $\Gamma_{tot,0}/\Gamma_{rad} = 1 + \Gamma_{loss} = 21$ in Eq.4.1, and then fit the dependence of the fluorescence (again outside the graphene region) on the excitation power P_{exc} (see Fig.4.4b). In this way we obtain $C_{exc} \approx 7 \cdot 10^3$ $s^{-1}W^{-1}$. With the excitation power at the sample $P_{exc} \approx 1.9$ mW we find $P_{exc}C_{exc}/\Gamma_{rad} \approx 13.5$.

Experimental vs theoretical curves

Having all the ingredients to model the fluorescence, in Fig.4.5a we show the experimentally obtained erbium fluorescence contrast $\eta = F_g/F_0$ as a function of E_F, compared with the theoretical results. The device has a ∼60 nm thick layer of Er^{3+}:Y_2O_3 and the Fermi energy is calibrated through Hall measurements. The theoretical curve is calculated by integrating the fluorescence of dipoles at distances between 2 and 50 nm from the graphene sheet, considering a simplified dielectric environment[5]. The data and model show very good agreement. We remark two main features in the experimental and theoretical curves. First, the quenching in the *photon emission* regime does not completely disappear. Second, the fluorescence contrast η depends on E_F in a non-monotonic fashion, and decreases for $E_F > 0.6$ eV.

To better understand the origin of these two features, we concentrate on the theoretical decay rates Γ_{e-g} that correspond to the theoretical fluorescence curve presented in Fig.4.5a. In Fig.4.5b we show them as a function of Fermi energy for a few fixed distances. These traces reveal energy transfer rate increases up to 3000 times for $d = 5$ nm.

The gate-tunability of the emitter-graphene coupling is evident because of the term $\sigma(E_{em}, E_F)$, which makes r_p depend strongly on E_F. The black and violet curves, corresponding to a relatively small $k_{\|}$, have the same shape as the real part of the conductivity, $\mathrm{Re}\sigma(E_{em}, E_F)$, to be compared with Fig.1.4b. This reflects the excitation of electron-hole pairs through vertical transitions, which is suppressed by two orders of magnitude for $E_F > E_{em}/2$.
However, for larger $k_{\|}$, for example as represented by the magenta curve, the suppression is much weaker. In the experiment, these large wave vectors are present due to the very small emitter–graphene distance d. This explains the incomplete recovery of the fluorescence at $E_F > E_{em}/2$ (e.g. in Fig.4.5a).

Indeed, as illustrated in Fig.4.5c in the middle Dirac cone, even though electron-hole pair excitations with small $k_{\|} \approx 0$ (vertical transitions) are inhib-

[5] A rigorous simulation of the complex dielectric environment through a proper multiple-reflection formalism [Blanco & Garcia de Abajo, 2004] leads to very similar results.

ited above $E_F = 0.4$ eV – larger wave vectors still result in electron-hole pair excitations through non-vertical transitions. We note that this near-field effect is markedly different from the not fully understood far-field effect of residual absorption in the Pauli-blocking regime for mid-IR light, which was attributed to a non-zero background conductivity even for large E_F [Li *et al.*, 2008]. In contrast, we can fully ascribe the observations to the incomplete recovery of the fluorescence to e-h pair excitations by higher wave vectors.

Interestingly, upon increase of the Fermi energy above 0.6 eV, both the experimental data and the theoretical model in Fig.4.5a,b show a decrease of emission (stronger quenching) and a reduction in lifetime. We ascribe this effect to energy transfer to near-infrared graphene plasmons. Graphene plasmons emerge at larger E_F because of the suppression of interband transitions and because of the increasing $\mathrm{Im}\sigma(E_{\mathrm{em}}, E_F)$ with E_F (i.e. graphene becomes more metallic).

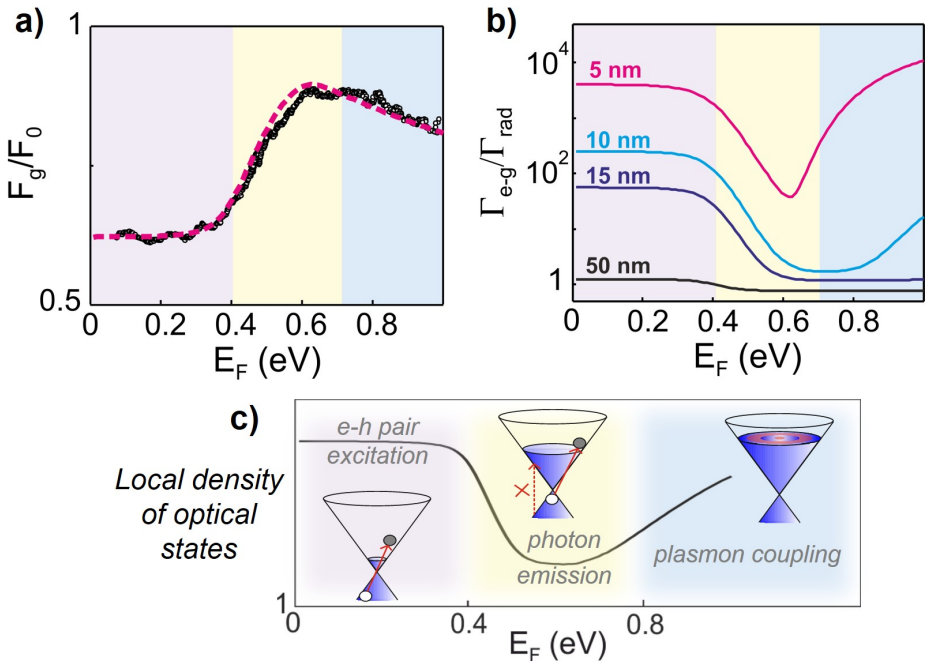

Figure 4.5: a) Fluorescence emission contrast F_g/F_0. Experimental data (black circles) of a device with ∼ 60 nm of Er^{3+}:Y_2O_3 and comparison with theory (magenta dashed line). The parameters for the theory curve are graphene mobility 10000 cm^2 $V^{-1}s^{-1}$, effective dielectric constant $\varepsilon = 3.5$, temperature ϑ=400 K and contribution of emitters integrated between 2 and 50 nm. b) Calculated decay due to emitter-graphene coupling for different emitter-graphene distances, corresponding to the theoretical model in presented in (a) . c) Sketch of the LDOS as a function of Fermi energy and of the processes involved in the emitter-graphene coupling.

4.4 Plasmon coupling

In order to further verify that the experimental observations are signatures of near-infrared graphene plasmons, and to provide more insight on the plasmon field confinement, we take advantage of the fact that the non-radiative emitter–graphene coupling decays with d^{-4} [Gómez-Santos & Stauber, 2011; Velizhanin & Shahbazyan, 2012; Swathi & Sebastian, 2008; Gaudreau *et al.*, 2013], whereas the plasmon-emitters coupling decays exponentially: $e^{-k_\perp d}$ [Nikitin *et al.*, 2011; Koppens *et al.*, 2011; Velizhanin & Shahbazyan, 2012]. We illustrate the emitter-graphene coupling in Fig.4.6a, which shows the numerically calculated electric field patterns for a dipole at different distances from the graphene sheet, showing the coupling to plasmons in the case of 5 nm distance.

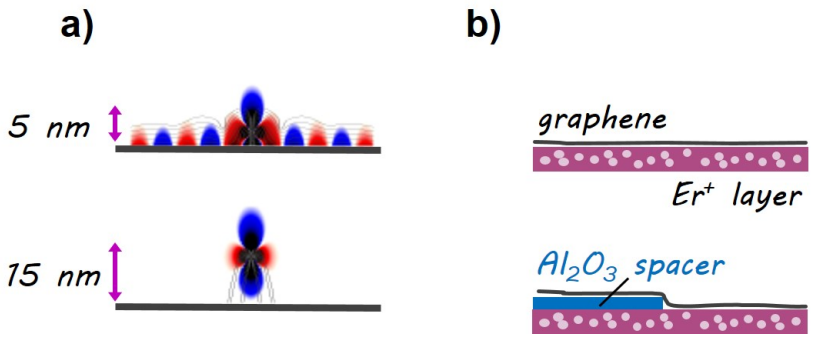

Figure 4.6: a) Electric field amplitude showing the coupling between a dipole and graphene plasmons for emitter-graphene distances of 5 and 15 nm. b) Sketch of the section of the devices used to verify the coupling to near-infrared graphene plasmons.

By controlling the distance between the emitters and graphene, we can tune the relative contribution of the coupling mechanisms (to e-h pairs and to plasmons) and obtain an estimation of the plasmon field confinement. To this end, we use devices with an additional Al_2O_3 spacer layer, grown by atomic layer deposition, in between graphene and the erbium layer. Half of the gra-

phene region is in direct contact with the erbium layer, whereas the other half is separated by the spacer layer, as sketched in Fig.4.6b.

In Fig.4.7a we show the emission as a function of Fermi energy for a region without spacer layer, with a 5 nm spacer layer and a 12 nm spacer layer. For $E_F < E_{\mathrm{em}}/2$ (the *e-h pair excitation* regime) all curves show emission quenching and all curves show the transition to the *photon emission* regime starting at $E_F = 0.4$ eV. The *plasmon coupling* regime is clearly visible for the curve without spacer layer and the one with 5 nm spacer layer. However, for the case of 12 nm spacer layer, the fluorescence curve is independent of E_F for $E_F > 0.6$ eV.

These trends are well reproduced in Fig.4.7b, where we show the calculated emission as a function of Fermi energy. Here we integrate the fluorescence from emitters at distances that range from D to $t+D$, with t the emitter layer thickness. We mention that we do not expect[6] intraband excitations to be responsible for the decrease in emission for $E_F > 0.6$ eV. Indeed the decreasing emission with Fermi energy is well in agreement with coupling to graphene plasmons. With increasing spacer layer the *plasmon coupling* regime starts at a higher Fermi energy. Therefore almost no plasmon coupling is present up to 0.8 eV for the 12 nm spacer layer.

By comparing our data to the model, we can estimate $k_\perp$ of the graphene plasmons and thus the plasmon field confinement with respect to the graphene surface. We find that it is approximately 10 nm, as expected for an emission wavelength of 1.5 μm.

[6] This can be seen from the loss function in Fig. 3.2d of the previous Chapter where it is clear that at distances of only few nanometers the wave vectors overlap with the plasmon resonance, but not with the (much weaker) intraband excitations.

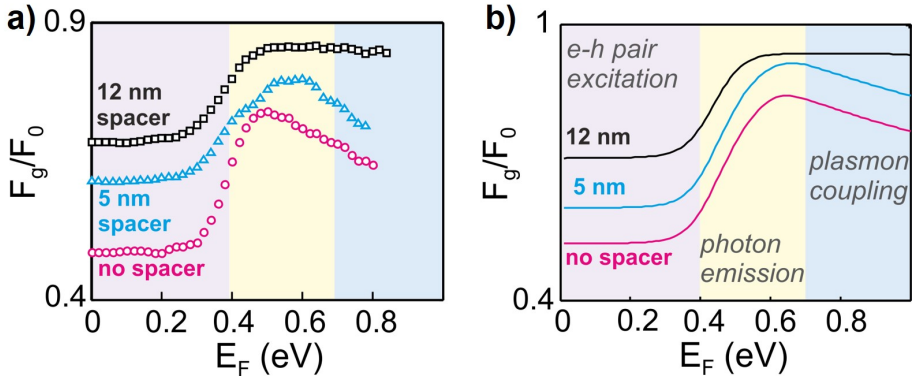

Figure 4.7: a) Experimental fluorescence emission contrast F_g/F_0 for a device with $\sim$ 45 nm of Er^{3+}:Y_2O_3, for no spacer layer (magenta circles), D=5 nm Al_2O_3 spacer (cyan triangles) and D=12 nm Al_2O_3 spacer (black squares). b) Calculated fluorescence contrast as in 4.5a, integrating the contribution of emitters placed at distances between D and $t+D$ from the graphene.

4.5 Conclusions and outlook

In this Chapter we have shown the electrical tunability of the optical emission, relaxation rate and relaxation pathways of an emitter placed in nanometre scale proximity to a graphene sheet. The electrical control is achieved by acting on the graphene Fermi energy, and the emitter-graphene coupling can be tuned through three regimes.

For $E_F < E_{em}/2$, there is energy transfer from the emitter to interband electron-hole (e-h) pair excitations in graphene [Swathi & Sebastian, 2008; Gómez-Santos & Stauber, 2011; Velizhanin & Shahbazyan, 2012]. In the second regime, which crosses over at a Fermi energy of about $E_F = E_{em}/2$, the emitter-graphene coupling is strongly reduced and the graphene is almost "invisible" for the emitter, with most energy of the excited emitter relaxing by photon emission. Interestingly, a third regime at $E_F > 0.7E_{em}$ is accessible, where graphene behaves as a metal and as a result the emitter couples to

intrinsic plasmons, i.e. propagating electron density waves that are strongly confined to the graphene sheet.

The ability to control optical fields by electric fields at length scales of just a few nanometres opens new avenues for on-chip optoelectronic nanotechnologies. Although our devices were suited to show the electrical control of the graphene-emitter coupling, they present some important limitations that hinder their practical use for light control. The two main relevant parameters for devices used for light control, for example as optical modulators, are the modulation efficiency and the modulation speed. In our case, we obtain a modulation efficiency of ∼66% (see Fig 4.5a), which is of little practical use. The modulation speed, on the other hand, was not addressed by our studies. However, the measured decay rates are in the ms range and the observed changes only 2-3 times higher, thus we can infer the limiting speed to be in the kHz range. In addition, another important limitation in this regard is given by the speed of operation of the polymer topgate, which is in the hundreds of Hz range [Ozel *et al.*, 2005].

In order to improve the performances of our devices we therefore should address the aforementioned issues. The main strategies that should be implemented concern the reduction of the emitter intrinsic losses and the realization of even thinner emitter layers with a specific and narrowly distributed distance from the graphene. Improvements in these directions would definitely benefit the modulation efficiency and limiting speed. In addition, would be essential to test different electrolytes or alternative gating methods in order to increase the operation speed.

However we remark that, from a fabrication point of view, the layered device scheme used in these experiments is very flexible to allow changes both in the emitters and in the 2D material that controls the LDOS. Therefore more advanced schemes with emitters at different wavelengths and with nanostructured graphene or more sophisticated 2D material heterostructures could be easily implemented.

5

Real-space imaging and tuning of plasmons

In this Chapter we present scattering type near field scanning microscopy (s-SNOM) measurements that allow a real-space imaging of graphene plasmons launched by the tip. We observe both propagating plasmons and localized resonances, and we show a very strong reduction of the wavelength of the plasmons compared to the free space wavelength (by a factor of 40). We exploit the possibility of tuning the graphene Fermi energy to *in situ* tune the plasmon wavelength and to effectively turn the plasmon resonance on and off.

In the previous Chapter we have seen how it is possible to couple a dipole at a subwavelength distance from a graphene sheet to graphene plasmons, and how this coupling affects the optical emission of the dipole. Several works by other groups have revealed the interaction between low-energy photons and graphene plasmons in the spectral domain. For example, electron spectroscopies (inelastic electron scattering [Liu *et al.*, 2008; Eberlein, 2008; Zhou, 2012] and photoemission spectroscopy [Bostwick *et al.*, 2007]) have been used to spectrally probe broad plasmons in large-area graphene. Resonant coupling of propagating Terahertz waves to plasmons in micro-ribbons has been demonstrated [Ju *et al.*, 2011], and infrared near-field microscopy has been applied to observe the coupling of graphene plasmons to phonons [Fei *et al.*, 2011].

In this Chapter we present the nanoscale real-space imaging of the plasmonic modes, which allows a deeper understanding of propagating and localized plasmons in graphene sheets and nanostructures. We can visualize propagating and localized graphene plasmons in real space by performing scattering-type scanning near-field optical microscopy (s-SNOM) measurements on tapered graphene nanoribbons. In addition, we show the electrical tuning of the observed plasmon features.

5.1 Devices and experimental setup

The devices used for the experiments presented in this Chapter are graphene samples with a triangular shape, where the tip of the triangle is generally tapered down to a width of less than 100 nm. We employ triangular structures, or tapered graphene nanoribbons, because they allow us to probe continuously a variety of ribbons widths.

In order to have devices where we can tune the plasmon wavelength by controlling the Fermi energy, we fabricate graphene FET on SiO_2/Si following the steps described in Chapter 2. To obtain the tapered nanoribbons, we etch a triangular shape out of a larger graphene area made of CVD graphene or on large single or bilayer graphene flakes from mechanical exfoliation, as shown

in Fig. 5.1. The etched triangles have a maximum width of 1 µm and a length of at least 5 µm. They are fabricated using EBL and oxigen plasma etching. We note that we lower the EBL exposure dose towards the ribbon end so that we are able to obtain very narrow widths without suffering too much from proximity effects.

Etching triangular shapes out of a large sheet of CVD graphene provides a mean to access several devices during an experiment within the same sample. In addition, we also fabricated graphene FET out of exfoliated flakes of few layer graphene with naturally tapered tips. Furthermore, naturally tapered ribbons epitaxially grown[1] on the carbon-terminated surface of 6H-SiC have been measured. In those samples the intrinsic high doping and cleanliness due to the lack of fabrication steps allow neat imaging of plasmon interference fringes.

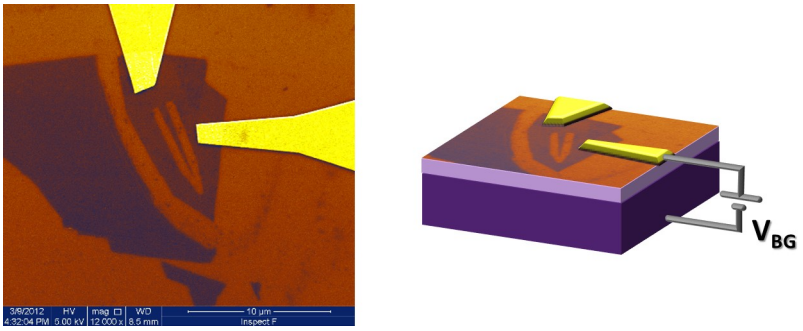

Figure 5.1: SEM false color image of a triangle etched from a graphene flake.

[1] By the GREMAN UMR 7347 group at Université de Tours.

5.2 Scattering-type Scanning Near Field Optical Microscope (s-SNOM)

The nanoscale imaging of the graphene plasmons is performed with a Scattering-type Scanning Near Field Optical Microscope (s-SNOM) from Neaspec GmbH, where infrared light illuminates the AFM tip and the backscattered radiation is recorded simultaneously with the topography. This yields nanoscale resolved infrared near-field images of the amplitude and phase of the scattered field. The measurements where performed within a collaboration with the Nano-Optics group of prof. R. Hillenbrand.

The scattering-type SNOM used for this work employs metal AFM tips as near-field probes, which are illuminated by infrared light from a grating-tunable CO_2 laser. The tip acts as an optical antenna that converts the incident light into a localized near field below the tip apex [Hillenbrand *et al.*, 2002], allowing for deeply sub-wavelength resolution. The nanoscale field concentration provides the required momentum [Novotny & Hecht, 2006; Hecht *et al.*, 1996] for launching plasmons on graphene, as illustrated in Fig. 5.2. The light elastically scattered by the tip back to the detector is recorded with a pseudo-heterodyne interferometer [Ocelic *et al.*, 2006]. In order to suppress background scattering from the tip shaft and the sample, the tip is vibrated vertically with 50 nm amplitude at a frequency of about $\Omega = 300$ kHz, and the detector signal is demodulated at a higher harmonic $n\Omega$. For our experiments we generally look at the 3rd and 4th harmonic of the signal, which give best signal-to-noise ratio.

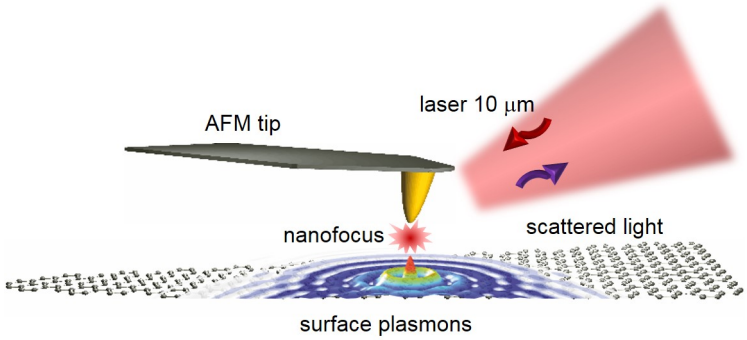

Figure 5.2: Basic mechanism of the plasmon launching and detection with s-SNOM.

5.3 Real space imaging of plasmons

A typical near field image of a graphene triangle on the carbon-terminated face of 6H-SiC is shown in Fig. 5.3, together with a map of the local density of optical states (LDOS) for a graphene device with the same geometry. One of the most distinct features in the experimental near field image is the presence of fringes parallel to the edge of the ribbon at its wider part[2]. We explain these fringes as the interference of forward- and backward-propagating plasmons as follows: the near field at the tip's apex locally excites surface waves that propagate radially along the surface and are reflected back at the graphene edges. These reflected plasmons act back on the tip, and are subsequently scattered into photons, which we detect.

The detected signal is strongly correlated with the vertical component of the LDOS. We can clearly see this from Fig. 5.3, where we compare a topography map (Fig. 5.3a) and the amplitude of the near field optical signal for a graphene ribbon on SiC(Fig. 5.3b) with the calculated LDOS map (Fig. 5.3c).

[2]We note that the much weaker fringes sometimes observed along other directions in these devices, but especially on CVD graphene devices, might be due to plasmon scattering in presence of folds or grain boundaries, as shown by Fei *et al.* [2013].

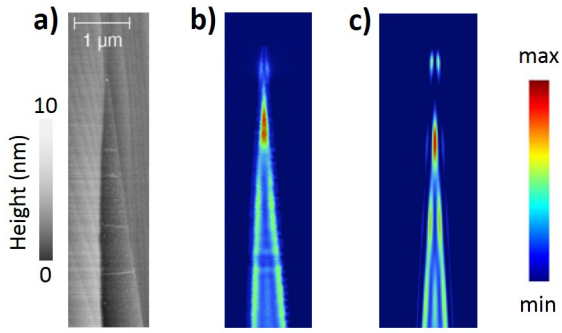

Figure 5.3: a) Topography of a graphene flake on SiC. b) Amplitude of the near field optical signal. c) LDOS map.

The calculated LDOS map for a tapered ribbon matches very closely the experimental results, including the features at the narrower part of the ribbon that we will address in detail later. The LDOS maps are obtained by the group of prof. FJ. Garcia de Abajo [Chen *et al.*, 2012] modelling the microscope tip as a vertically-oriented point dipole [Novotny & Hecht, 2006], which is scanned 60 nm above the graphene. Therefore the LDOS result by solving the Maxwell equations for a dipole source $\mathbf{p}$ at location $\mathbf{r}_0$:

$$\mathrm{LDOS} = \mathrm{LDOS}_{\mathrm{vac}} + \frac{1}{2\pi^2\omega|p|^2}\mathrm{Im}\{\mathbf{E}^{\mathrm{ref}}(\mathbf{r_0})\cdot\mathbf{p}^*\},$$

where $\mathbf{E}^{\mathrm{ref}}(\mathbf{r}_0)$ is the field reflected by nearby structures, which is evaluated at the position of the source dipole.

Propagating plasmons

We now concentrate on the wide part of the ribbon in order to obtain a value for the plasmon wavelength reduction factor, i.e the ratio between the free space wavelength of the photon and the plasmon wavelength. Within this basic physical picture of interference of forward and backward propagating

plasmons launched by the tip, the maxima are separated by half the plasmon wavelength, $\lambda_p/2$. As shown in Fig. 5.4 the distance between fringe maxima is approximately constant at 130 nm inside the ribbon for a free-space excitation wavelength of 9.7 μm. Thus, we experimentally find a plasmon wavelength λ_p= 260 nm, which is about a factor of 40 smaller than the free-space excitation wavelength.

Recalling Eq. 3.3 for the graphene plasmon wavelength, we thus infer a Fermi energy $E_F \approx$0.4 eV, slightly higher than the intrinsic doping levels measured on similar samples via Hall measurements [Crassee, 2011]. This higher doping value could be due to edge doping.

Our experimental observation of an extremely short plasmon wavelength compared to the excitation wavelength is associated with an extraordinary confinement of the infrared field perpendicular to the graphene sheet, characterized by a decay length $\delta \sim \lambda_p/2\pi$. This means that narrow graphene ribbons are ideally suited to confine light down to extremely small volumes.

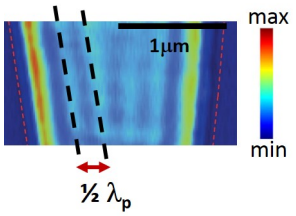

Figure 5.4: Near field optical image upon excitation with λ_0=9,7 μm, from which λ_p=260 nm is extracted. The red dashed line shows the edge of the graphene from the topography.

However, we should notice that for the devices measured in this experiment, we observed complete damping of the plasmon after maximum 5 oscillations, therefore indicating a rather short plasmon propagation length.

Localized plasmons

In Fig. 5.5a, we show a near-field image of the tip of the tapered ribbon where the width W reaches values smaller than the plasmon wavelength λ_p. The two linecuts corresponding to the positions indicated by the red and the green ar-

rows, are shown in Fig. 5.5b. These images clearly reveal two distinct localized modes that coexist with a resonant enhancement of the near-field signal, similar to the observations of Fei *et al.* [2012]. From the width W for which these two modes occur, normalized to the plasmon wavelength λ_p, we experimentally determine the resonance conditions W $0.3\lambda_p$ and $0.6\lambda_p$. In our LDOS

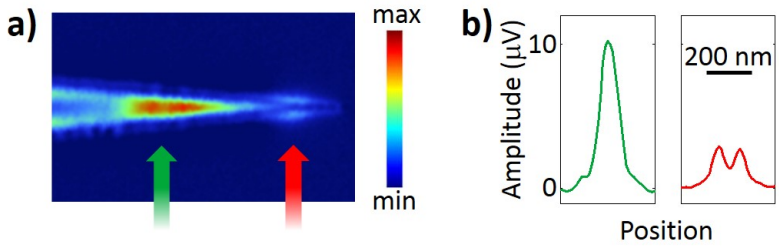

Figure 5.5: a) Near field optical images upon excitation with λ_0=11 μm, for single and bilayer graphene varying the applied gate voltage. b) Linecuts along the lines indicated by the green and red arrows in a).

model interpretation, the localized modes near the tip of the graphene ribbon are explained as localized graphene plasmon resonances, which occur for specific values of the ribbon width (W = $0.37\lambda_p$ and $0.82\lambda_p$) [Christensen *et al.*, 2012], where the strong concentration of the electromagnetic field yields an enhanced plasmon–dipole interaction [Koppens *et al.*, 2011], and therefore, an increase in the near-field signal.

In both theory and experiment, the profiles of the two localized modes are rather different from those of conventional Fabry-Perot cavity modes. For example, the lowest-order mode (indicated by a red arrow in Fig. 5.5a) exhibits field maxima at the graphene edges, while in the conventional lowest-order Fabry-Perot mode the field is maximum in the middle. This is because graphene plasmons are not reflected at the boundaries with a reflection coefficient of minus one (π phase) characteristic of the conventional Fabry-Perot model. Indeed the phase picked up by the plasmon upon reflection at the graphene edge has been calculated to be -3/4π [Nikitin *et al.*, 2014].

5.4 Tuning the plasmons

One of the most appealing advantages of graphene plasmonics is the capability to control and switch nanoscale optical fields *in situ*. Here we demonstrate very effective electrical control of nanoscale optical fields by applying an electric field perpendicular to the graphene sheet. This allows us to tune the plasmon wavelength and even switch the plasmon resonances on and off. To this end, we use the ribbons based on graphene on a SiO_2 substrate with a Si backgate, where applying a backgate voltage V_{BG} we tune the carrier density.

For these devices both the presence of resist residues after fabrication and in the case of CVD grown graphene the intrinsically lower mobility hamper the possibility of extracting the plasmon wavelength from the distance of the fringe maxima parallel to the edges, as they decay too quickly. Therefore we concentrate now on the tip of the triangles and in particular on how the strongest resonance (indicated by the green arrow in Fig. 5.5a) is affected by a change in carrier density. As we have seen in the previous section, the width of the ribbon where the resonance occurs is proportional to the plasmon wavelength. Thus monitoring the position of this resonance along the tapered ribbon is an effective way to qualitatively demonstrate the tuning of the plasmon wavelength.

In Fig. 5.6a we show the optical signal for a single layer graphene device and for a bilayer graphene device for different applied backgate voltages. As it can be seen from the s-SNOM maps, the plasmon wavelength can be significantly modified by applying a backgate voltage. This is even more clear from the plots of the extracted ribbon widths corresponding to the resonances, shown in Fig. 5.6b. In particular, we find that by increasing V_{BG}, the resonances (signal maxima) shift towards larger ribbon width. We attribute this to an increase in plasmon wavelength when the carrier density, and thus also the Fermi energy, increases, in agreement with Eq. 3.3.

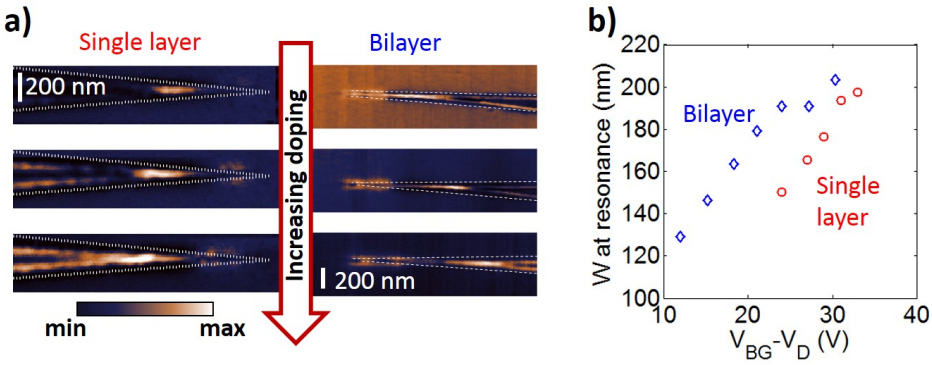

Figure 5.6: a) Near field optical image upon excitation with λ_0=11,06 μm, for a single (left) and bilayer (right) graphene ribbon on SiO_2/Si. The white dashed line show the edge of the graphene from the topography. b) Ribbon width at the resonance as a function of the backgate voltage for the two devices in a).

We note that the position of the charge neutrality point for these measurements can be determined only optically, by looking at the plasmon damping region. This implies an uncertainty on V_D that does not allow direct comparison of the single and bilayer graphene behaviours. However, we point out that single and bilayer graphene are expected to show a different dependence of the plasmon wavelength on backgate voltage, following from the different dependence of the Drude weight on carrier density. In particular, a more detailed study would be interesting for the case of bilayer graphene, since the optical conductivity, although following the Drude behaviour at low frequencies and the interband dominated behaviour at visible frequencies, presents additional features due to phonons at 0.2 eV and interlayer hopping at 0.4 eV [Nicol & Carbotte, 2008].

Finally, we exploit the effect of plasmon damping by interband excitations for small carrier densities ($|E_F| < E_p$), which allow us to actively switch graphene plasmons on and off by electric fields. Experimentally, we clearly observe very strong plasmon damping, as shown in Fig. 5.7, where the ribbon does not show any signal compared to the substrate for negative applied volt-

age. We illustrate electrostatic switching of graphene plasmons in more detail with line scans across a ribbon of width W= 200 nm, while changing V_{BG}. At negative applied voltages, the near-field signal is dramatically depleted on the whole ribbon, while with increasing Fermi energy, plasmon modes emerge.

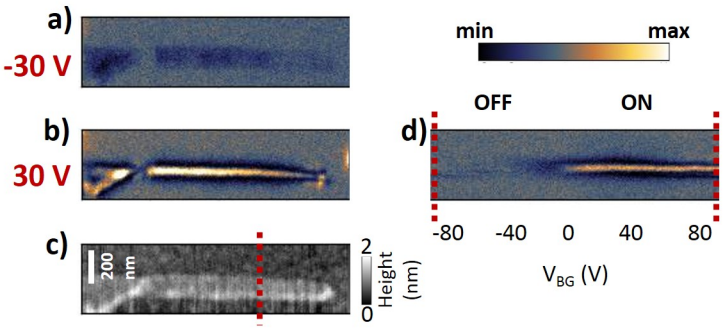

Figure 5.7: Exfoliated natural ribbon on SiO_2/Si. a,b) Near field optical signal for -30 V and 30 V of applied backgate voltage. c)Topography. d) Linecut along the position indicated by the red dashed line in c) as a function of backgate voltage, showing the turning on and off of the plasmon resonance.

5.5 Conclusions and outlook

In this Chapter we have shown the real space launching and imaging of graphene plasmons with s-SNOM. The large wavevector distribution associated with the tip, which can be modelled as a vertically-oriented dipole above the surface, provides the necessary momentum to launch the plasmons. Plasmons are then scattered back by the tip into photons, which are detected.

In this way we can measure the plasmon wavelength, and compare the experimental data to the model presented in Chapter 3. We find a strong reduction of the plasmon wavelength with respect to the free space, by about a factor of 40. Also, by changing the Fermi energy we show that it is possible to effectively tune the plasmon wavelength, and also to turn the plasmons on

and off.

These unique features are the starting points to employ graphene plasmonics in active nanophotonics devices, as envisaged by [Vakil & Engheta, 2011]. However, graphene devices employed in our experiment have relatively low mobility (~ 1000 cm^{2}V^{-1}s^{-1}) and do not show propagation length that would be relevant for applications, as they become completely damped after a maximum of ~ 5 oscillations.

Indeed, more recent studies have already pushed a step further in the development of better quality devices. For example, graphene plasmon focusing has been demonstrated [Alonso-Gonzalez *et al.*, 2014], and higher field confinement and propagation length have been observed in graphene encapsulated in boron nitride [Woessner *et al.*, 2014].

Part II

Graphene-based photodetection

6

Introduction to photodetection with graphene

In this Chapter, the advantages and disadvantages of graphene-based photodetection are presented. We review the most interesting implementations of graphene-based photodetectors in the range from the visible to the MIR and discuss the main strategies to increase the photoresponse of such devices. Also, we discuss the main mechanisms responsible for the conversion of photons to electrical signals, giving particular emphasis to the photothermoelectric effect.

6.1 Why graphene for photodetection?

Technologies involving photon-to-electron conversion are ever more essential in work and leisure activities of the XXI century, from optical communications to imaging for medical purposes. Therefore, a plethora of well-established photodetection schemes exist, mainly based on p-n or p-i-n junctions made of silicon or heterojunctions comprising different types of semiconductors, according to the wavelength range of interest. Still, the need for faster, smaller and cheaper detectors at different wavelengths fuels the effort to continuously explore new materials and solutions.

Advantages

Graphene possesses some very appealing features for photodection applications. First of all the **broadband absorption** allows to span a uniquely large spectral range, from the visible to the Terahertz. **High speed operation** has been demostrated [Xia *et al.*, 2009b; Mueller *et al.*, 2010], and the potential integration of graphene into a fully **flexible** detector design is being investigated [Liu *et al.*, 2014b]. Moreover, the possibility to control the optoelectronic properties by gating leads to an **electrically tunable photoresponse** [Lemme *et al.*, 2011]. Finally, graphene-based detectors operate at **room temperature** and are **compatible with CMOS** technology.

Disadvantages

However, graphene photodetectors, at least in their most simple metal-graphene-metal (MGM) configuration, present some intrinsic limitations which must be overcome in order to increase the responsivity, that is typically $\lesssim 1$ mA/W in the visible and NIR [Lee *et al.*, 2008; Park *et al.*, 2009; Xia *et al.*, 2009a]. Suspended graphene **2.3% absorption**, even if remarkably high for a single layer of atoms, is rather low for photodetection applications. In addition, the **the few picosecond photocarrier lifetime** allows for high speed operation but can

lead to fast recombination [George *et al.*, 2008; Urich *et al.*, 2011] . Furthermore, in MGM devices, as well as in devices based on graphene-bilayer or graphene p-n junctions, the **photoactive area is small**, typically on the order of only few hundreds of nanometres from the metal contacts [Mueller *et al.*, 2009] or the material interface (up to $\sim 1\,\mu m$ for p-n junctions [Gabor *et al.*, 2011]). Finally, the MGM band-structure **symmetry needs to be "broken"** in order to observe a photocurrent signal. For investigation purposes this is achieved by focusing a beam on a much smaller spot than the electrode separation, as for example in the case of the measurements presented in Chapter 8 and 9.

Methods to increase the photoresponse

Several strategies have been undertaken in order to improve the photoresponse of graphene-based photodetectors by tackling the main disadvantages.

Asymmetric metal electrodes. It is possible to break the MGM symmetry by fabricating the electrodes with different metals. In this way a net current is obtained when illuminating the whole device without applying any bias [Mueller *et al.*, 2010].

Increased absorption - intrinsic plasmons. In MGM detectors where the graphene channel consists of 100 nm-wide nanoribbons, MIR light absorption by graphene intrinsic localized plasmons leads to an increase in the photoresponse to light perpendicularly polarized with respect to the ribbon axis [Freitag *et al.*, 2013b].

Increased absorption - field concentration. Up to 60% absorption at a specific wavelength has been achieved placing graphene into an optical cavity [Furchi *et al.*, 2012; Engel *et al.*, 2012]. Another way of increasing the absorption is to exploit the electric field concentration due to metal plasmons (in the VIS) [Echtermeyer, 2011; Liu, 2011] or surface phonons (in the MIR), as explained in detail in Chapter 9. In addition, increased graphene absorption is achieved by coupling graphene to a

silicon wave-guide instead of using vertical illumination [Gan *et al.*, 2013; Pospischil, 2013; Schall *et al.*, 2014].

Different absorbing material - hybrid devices. In this case the material where the absorption takes place and the electrical channel are different, and the absorber can be appropriately chosen according to the desired spectral range. In this way higher photoactive areas can be achieved, and the issue of fast recombination can be overcome. Hybrid devices are particularly promising for high sensitivity applications. For example, devices based on photogating in a hybrid system of graphene and quantum dots [Konstantatos, 2012; Sun, 2012; Klekachev, 2011] will be discussed in more detail in Chapter 7. A similar scheme has been employed in hybrid graphene-MoS_2 detectors [Zhang *et al.*, 2014]. In these devices, the responsivities can reach outstanding values of $\sim 10^7$ A/W, but the spectral bandwidth is limited by the material used as an absorber. In addition, a double-layer graphene heterostructure was reported, where two graphene layers separated by a thin tunnel barrier act as the absorbing layer and as the phototransistor channel respectively. This scheme allowed room- temperature photodetection from the visible to the MIR, with responsivity on the order of ~ 1 A/W in the infrared, on pair with currently used low temperature detectors [Liu *et al.*, 2014a].

Vertical structures. With the ubiquitous use of different 2D crystals such as hBN or transition metal dicalchogenates or transition metal oxides, vertical graphene FET structures have been realized [Britnell, 2012], with promising applications for photodetectors exploiting vertical extraction of the photocurrent generated in the heterostructure [Yu, 2013].

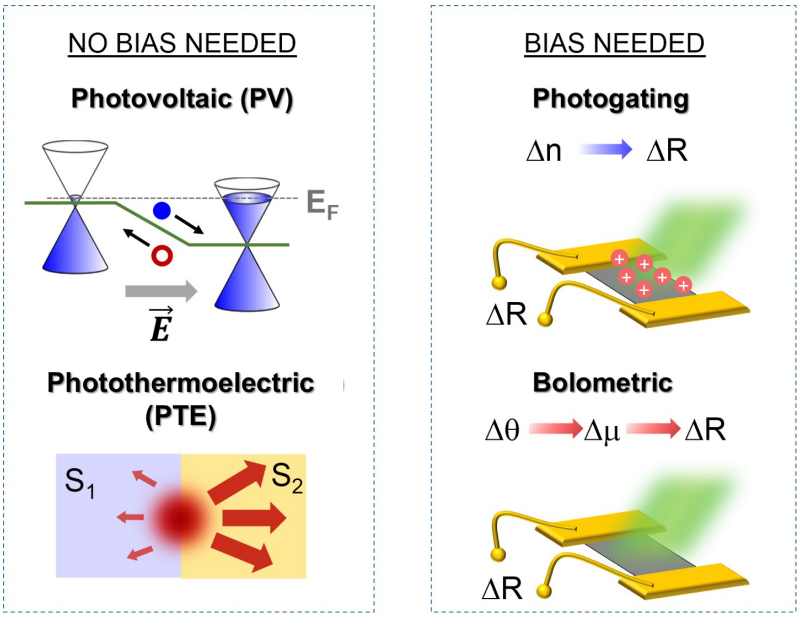

Figure 6.1: Sketch of the main photocurrent generation mechanisms in graphene in the VIS, NIR and MIR spectral range. Left: mechanisms not requiring an applied bias voltage: photovoltaic (PV) and photothermoelectric (PTE). Right: mechanisms requiring an applied bias voltage and relying on a conductance change: photogating and bolometric.

6.2 Photodetection mechanisms in graphene

The main mechanisms that contribute to the conversion of photons to an electrical signal in graphene-based devices are summarized in Fig. 6.1. We divide them for clarity into those that do not require a bias voltage applied, but instead rely on the presence of an interface such as the photovoltaic (PV) and photothermoelectric (PTE) effects, and the ones where photodetection is obtained by monitoring a change in the conductance, such as the photogating and the bolometric effect.

The PV effect takes place in the presence of an electric field that allows charge separation after the creation of an e-h pair by the absorption of a photon. The electric field can be the built-in field resulting at the interface between two differently doped graphene regions, as shown in Fig. 6.1, and indeed PV was described as the main mechanism at graphene metal interfaces in early experiments. Further studies have shown that several features such as response times, wavelength and backgate dependence are instead compatible with a PTE description [Tielrooij *et al.*, 2015a]. The electric field that separates the charges can also be due to an applied bias. In this case, the full graphene area is responsive (even though the responsivity is quite low: 2.5×10^{-4} A/W for red light with 1 V applied bias), with the PV effect being dominant with respect to bolometric effect for graphene close to Dirac point [Freitag *et al.*, 2012]).

Light absorption leads to a temperature increase in the charge carriers, and the hot carrier diffusion from the high temperature region to the low temperature region can lead to a PTE voltage generation, provided that an asymmetry is present in the system, either given by the interface of two materials or by an intrinsic difference between the hot carriers going towards the cold end and the cold carriers moving in the opposite direction, so that the net current flow is non-zero. The PTE effect is then based on the generation of a photovoltage ΔV from a gradient in the charge carrier temperature ϑ, and is governed by the Seebeck coefficient, or thermopower, $S = -\Delta V / \Delta \vartheta$.

In the case of photogating, light induces a change in the carrier density after illumination, leading to a detectable change in the measured resistance. The bolometric effect also results in a change in the device conductivity, which is due to the heat-induced change in the mobility in this case.

6.3 Photothermoelectric effect at graphene interfaces

The electronic contribution[1] to the Seebeck coefficient for metals[2] is described by the Mott formula in the first temperature term of the Sommerfeld expansion (valid for $k_b\vartheta << E_F$) [Ashcroft & Mermin, 1976]:

$$S = -\frac{\pi^2 k_b^2 \vartheta}{3e}\frac{1}{G}\frac{dG}{dE_F} \tag{6.1}$$

where k_b is the Boltzmann constant, ϑ is the temperature and G is the conductance.

In the case of graphene, it has been shown that the value of the thermopower obtained from thermoelectrical measurements matches well with the value that can be retrieved from the Mott formula by differentiating the measured DC conductance with respect to the tunable Fermi level [Zuev *et al.*, 2009; Wei *et al.*, 2009]. Indeed, the Seebeck coefficient of graphene is easily tunable (its typical shape is shown in Fig. 6.2b) and it reaches hundreds of μV/K at room temperature[3].

While a more complete local treatment of the PTE will be given in Chapter 8, we focus here on the conceptually important and simple case of a graphene p-n junction, and the comparison between the expected behaviours due to PV and PTE effects. Tunable graphene p-n junctions can be realized by gating differently two adjacent regions of a graphene flake, for example using split gates at the bottom[4] [Herring *et al.*, 2014], or a top gate and a backgate [Lemme *et al.*, 2011; Gabor *et al.*, 2011]. When sweeping the two gates one can span all the configurations for the junction, as shown in the resistance measurement from Gabor *et al.* [2011] in Fig. 6.2e.

If the dominant mechanism of photovoltage generation was photovoltaic, one would expect only one sign change which occurs when the two regions

[1] Considering independent electrons.

[2] Or semiconductors in the high doping regime.

[3] Note that metals such as Au, Ag and Cu show values of Seebeck of few μV/K, while semiconductors like Si also show several hundreds of μV/K.

[4] Configuration used for some of the measurements reported in Chapter 9.

have the same chemical potential. Indeed, in this case the direction of the built-in electric field changes sign only once, as shown in the sketch of Fig. 6.2a. The measured photocurrent pattern when sweeping both gates would then result in the observation of the p-n quadrant divided in two region with different sign, as shown in Fig. 6.2c from the calculation by Song *et al.* [2011].

Instead, the generation of a PTE photovoltage depends on the difference between the Seebeck coefficient in the two regions, $V_{PTE} = (S_2 - S_1)\Delta\vartheta$. Therefore there are values of the doping (and hence of S_1) in the first region for which the $(S_2 - S_1)$ term changes sign twice while changing the doping of the second region, as sketched in Fig. 6.2b. One sign change occurs again when the chemical potential of the two regions are the same, while the other arises from the non-monotonic behaviour of the Seebeck coefficient. This results in a six fold pattern when both gates are swept, as shown in the calculation from Song *et al.* [2011] in Fig. 6.2d. Indeed, the six fold pattern as shown in Fig. 6.2f was first observed by Gabor *et al.* [2011], proving the fact that PTE is the dominant mechanisms for photocurrent generation in such device configurations.

In addition, the photothermoelectric effect has been shown to be the dominant mechanism giving rise to photocurrent at graphene-bilayer interfaces [Xu *et al.*, 2010], and to describe well experimental findings for graphene-metal interfaces in the VIS, NIR, and MIR [Tielrooij *et al.*, 2015a; Badioli *et al.*, 2014].

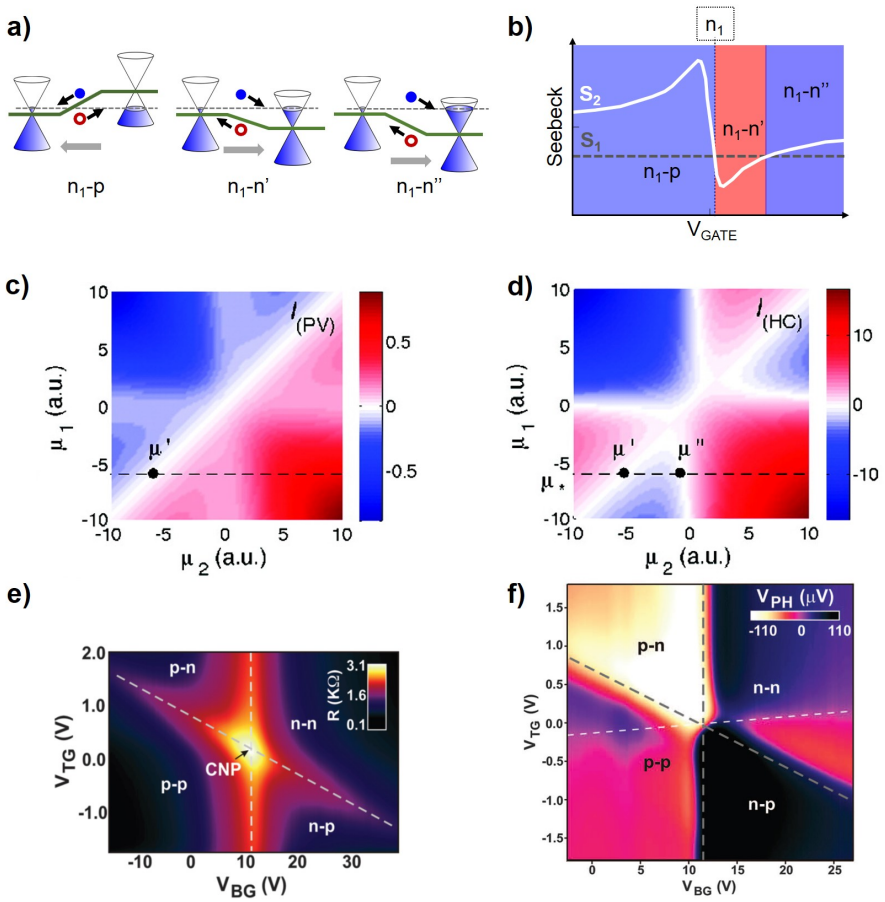

Figure 6.2: Comparison between PV and PTE at a graphene p-n junction. a) Direction of the built-in electric field (that determines the sign of PV contribution to the photovoltage) fixing one side of the junction to a doping n_1, and for three different values of doping of the other side. b) In white: gate-dependent Seebeck coefficient (S_2); grey dashed horizontal line: value of the Seebeck coefficient for the side at doping n_1. The three areas with different colours correspond to the three different junction combinations in a), and the different colours indicate different signs of the resulting photovoltage. c, d) Calculated pattern of the photocurrent when changing the doping level of both sides of the junction for PV (c) and PTE (d), from Song *et al.* [2011]. e,f) Resistance and photovoltage as a function of backgate and topgate voltage for a p-n junction fabricated using hBN as topgate dielectric from Gabor *et al.* [2011]. The photovoltage was measured shining 1 mW of 850 nm light.

7

Hybrid graphene-quantum dot photodetector

In this chapter we show the implementation of a graphene-based ultra-high gain phototransistor. We utilize PbS quantum dots as the absorbing material, combined with graphene as the transport channel, achieving a gain as high as $\sim 10^8$. The gain is gate-tunable by applying an electrostatic gating, and spectral selectivity is obtained by choosing quantum dots with different band-gaps.

7.1 Photodetector gain

As discussed in the previous Chapter, graphene is an interesting material for photodetection [Bonaccorso *et al.*, 2010]. Given its peculiar opto-electronic properties it is suitable to be employed in spectrally broad and fast devices [Xia *et al.*, 2009b; Mueller *et al.*, 2010]. Furthermore, graphene devices are simple to fabricate, they can operate at room temperature and they are compatible with CMOS technology. However, photodetectors made uniquely out of graphene show a small photoactive area and low responsivity, up to ∼10 mA/W for graphene p-n junctions [Lee *et al.*, 2008; Park *et al.*, 2009; Xia *et al.*, 2009a; Lemme *et al.*, 2011; Gabor *et al.*, 2011]. The responsivity can be improved by enhancing the graphene absorption with plasmonic effects or microcavities [Echtermeyer, 2011; Koppens *et al.*, 2011; Furchi *et al.*, 2012; Engel *et al.*, 2012]. However, these solutions do not provide a mechanism to obtain photoconductive gain, that is the generation of multiple charge carriers per incident photon, crucial for highly sensitive photodetection.

Currently, there are different kinds of highly sensitive photodetectors that rely on a gain mechanism, but they generally present some issues difficult to overcome. For example, commercially available avalanche photodiodes and photomultipliers are bulky and operate under high bias. Photodetectors based on epitaxially grown III-V semiconductors can achieve gain of 10^3 [Wright *et al.*, 1980; Leu *et al.*, 1991; Ogura, 2010], but involve technologically challenging and costly fabrication steps and it is not straightforward to integrate them with CMOS technology. Extremely sensitive phototransistors, down to the single photon level, have been demonstrated for visible and NIR light using quantum dots made of epitaxially grown III-V semiconductors for absorption and a 2DEG transport channel [Shields, 2000; Gansen, 2007]. However, in addition to the issues previously described, these photodetectors require cooling to 4K for operation.

A new route to photodetection using a film of colloidal quantum dots has been recently reported by Konstantatos [2006], reaching gain of the order of 10^2-10^3. This approach has the advantage of relying on low-cost fabrication via self-assembly procedures and the possibility of easy integration with CMOS

technology, but the gain value is limited by the mobility of QDs [Konstantatos & Sargent, 2010; Lee *et al.*, 2011].

In the experiments presented in this chapter, high photoconductive gain is obtained by combining the favourable electrical properties of graphene and optical properties of colloidal quantum dots in a hybrid device. As explained in more detail later, the photodetection mechanism is based on light-induced local gating of the graphene that changes the resistance of the transistor channel.

7.2 Hybrid system

In our hybrid graphene-quantum dot phototransitor, graphene is the carrier transport channel, and the quantum dots are employed as the photon absorbing material. The devices consist of a single or bilayer graphene flake coated with colloidal quantum dots (see Fig. 7.1).

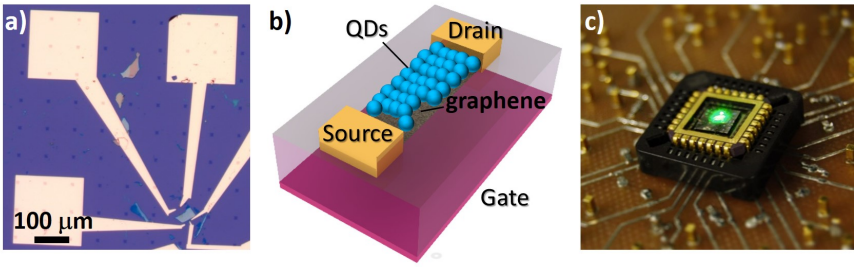

Figure 7.1: a) Exfoliated graphene FET before the QD deposition. b) Sketch of the phototransistor device. The graphene transport channel is covered with a layer of PbS quantum dots, where the light is absorbed. c) Device mounted on the electrical board after the QD deposition. The green laser spot diameter is ~ 3 mm.

The graphene is deposited on a SiO_2/Si substrate and contacted with gold electrodes patterned by EBL, and its Fermi energy can be tuned using the silicon back-gate. After the fabrication of the graphene channel following the

steps described in Chapter 2, a thin film (∼80 nm) of PbS colloidal quantum dots, with exciton peak at ∼950 nm or ∼1450 nm, is deposited via spincasting. The quantum dot charge transfer capability is improved with a ligand exchange process[1] (performed by the Functional Optoelectronic Nanomaterial group at ICFO).

Large photoactive area

In planar graphene photodetectors in the visible and near-infrared, photocurrent generation at zero applied bias takes place in a very limited area in the proximity of an interface, from hundreds of nanometres as reported in [Mueller *et al.*, 2009] to few micrometers as shown by Gabor *et al.* [2011]. The interface can be a graphene/contact boundary, a single-bilayer edge, or a pn-junction. However, for most sensing applications, photoresponsivity over a large area is advantageous. In biased graphene it has been shown that a small photocurrent (with responsivity of 2.5×10^{-4} A/W for 1V of applied bias) can arise from the entire device area due to different mechanisms (photovoltaic or bolometric) depending on the graphene Fermi energy.

We characterize the photoactive area of the hybrid device using a photocurrent map, obtained by scanning our green excitation laser (focal spot diameter ~ 1 μm) over the area of the sample and measuring photocurrent at each excitation spot. As it is shown in Fig. 7.2, our device is strongly photoresponsive over a large area. Indeed, we observe a local responsivity of 4×10^4 A/W for only 10 mV of applied bias.

[1] During the layer-by layer deposition ethanedithiol replaces the ligand on the quantum dot surface in order to turn the quantum dots into a conductive solid state film.

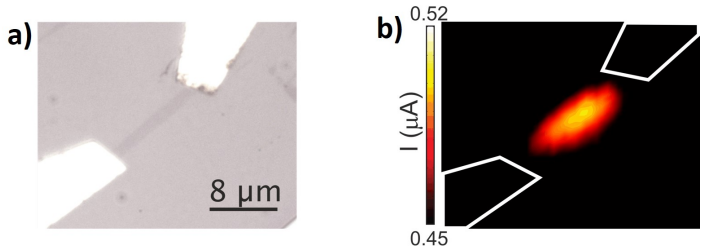

Figure 7.2: a) Optical microscope image of a graphene flake used in the experiments. b) Scanning photocurrent image of the same flake. The photocurrent map is performed upon excitation with a focused laser beam of 1.7 pW of power and 532 nm of wavelength, using 10 mV of source-drain bias.

7.3 Photogating

In order to assess the performance of the device and to reveal the physical mechanism that gives origin to the observed photocurrent response, we study how the source-drain resistance is affected by illumination.
We first measure the transistor resistance as a function of the backgate voltage before the quantum dot deposition, and then after the deposition in the dark and under ambient light, and we show the results for two devices in Fig. 7.3.

The deposition of the QDs has two main effects: the mobility is reduced by about a factor two, and the Dirac peak is shifted. The decrease in mobility is likely due to increased disorder induced by the QDs. The shift of the Dirac peak is due to charge transfer from the quantum dots to the graphene. The direction of the Dirac peak shift depends on the work function of the graphene device before the QDs deposition. The Fermi level of PbS QDs has been found to be 4.7-4.8 eV [Pattantyus-Abraham *et al.*, 2010], while the graphene work function is around 4.6 eV when intrinsic doping is absent [Yu *et al.*, 2009]. As graphene can exhibit some intrinsic doping, QD deposition can induce a shift of V_D to lower or higher backgate voltages.

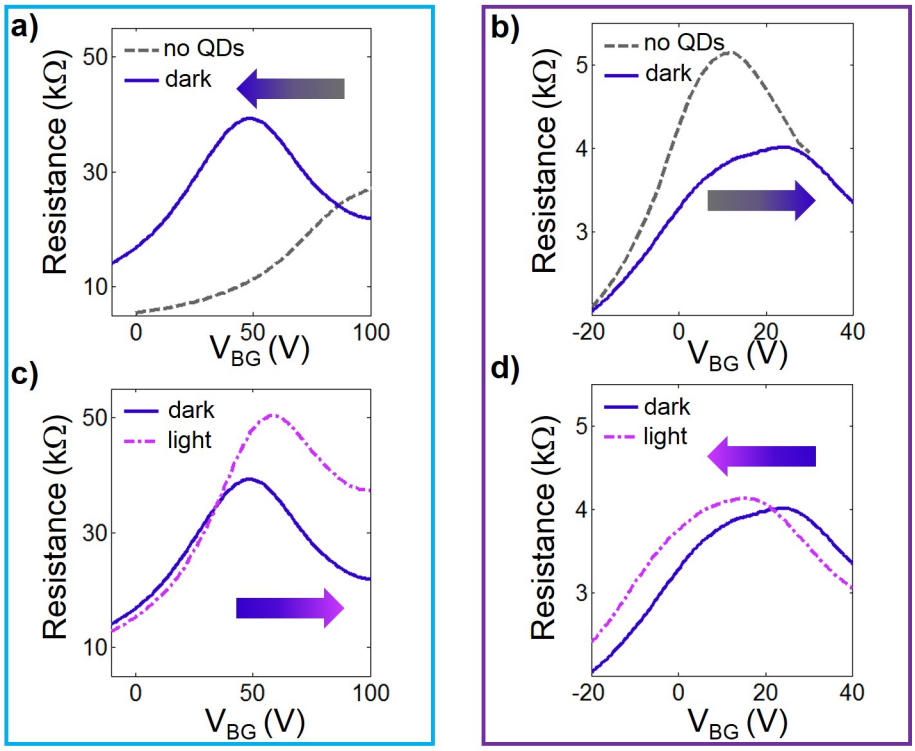

Figure 7.3: Comparison of the resistance as a function of backgate voltage for devices where either holes (left, light blue box) or electrons (right, violet box) are transferred to the graphene upon light excitation. a,b) Before (grey dashed curve) and after (blue curve) QD deposition in the dark. c,d) After QD deposition, in the dark (blue) and with ambient light on (magenta dash-dotted curve).

Here, we present both scenarios

1. For strongly hole-doped graphene, QD deposition induces a shift of V_D to lower backgate voltage, as observed from Fig. 7.3a. This is consistent with a slightly higher work function of the PbS QDs compared to the graphene, which induces electron transfer to the graphene. Under

illumination, V_D shifts back to a higher voltage because holes are transferred (back) to the graphene. This is the case for the device presented in Fig. 7.4 and 7.6.

2. For intrinsically almost undoped graphene, we observed that QD deposition induces a shift of V_D to a higher backgate voltage (see Fig. 7.3b). This is consistent with a slightly higher work function of the PbS QDs compared to the graphene, inducing hole transfer to the graphene. Under illumination, V_D shifts back to a lower voltage because electrons are transferred to the graphene.

We remark that QD deposition reduces the mobility by about a factor two to four, probably due to additional disorder induced by the QDs. In addition, illumination increases slightly the resistance at the Dirac point, possibly due to enhanced disorder originating from light-induced charge carriers in the QDs.

In order to obtain a quantitative analysis of the photodetector behaviour, we then illuminate the device with a collimated laser beam of about 1 mm diameter, and we put the device in vacuum in order to improve the mobility, and reduce intrinsic doping and hysteresis. When the source-drain bias is changed at a fixed backgate voltage, we observe a linear dependence of the photocurrent ΔI, i.e. of the difference between the current measured under illumination and the dark current, on the applied bias.

Setting the source-drain bias to 1 V, we measure the resistance change as a function of the backgate voltage, while illuminating the device. The results of the change of the excitation laser power over a four orders of magnitude range are shown in Fig. 7.4. The power we consider is the one actually impinging on device area, which is estimated from the optical image shown in Fig. 7.1. We observe that illumination causes the Dirac point to shift to higher values of V_{BG}, and thus the resistance of the graphene channel decreases for $V_{BG} < V_D$, where the carrier transport is hole dominated whereas it increases for $V_{BG} > V_D$, where carrier transport is electron dominated. The shift of the Dirac point under illumination indicates that a photo-gating effect is taking place.

The sensitivity of this photogating effect is probed by extracting the val-

ues of the Dirac point change as a function of optical power. We observe a steep linear dependence for low values of the laser power, and a saturating behaviour for higher power. In the region of low laser power we detect a light-induced shift as large as 20 pV/W, as shown in Fig. 7.4c.

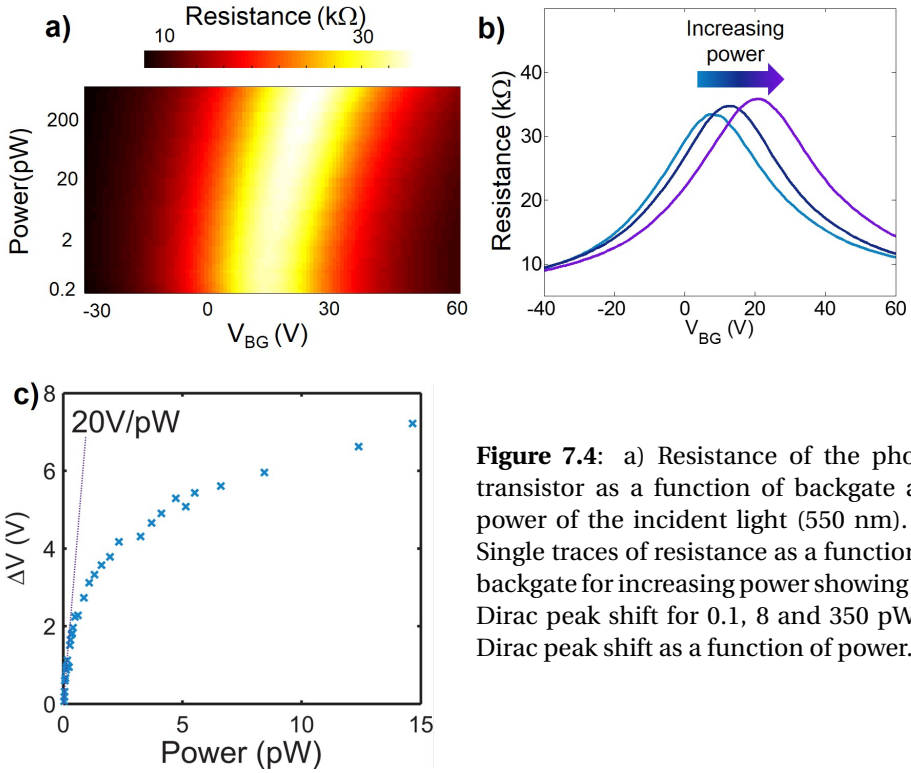

Figure 7.4: a) Resistance of the phototransistor as a function of backgate and power of the incident light (550 nm). b) Single traces of resistance as a function of backgate for increasing power showing the Dirac peak shift for 0.1, 8 and 350 pW. c) Dirac peak shift as a function of power.

Physical mechanism

The observation of the Dirac peak shift upon quantum dot deposition and of the highly sensitive photogating effect leads to the following model of the physical mechanism responsible for the photocurrent generation in our de-

vice. The photons are absorbed in the quantum dot layer, creating electron-hole pairs. The electron-hole pairs separate at the interface between quantum dots and graphene. This is due to the presence of an internal electric field that leads to band bending following the work function mismatch between graphene and the quantum dots. Charge carriers are then transferred from the quantum dots to the graphene, as illustrated in Fig. 7.5. Since we observe that illumination causes a decrease in the resistance when the graphene is hole doped, we infer that the photogenerated carriers that are transferred to the graphene channel are holes. Similarly, we can ascribe the current quenching observed upon illumination for $V_{BG}>V_D$, to the recombination that takes place between photogenerated holes transferred from the quantum dots to graphene and electrons induced by the backgate.

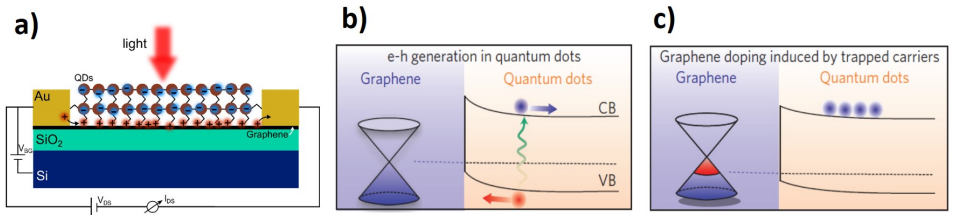

Figure 7.5: Sketch of the physical mechanisms. a) light is absorbed in the QD layer, creating e-h pairs. b) Holes are transferred to the graphene, and c) graphene is gated by the trapped carriers in the QDs.

We apply a source-drain bias, which causes the holes to drift towards the drain. The holes travel through the graphene channel in a typical time-scale of τ_{transit}, which is inversely proportional to the carrier mobility. Electrons remain trapped in the PbS quantum dots with a typical time-scale of τ_{lifetime} due to the built-in field at the quantum dot-graphene interface as well as the electron traps in PbS quantum dots [Konstantatos *et al.*, 2008]. As long as the quantum dots remain negatively charged, positive charges in the graphene sheet are recirculated, due to charge conservation in the graphene channel, as illustrated in Fig. 7.4. Therefore, a single electron-hole pair photogeneration give rise to to multiple holes circulating the graphene channel, leading to

photoconductive gain.

From this simple picture it is clear how key factors for achieving high gain are high mobility of the transistor channel and long lifetimes of the electrons in the quantum dots. Indeed the photoconductive gain for this mechanism can be described as $G = \tau_{\text{lifetime}}/\tau_{\text{transit}}$ [Rose, 1978].

In addition, it allows us to explain the saturation effect with increasing power observed in Fig. 7.4. Indeed, this can be due to the reduction of the built-in electric field at the graphene-quantum dot interface, since an electric field opposite to the equilibrium built-in field arises as the number of photo-generated electrons increases. Also, the progressive occupation of trap states could lead to saturation in the photoresponse.

7.4 Gate-tunable high gain

In this section we analyse the implications of the described phototransistor operation scheme on the device performances. One important figure of merit for photodetectors is the responsivity R=$\Delta I/P$ which is the ratio between the photocurrent to the impinging power. The gain instead, as mentioned before, measures the number of collected electrons per incoming photon, i.e.

$$G = \frac{N_{\text{el}}}{N_{\text{ph}}} = \frac{\frac{\Delta I}{e}}{\phi_{\text{ph}}}$$

where e is the electron charge and ϕ_{ph} is the incoming photon flux, which is given by the ratio of the optical power and the energy of the photon, $\phi_{\text{ph}} = P/E_{\text{ph}}$. This means that gain and responsivity are related by the equation G =RE_{ph}/e.

The highest value for the responsivity achieved with our device in the non-saturation regime is $\sim 5 \times 10^7$ A/W upon excitation with light of wavelength 600 nm (E_{ph}= 2 eV), which thus corresponds to a gain of $\sim 1 \times 10^8$.

Moreover, it is possible to actively modify the responsivity of our device by changing the graphene Fermi energy due to the change in transconductance.

In Fig. 7.6 we show the responsivity as a function of backate voltage: clearly, the responsivity can be tuned and even turned to zero. This feature is useful for applications where the gain has to be adjusted according to the intensity of the light to be detected.

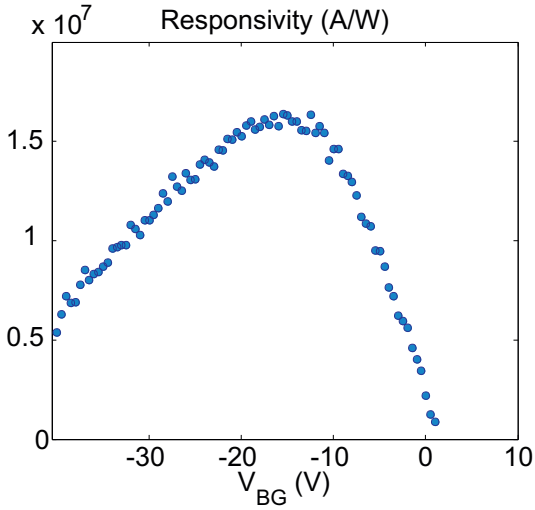

Figure 7.6: Responsivity as a function of backgate voltage.

Temporal response

In the operation of photodetectors with photoconductive gain, the transient response is related to the times it takes for the optical gate to activate, and how long it remains active, allowing for charge carriers to recirculate in the transport channel. As we discussed previously, it is desirable that the photogating stays active much longer than the carriers transit time in the channel to obtain a high gain. However, this occurs at expenses of the time response of the device.

As we show in Fig. 7.7, the rise time of our device's photoresponse is ∼

10 ms, while the decay shows two components [2], one faster, of ∼ 50 ms, and one slower, of ∼ 2s. This time response is not suitable to video-rate imaging applications, hence we propose a scheme to improve it. The decay time can be reduced by lowering the potential barrier at the graphene-quantum dot interface by applying an electrical pulse to the gate so that trapped electrons can be injected in the graphene, thus quickly suppressing the hole-dominated photocurrent.

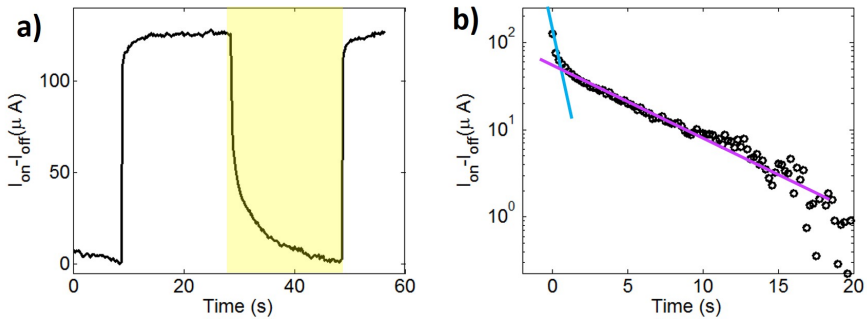

Figure 7.7: a) Time response of a phototransistor (incident power 260 pW). b) zoom of the area highlighted in yellow in a) showing the two components of the decay.

Comparison with model

Starting from the measured time-response of the photosignal, we can compare the experimentally observed gain with the theoretical prediction based on the ratio of the relevant timescales, τ_{lifetime} and τ_{transit}. The transit time of the carriers in the graphene channel is given by:

$$\tau_{\text{transit}} = \frac{L^2}{V_{SD}\mu}$$

[2] The presence of different components in the decay is likely to be originated by the presence of several electron traps associated to distinct surface states of the PbS quantum-dots, as reported in Konstantatos *et al.* [2008].

where L is the channel length, V_{SD} is the applied bias voltage and μ is the carrier mobility. For the device considered here, $\mu \sim 1000\,\mathrm{cm}^2/(\mathrm{Vs})$, $L \sim 10\,\mu\mathrm{m}$, therefore τ_{transit} is $\sim$1 ns. This results in a gain value between 10^7 and 10^9 for τ_{lifetime} of 10 ms and 1 s respectively, in accordance with the value determined by the measurements of the device responsivity. It is then clear that the key requirement for the observed high gain is the fast transit time in the channel. Hence, devices with improved time-response to $\sim$10 ms to achieve video-rate operation either by implementing an electrical reset mechanism, by changing the chemistry of the quantum dots or by choosing a different material for the absorbing layer will still show very high gain. Furthermore, we note that τ_{transit} can be decreased even more by improving the graphene mobility, changing the device geometry or increasing the bias.

7.5 Spectral selectivity

One important characteristic of quantum dots is the size-dependent band-gap, which leads to a size-dependent absorption and emission spectrum. In our photodetection scheme the quantum dots are the light-absorbing material, thus enabling the modification of the optical response of the system by tailoring the properties of the quantum dots. Therefore the fabrication of hybrid devices with quantum dots of different sizes allows tuning of the spectral range of operation of the phototransistors. We demonstrate this feature with the implementation of photodetectors where we use two different batches of quantum dots, one with the exciton peak at $\sim$ 950 nm, and the other with the exciton peak at $\sim$ 1450 nm. In Fig. 7.8 we show the responsivity spectrum for two devices with different quantum dots. As expected, the photoresponse follows the absorption of the quantum dots, and it goes to zero for energies that are below the quantum dot band-gap. This shows how the quantum dot band-gap tunability can be effectively used to achieve spectral selectivity in our phototransistors. In addition, we note that high responsivity is achieved also in the short-wavelength infrared range, where conventional silicon photodetectors are not functional.

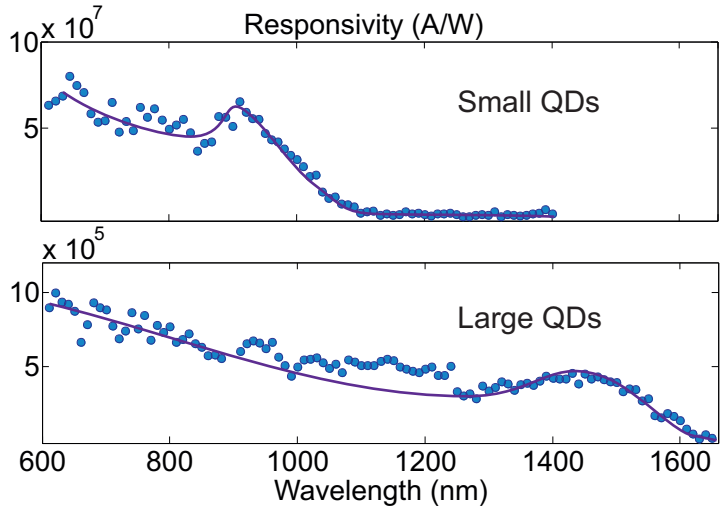

Figure 7.8: Spectral responsivity of phototransistors of single (top), and bi-layer graphene (bottom), with PbS quantum dots of different sizes, with exciton peaks at 950 nm and 1450 nm respectively. The smaller responsivity observed for the bilayer device can be attributed partially to the lower mobility of the sample ($\sim$ 600 cm/Vs), and also to the different work-function of the bilayer graphene which then results in a different band-bending at the interface.

7.6 Conclusions and Outlook

In this chapter we have presented the physical mechanism and the characterization of a hybrid graphene-quantum dot photodetector, realized by coating a graphene FET with a thin film of highly absorbing and spectrally tunable PbS colloidal quantum dots. This photodetector shows high and gate-tunable photoconductive gain, and spectral selectivity in the visible and SWIR range.

This device operates as a phototransistor, a device where a light-activated gate changes the conductivity of the transistor channel. Specifically, the light is absorbed in the quantum dot layer. Photo-generated carriers, whose po-

larity depends on the potential barrier at the interface between graphene and quantum dots, are injected into the graphene and drift towards the electrode due to a voltage bias. The oppositely charged carriers remain trapped in the quantum dots acting as a local gate: the graphene sheet resistance is modified through capacitive coupling.

The high gain exhibited by this phototransistor is due to the high carrier mobility of the graphene sheet and the long lifetime of the carriers that remain trapped in the PbS quantum dots, both of which are crucial factors for an efficient recirculation of charge carriers in the graphene channel while the local gate is active. In addition, the gain can be gate-tuned by tuning the graphene Fermi energy.

The performances of the reported hybrid photodetector can be pushed even further by improving the device fabrication and operation, for example by improving channel mobility to achieve higher gain, or by implementing an electrical reset to obtain a faster photoresponse.

Potentially interesting applications for the proposed phototransistor include night vision cameras, based on the detection of airglow [3] SWIR radiation. Indeed the best options so far for detectors in this spectral range are InGaAs photodetectors [Vollmerhausen *et al.*, 2013], where the hybrid graphene-quantum dot detector could compete both in performances and production costs.

However, in order to work as the building block for video-camera applications, the operation speed characteristics of our devices must be improved to reach a 10 ms video rate in a reliable and practical way. A scheme of high voltage pulses to deplete the electron traps of the quantum dots is an option for research purposes, but for commercial applications a fine tuning of the electron traps controlling the QD growth seems the most viable solution. In addition, further work on the QD chemistry and the choice of a suitable substrate must be done to address device stability and reproducibility over long time scales in ambient conditions.

[3] Airglow is the radiation emitted at night in the high atmosphere due to chemical processes of recombination of molecules that during the day are photoinized by the solar UV light.

Finally, we want to stress that the concept of photogating in graphene can be applied to different purposes. For example, electron injection from plasmonic metal structures has been shown by Fang *et al.* [2012], and a comparable high gain graphene-MoS_2 photodetector based on light absorption in the MoS_2 layer and subsequent graphene photogating has been recently reported by Zhang *et al.* [2014].

8

Mid-infrared photoresponse: the role of substrate absorption

In this Chapter we present a study on graphene photoresponse under MIR excitation. Combining spectrally and spatially resolved photocurrent measurements, as well as transmission measurements, we unveil two origins of the graphene photoresponse in the MIR, one due to absorption in the substrate, and one to direct graphene absorption. We also show how in both cases the photothermoelectric effect gives a good description of our data, provided that different temperature distributions are considered for the two different absorption processes.

8.1 Mid-infrared photonics with graphene

Graphene photonics [Bonaccorso *et al.*, 2010], optoelectronics [Ferrari & Al., 2015; Koppens *et al.*, 2014] and nanophotonics [A. N. Grigorenko , M. Polini, 2012; García de Abajo, 2014; Low & Avouris, 2014] are fast growing fields with increasing attention for the mid-infrared (MIR) regime. This spectral region is interesting both from fundamental and technological points of view. For example, MIR covers the characteristic vibrational frequency range of many relevant molecules, as well as most of the thermal radiation emitted from warm objects. Therefore, the MIR range is crucial for spectroscopy and biosensing, and for thermal imaging in applications ranging from medical diagnostics to damage-assessment, and defence. Graphene is in particular a promising material for detecting MIR light because it provides additional features with respect to current technologies, such as broadband absorption for infrared and visible light, in-situ tunable doping, easy integration with silicon electronics, room temperature operation, and flexibility [Bonaccorso *et al.*, 2010].

In addition, graphene MIR physics is enriched by the fact that the energy scale of the photons is comparable to the Fermi energy, the energy of quasiparticle excitations such as plasmons [A. N. Grigorenko , M. Polini, 2012; García de Abajo, 2014; Low & Avouris, 2014], and the energy of intrinsic and substrate phonons.

Pioneering works have already demonstrated bolometric [Yan *et al.*, 2012; Freitag *et al.*, 2013b] or photoconductive [Yao *et al.*, 2014] MIR detection, and a photo-thermoelectric photoresponse of graphene p-n junctions to 10.6 μm light has been studied [Herring *et al.*, 2014], showing higher responsivity for the appropriate choice of substrate. In nano-patterned graphene, the bolometric photoresponse has been observed to be enhanced by the plasmon-phonon polariton supported by the substrate [Freitag *et al.*, 2014]. Furthermore, photocurrents arising from photo-galvanic and photon drag effects under oblique incidence on large-area epitaxially grown graphene have been reported [Jiang *et al.*, 2011; Olbrich *et al.*, 2013], showing a photoresponse related to the substrate reflection [Olbrich *et al.*, 2013].

8.2 Devices and setup

The experimental results presented in this and the following chapter are based on spatially resolved photocurrent maps. We excite the graphene transistor samples with light from a quantum cascade laser (QCL) from Block Engineering tuned to a specific frequency in the MIR range (1000-1600 cm^{-1}, or ~6-10 μm). We modulate the laser light with a chopper at 423 Hz frequency, in order to perform photocurrent and transmission measurements using lock-in amplification techniques. The scanning photocurrent images are collected by focusing the laser beam with ZnSe lenses to a spot whose fwhm is approximately twice the wavelength, and moving the sample mounted on a motorized stage. The samples consist of CVD graphene deposited onto a SiO_2 (300 nm)/Si or SiO_2 (300 nm)/Si/SiO_2 (300 nm) substrate and etched into rectangles with $\geq$ 100 μm between the Ti (3 nm)/Au (100 nm) electrodes.

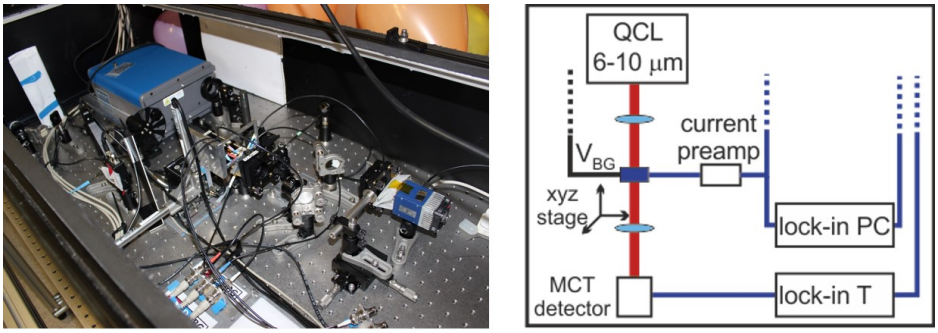

Figure 8.1: Left, picture of the MIR photocurrent setup. Right, sketch of main components of the optics and electronics of the setup.

We record the current that flows between source and drain due to photoexcitation (modulated by the chopper), without applying any bias. The photocurrent is amplified by a Femto DLPCA-200 preamplifier and the lock-in signal is obtained by a Stanford Research Systems SR830 DSP. The transmitted light is re-collimated and collected, thus enabling us to perform simultaneous acquisition of the graphene photoresponse at different wavelengths and

optical transmission.

In order to optimize the transmission of light in the ∼6-10 μm wavelength range, we use double-side polished substrates to reduce scattering from the back surface, and relatively low-doped Si (sheet resistance 5-10 Ω/cm) to reduce the effect of the Drude absorption of the charge carriers in the Si, while still being able to efficiently gate the device. A lock-in amplifier (Femto LIA-MV-150) is used for the transmission measurements.

The experiments are carried out at room temperature in N_2 atmosphere, in order to minimize the effects of the absorption by air in our wavelength range. The output power of the laser varies for each wavelength and is in the mW range. The linear dependence of the photocurrent on incident power is verified acquiring the photocurrent and the transmission signal while changing the power impinging on the sample with the use of two polarisers (one rotating and one fixed) added to the laser beam path.

In this Chapter we concentrate on the results obtained with the light polarization parallel with respect to the contact edge, while in the next Chapter we will discuss the effect of the change of polarization.

8.3 Spatial extent

In Fig. 8.2 we show the spatially resolved photocurrent I_{PC}, normalized by the incoming power P_{inc}, for two excitation wavelengths, $\lambda = 9.26\,\mu m$ and $\lambda = 7.19\,\mu m$, corresponding to $\tilde{\nu}_e$ =1080 cm^{-1} and $\tilde{\nu}_e$ =1390 cm^{-1}, respectively. In both cases, the normalized photocurrent $PC_{norm} = I_{PC}/P_{inc}$ peaks close to the graphene/contact edge, as previously reported for visible and near-infrared light [Lee *et al.*, 2008; Park *et al.*, 2009; Xia *et al.*, 2009a; Mueller *et al.*, 2009]. The position of the contacts is retrieved from the transmission measured at the same time. Interestingly, there is a clear difference in the strength and spatial extent of PC_{norm} for the two frequencies. For $\tilde{\nu}_e$ =1080 cm^{-1}, the normalized photocurrent is high compared to $\tilde{\nu}_e$ =1390 cm^{-1}. Furthermore, for $\tilde{\nu}_e = 1080$ cm^{-1} the system is photo-responsive over a much larger area that extends

even outside the graphene sheet, while the response for $\tilde{\nu}_e = 1390$ cm^{-1} is confined to the interface between graphene and the electrodes. We recall that for excitation with visible and NIR light the photocurrent-active area has been shown to be between hundreds of nanometers [Mueller *et al.*, 2009] and a few microns [Gabor *et al.*, 2011], hence much smaller than the photosensitive area we observe here.

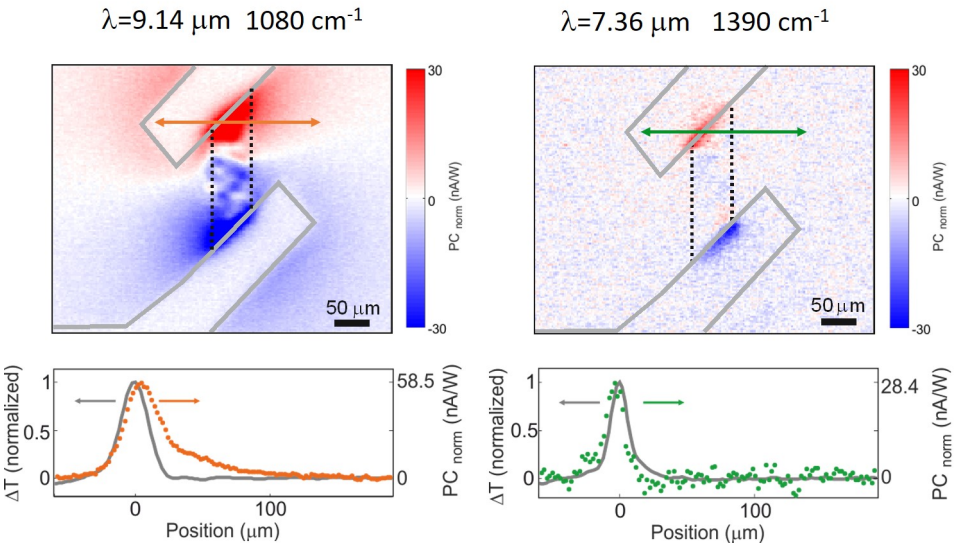

Figure 8.2: Top: photocurrent maps upon excitation with wavelength $\lambda = 9.26$ μm, $\tilde{\nu}_e$=1080 cm^{-1} (left), and $\lambda = 7.19$ μm, $\tilde{\nu}_e$=1390 cm^{-1} (right). The grey lines indicate the position of the contacts retrieved from the transmission measurement; the black dotted lines indicate the graphene position. The beam spot fwhm for the two wavelengths is 22 μm and 14 μm respectively. The photocurrent values are normalized by the incident power. Bottom: (left) In orange, spatial linecut of the photocurrent along the orange arrow in the map at the top left, for 1080 cm^{-1}. (right) In green, spatial linecut of the photocurrent along the green arrow in the map at the top right, for 1390 cm^{-1}. In both cases the grey curves are the normalized spatial derivatives of the corresponding transmission measurement, which indicate the laser spot size.

For a more quantitative comparison, we show at the bottom of Fig. 8.2 a

cut of PC_{norm} across one of the contacts and compare it to the size of the excitation beam, which we obtain from the spatial derivative of the transmitted light. The data show that the photocurrent generated for $\tilde{\nu}_e$ =1390 cm^{-1} is spot-size limited. In contrast, for $\tilde{\nu}_e$ =1080 cm^{-1} the responsive area is significantly larger than the spot-size: ∼20% of the peak signal is still present 50 μm away from the contact edge. In addition, the overall signal at the edge is twice as large as for $\tilde{\nu}_e = 1390$ cm^{-1}.

8.4 Spectrum

The observation of a different spatial extent and signal intensity for excitation with light at $\lambda = 9.26$ μm and $\lambda = 7.19$ μm, suggests the presence of different photocurrent generation mechanisms for the two wavelengths, which we aim to identify by combining spectrally resolved photoresponse and substrate transmission measurements over the ∼6-10 μm wavelength range ($\tilde{\nu}_e$ =1000-1600 cm^{-1}).

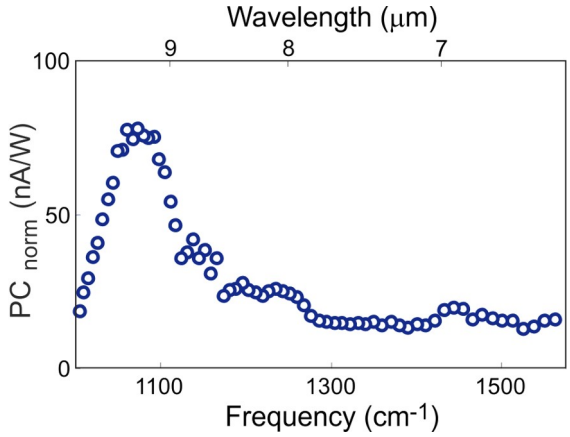

Figure 8.3: Excitation spectrum of the normalized photocurrent, obtained by taking the maximum of PC_{norm}, for a gate voltage that is away from the charge-neutrality point ($V_{BG} - V_D$=70 V)

We obtain the photocurrent excitation spectrum (away from the Dirac point) by recording the photocurrent scanning a line from one electrode to the other in the centre of the device, and selecting the maximum value of the normalized photocurrent. The photocurrent spectrum is shown in Fig. 8.3. We observe a clear peak at $\tilde{\nu}_e = 1080\ \mathrm{cm}^{-1}$, with a shoulder extending up to $\tilde{\nu}_e = 1280\ \mathrm{cm}^{-1}$. In order to understand the presence of such a distinctive peak in the spectrum we proceed to study the optical response of the SiO_2 substrate, that is known to present phonon modes in the 1000-1600 cm^{-1} frequency range.

Optical response of the SiO_2 substrate

We measure the FTIR transmission T of our substrate with an Agilent spectrometer. We observe that the frequency of the photocurrent peak coincides with a peak in the substrate extinction spectrum $1-T$, as shown in Fig. 8.4. Since the spectral features observed in the FTIR spectrum are mainly due to the absorption in the SiO_2 and the reflection at the air-SiO_2 and SiO_2-Si interfaces, this correlation indicates that the interaction with the SiO_2 substrate has a strong effect on the photocurrent[1].

The optical response in the SiO_2 is governed by two bulk optical phonon modes within our frequency window: transverse (TO) and longitudinal (LO) [Ashcroft & Mermin, 1976] and it can be represented by a complex permittivity with the expression derived from Lorentz model for lattice vibrations:

$$\varepsilon(\tilde{\nu}) = \varepsilon_\infty\left(1 + \frac{\tilde{\nu}_{LO}^2 - \tilde{\nu}_{TO}^2}{\tilde{\nu}_{TO}^2 - \tilde{\nu}^2 - i\,\tilde{\nu}\Gamma}\right) \tag{8.1}$$

where ε_∞ is the permittivity at high frequency, $\tilde{\nu}_{LO}$ and $\tilde{\nu}_{TO}$ are the frequencies of the longitudinal and transverse optical phonons respectively, and Γ an effective phonon damping. The real and imaginary parts of $\varepsilon(\tilde{\nu})$ are shown in Fig. 8.4 as obtained from a fit of literature data [Palik, 1997] to Eq. 8.1.

[1] We note that the spectral features observed in the FTIR extinction spectrum are mainly due the SiO_2. Indeed the spectrum of the substrate after an Hf etching to remove the SiO_2 is almost flat and transmits around 90 % of the incident light.

The real part of ε is negative in the frequency range between the TO and the LO modes, the so-called *reststrahlen* band, leading to a strong reflection at the air/SiO_2 interface. For plane wave excitation at normal incidence only the TO mode can directly couple to the incident light. Thus, the imaginary part of ε peaks at the TO phonon frequency, and produces the main contribution to the absorption in the SiO_2 layer. We therefore point out the correlation between the substrate absorption and the photocurrent spectrum, as they both peak at the TO phonon band.

In addition, we note that the imaginary part κ of the refractive index is related to the permittivity with the relation: $\kappa = \sqrt{\frac{\sqrt{(\mathrm{Re}\varepsilon)^2+(\mathrm{Im}\varepsilon)^2}-\mathrm{Re}\varepsilon}{2}}$, therefore no absorption occurs in the substrate for frequencies higher than the LO phonon, where the imaginary part of the permittivity goes to zero.

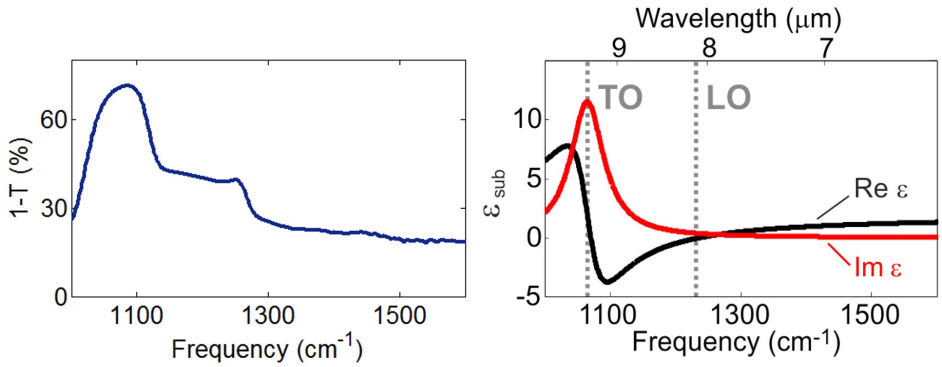

Figure 8.4: Left, extinction spectrum $1-T$ of the substrate, obtained by FTIR. Right, real and imaginary part of the SiO_2 permittivity obtained from a fit of literature data [Palik, 1997] to Eq. 8.1, with $\varepsilon_\infty = 1.843$, $\tilde{\nu}_{LO} = 1243.5\ \mathrm{cm}^{-1}$, $\tilde{\nu}_{TO} = 1065.5\ \mathrm{cm}^{-1}$ and $\Gamma = 61.6\ \mathrm{cm}^{-1}$.

8.5 Photocurrent generation mechanisms

We explain the relationship between the MIR light absorption in the SiO_2 and the photocurrent in the following way: after light absorption, heat is generated in the substrate, where it diffuses and equilibrates with the graphene, which is thus locally heated up (see the sketch in Fig. 8.5a). Consequently, when light is absorbed around the source electrode, an imbalance in the spatial distribution of the temperature of the graphene carriers is created, as graphene close to the drain electrode ($\geq$100 µm away) is not heated. As a consequence of the carrier temperature difference in the source and drain regions, a thermovoltage is generated, mainly governed, as explained more in detail in the last section, by the Seebeck coefficient of graphene: $\Delta V = S(\vartheta_s - \vartheta_d)$, where S is the graphene Seebeck coefficient, and ϑ_s (ϑ_d) is the temperature at the source (drain) contact. The large spatial extent of the photoresponse map as shown in Fig. 8.2 can thus be related to the temperature distribution in the substrate.

We note that this photo-thermoelectric mechanism is markedly different from the reported photo-thermoelectric response for visible and NIR light near metallic contacts [Freitag *et al.*, 2013a] or interfaces, such as p-n junctions [Gabor *et al.*, 2011; Lemme *et al.*, 2011] or single-bilayer graphene [Xu *et al.*, 2010]. In those cases, the graphene carriers are directly excited by the laser and the temperature gradient is generated within or close to the laser spot. In our case, because the region with an elevated substrate temperature extends over a larger area than the spot size, it is possible to observe a photoresponse even when the laser spot is outside the graphene region.

In addition to this spatially extended photoresponse, we also observe a local photoresponse near the contacts, as shown in Fig. 8.2 for $\tilde{\nu}_e$ =1390 cm^{-1}. This local photoresponse is particularly clear for $\tilde{\nu}_e > \tilde{\nu}_{LO}$, where substrate absorption is nearly zero, but a significant photoresponse is still observed (Fig. 8.3). We attribute this local photoresponse to direct light absorption in the graphene, as sketched in Fig. 8.5b.

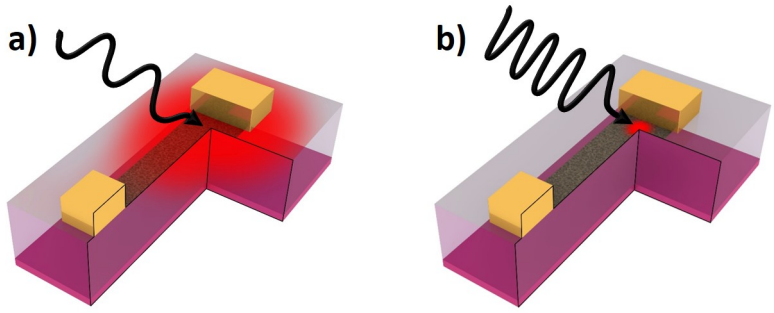

Figure 8.5: The sketches represent artistic views of the two photocurrent generation mechanisms, due to the substrate absorption (left) and the graphene absorption (right).

Interband and intraband effects in the transmission

We verify the occurrence of graphene absorption by directly measuring the light transmission T through the device. In Figures 3a,b we show $1-T$ as a function of the back-gate voltage measured on graphene upon 1080 cm^{-1} and 1390 cm^{-1} excitation, compared with the respective bare substrate extinction. In both cases there is a significant difference between the transmission values inside and outside the graphene over the entire range of applied voltages.

As previously explained in Chapter 1, graphene absorption is due to both interband and intraband processes. In our experiments the photon energy is in the 123-198 meV interval, and thus interband absorption is relevant only for a limited range of Fermi energies ($\sim$ 60-100 meV) around the charge-neutrality point, indicated in Fig. 8.6 with light-blue areas. Outside the interband windows, we clearly observe the signatures of intraband absorption.

We compare the data with the graphene transmission calculated starting from the optical conductivity of graphene at room temperature and taking into account the spatially varying E_F within our focus spot [Martin *et al.*, 2007]. We obtain good agreement with the use of one fitting parameter that represents the fraction of transmitted light through all the other layers of the sub-

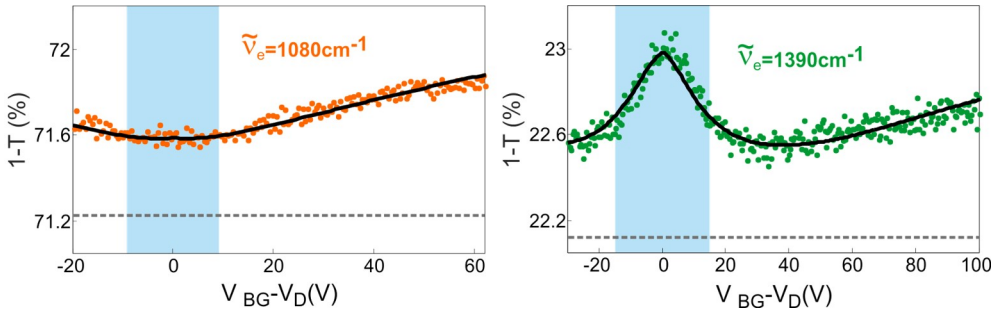

Figure 8.6: Dependence of $1-T$ on gate voltage (where T is the transmission) of the graphene+substrate system (symbols) or of the substrate alone (grey dashed lines), for $\tilde{\nu}$ =1080 cm^{-1} (left), and for $\tilde{\nu}$ =1390 cm^{-1} (right). The black solid curves are obtained from the theoretical model. The light blue areas indicate the regions where interband electron-hole pair transitions are allowed.

strate, following the simple model described below.

In the limit of graphene on an infinite SiO_2 substrate, the transmission defined via the Poynting vector after having passed a distance W is given by

$$T = n|t|^2 e^{-\frac{4\pi\kappa W}{\lambda}}$$

where

$$t = \frac{2}{(1+\sqrt{\varepsilon}+\frac{\sigma}{\varepsilon_0 c})}$$

$\sqrt{\varepsilon} = n + i\kappa$ and λ is the light wavelength. This is an approximation to the full system, where the effect of multiple reflections in the SiO_2 and Si layers is neglected. However, we are interested in a simple model that can describe our data without relying heavily on the material parameters taken from literature, which might be sample dependent. This procedure is further justified by the fact that we concentrate only on the term $|t|^2$ which bears the graphene dependence on E_F. We then compute $|t|^2$ using $\sigma(\tilde{\nu}, E_F) = \sigma_{\text{intra}}(\tilde{\nu}, E_F) + \sigma_{\text{inter}}(\tilde{\nu}, E_F)$, where $\sigma_{\text{intra}}(\tilde{\nu}, E_F)$ and $\sigma_{\text{inter}}(\tilde{\nu}, E_F)$ are obtained from the literature [Falkovsky & Pershoguba, 2007; Falkovsky, 2008; Wunsch *et al.*, 2006; Hwang & Das Sarma, 2007]. We take the scattering time as $\tau = 20$ fs, which

is a realistic scattering time considering that our samples mobility is of the order of 1000 cm^2/Vs. We probe an inhomogeneous sample with a $\sim$10 μm light spot: we include the effect of Fermi energy variation within the spot-size by a conductivity averaged over a distribution of Fermi levels with a standard deviation of 0.12 eV. To explain our data we use :

$$T_{\text{total}}(\tilde{\nu}, E_F) = |t|^2 \cdot T_{\text{sub}}$$

and then obtain T_{sub} by imposing that the value at V_D be the same as the smoothed data.

Our absorption measurements, in combination with the photocurrent measurements, which reveal a response for a wide voltage range (shown in Fig. 8.7, and discussed later), suggest that photoresponse is also originating from direct light absorption in graphene.

Photothermoelectric model for the photocurrent

Finally, we study the effect of the Fermi energy on the photoresponse for the different regimes and explain the results within a simple thermoelectric model. The back-gate dependences of the normalized photoresponse for 1080 cm^{-1} and 1390 cm^{-1} illumination with parallel polarization are shown in Fig. 8.7a. We observe that the photocurrent generated by the 1080 cm^{-1} light (i.e. on resonance with the TO phonon of the substrate) is significantly stronger over the entire applied voltage range and relatively symmetrical with respect to $V_{BG} = V_D$. The photocurrent at frequencies outside the TO phonon resonance exhibits asymmetrical behaviour with respect to V_D: it is strongly negative for $V_{BG} - V_D < 0$, and only weakly positive for higher voltages. We give a qualitative explanation for these different observed behaviours using a single framework based on the thermoelectric effect, where the difference arises due to the spatial extent of the temperature distribution, which is much larger for excitation at 1080 cm^{-1}, compared to excitation at 1390 cm^{-1}. We compute the thermoelectric photocurrent originating from the two different temperature distributions $\vartheta(x)$ at the two different excitation frequencies, by representing

the device by a simple Seebeck coefficient profile, as illustrated in the inset of Fig. 8.7b.

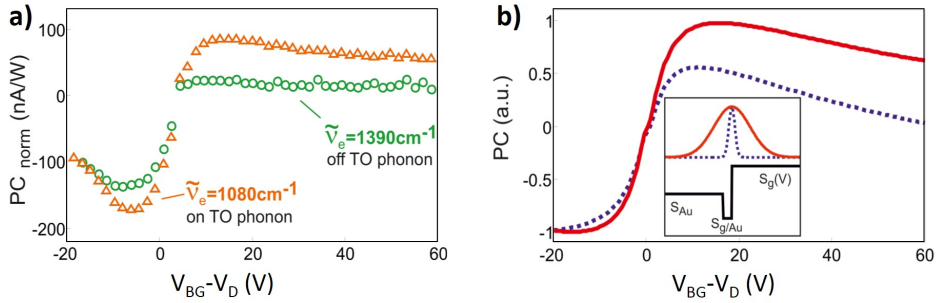

Figure 8.7: Left: photocurrent as a function of back-gate voltage under illumination with $\tilde{\nu}_e$=1080 cm^{-1} light (orange triangles), and $\tilde{\nu}_e$=1390 cm^{-1} light (green circles). Right: calculated photocurrent (normalized to the absolute value of the minimum) obtained from the integration of PC from the equation 8.2, using the $\vartheta(x)$ distributions shown in the inset: red solid curve for the large width one, blue dotted curve for the one comparable to the spot size. The parameters used to estimate the Seebeck coefficient and the resistance are: mobility μ=2000 cm^2/Vs, residual charge density at the Dirac point n$_0$=2·10^{11} cm^{-2}, contact resistance R$_c$=1000 Ω, $S_{g/Au} = S_g(V_{BG} = 1\,V)$

We consider three regions around the gold/graphene contact: the gold, with fixed Seebeck coefficient S_{Au}; the graphene, whose Fermi level is pinned by the gold, with fixed Seebeck coefficient $S_{g/Au}$; and the graphene with gate-tunable Seebeck coefficient $S_g(V_{BG})$ obtained via the Mott formula (see Eq. 6.1 in Chapter 6). In order to simulate the latter, we start from parameters typical for our samples for mobility, residual charge density and contact resistance, and we calculate the conductance from Eq. 2.2, using for the charge carrier density the empirical expression from Meric *et al.* [2008] (Eq. 2.3).

We then recall that the photocurrent is proportional to the spatial integral of the product of the Seebeck coefficient and the temperature gradient,

$$PC \propto \frac{1}{R} \int S(x) \nabla \vartheta(x) dx \tag{8.2}$$

where R is the total circuit resistance, and we describe the two different photocurrent generation mechanisms by means of Gaussian temperature distributions with different widths. We assume that the absorption in the graphene gives rise to a temperature profile whose width is comparable to the laser spot size and to the width of the gold-induced doping region with $S_{g/Au}$. In contrast, the temperature distribution arising from absorption in the substrate can be 5 times larger, following the observations in Fig. 8.2.

As we can see in Fig. 8.7b, where we show the results of the simulations for the set of parameters that best describes our data (see caption), this very simple model captures the main features observed in Fig. 8.7a: the photocurrent resulting from a temperature distribution with a large spatial extent is symmetric with respect to V_D (i.e. the negative and positive responses are comparable in magnitude). Indeed, as mentioned above, this is due to the fact that in this case the main contribution to the back-gate dependence comes from the graphene region in between the contacts, hence it is directly proportional to $S_g(V_{BG})$. Instead, when the temperature distribution width is comparable to or smaller than the the gold-induced doping region, the photocurrent is mainly created at the graphene-graphene junction near the contact, and thus defined by the $S_{g/Au}$ and $S_g(V_{BG})$, which results in a strongly asymmetrical signal. Such photo-thermoelectric response has been reported before for visible light, impinging on graphene pn-junctions [Gabor *et al.*, 2011; Lemme *et al.*, 2011].

8.6 Conclusions and Outlook

In conclusion, we infer the presence of different mechanisms of photocurrent generation in graphene on a polar substrate under excitation with MIR light. One of them is mediated by substrate absorption: the signal peaks at a frequency corresponding to the TO phonon resonance, and shows a spatial extent larger than the beam spot size. The other mechanism is due to hot carrier generation via absorption in graphene, and shows a spot-size limited photoresponse. The back-gate voltage dependence of the photoresponse is

well described with a simple model based on the photo-thermoelectric effect, with different spatial distributions of the temperature profile to take into account the two different mechanisms.

Understanding the role of these photocurrent generation mechanisms paves the way to the possibility of tailoring the magnitude and spatial extent of the graphene photo-response, by employing different substrates, for example by choosing more crystalline materials in order to have stronger phonon effects.

Furthermore, the photocurrent associated to phonon absorption in the substrate should exhibit a slower time response than the photocurrent due to direct absorption in the graphene. It would be particularly interesting to study the time-resolved photocurrent of graphene on SiO_2 membranes, in order to isolate better the interesting physics and prevent the heat conduction through the Si layer that is likely to affect strongly the photothermoelectric response.

9

Mid-infrared photoresponse: the role of surface phonons

In this Chapter we show how the excitation of surface phonons of the substrate leads to an enhancement of the graphene photoresponse. We introduce surface phonons and how to excite them with our experimental system. Then we analyse two examples of sample geometry, the case of a graphene FET on SiO_2 with gold electrodes and the case of a graphene pn junction on local bottom metallic gates. In both cases we show the measured spectra in different configurations and we compare them with simulations of the electric field concentration and the graphene absorption.

9.1 Substrate surface phonons and graphene

Concerning graphene-phonon interactions, extensive studies on scattering of graphene carriers by surface phonons of polar substrates in the context of electron transport properties [Chen *et al.*, 2008; Meric *et al.*, 2008] and relaxation dynamics of hot carriers [Hwang *et al.*, 2013] have been performed. In a related context, electron-phonon scattering at surfaces has been widely studied to understand photoemission spectra [Wang & Mahan, 1972]. For graphene, surface phonons have been found to limit the graphene mobility [Chen *et al.*, 2008; Meric *et al.*, 2008; Fratini & Guinea, 2008], and to provide additional cooling pathways of photoexcited carriers [Freitag *et al.*, 2013a; Low *et al.*, 2012].

In these phenomena, the interaction occurs between electrons and thermally occupied phonon states. In contrast, the use of MIR light can provide an efficient way to excite bulk or surface phonons, which can in turn act back on the graphene charge carriers.

The experiments presented in this Chapter are performed using the same MIR photocurrent setup described in the previous Chapter. In this case, in order to control the excitation of surface phonons, we change the polarization of the laser with respect to the metal edges of the samples.

9.2 Role of edges and light polarization for launching surface phonons

Analogous to surface plasmons in metals, surface phonons are evanescent waves originating from the ionic motion at the surface of polar materials; more precisely, they arise at the interface between two dielectric materials with permittivities of opposite signs, and their in-plane wave-vectors are higher than the free-space wave-vector for light of the same frequency [Kliewer & Fuchs, 1966]. Surface phonons can thus be studied in near-field measurements (see for example Hillenbrand *et al.* [2002]) where the momentum required to excite

the surface phonons is provided by the presence of the sharp metal tip as in the case of the plasmon excitation described in Chapter 5.

In the systems studied here instead, the momentum is provided by the presence of a metallic edge. Indeed, in a simple electrostatic picture, when an electric field impinges perpendicularly on a metal edge, there is an accumulation of charges at the edge, resulting in a strong field perpendicular to the conductor surface. Hence, the near field at the top and bottom corners of the metal contact carries a distribution of large in-plane momenta. The presence of large in-plane momenta thus enables the excitation of the surface phonons when the frequency of the incoming light matches the surface phonon resonance frequency $\tilde{\nu}_{SO}$.

With regards to the experimental implementation of the surface phonon coupling in our system, in Fig. 9.1a we show a sketch of what is meant in this Chapter when we refer to parallel and perpendicular polarization with respect to the metal edge. Measurements in parallel and perpendicular polarization on different samples have been performed often by rotating manually the samples. The results obtained in this way are always consistent but the risk of damaging the samples in the operation is high. In addition, this procedure is quite time-consuming as the focus has to be optimized again each time and the N_2 enclosure has to be opened.

Therefore, for further tests on the polarization on metal-graphene-metal samples we employ a crossed shaped geometry of the sample like the one shown in Fig. 9.1b, or a polarizer. Using a polarizer, one has to be careful in order to be able to compare the signal from the two different polarizations free from artefacts due to the low incident power on the sample for the polarization perpendicular to the laser output polarization. To avoid this problem, we position the sample with a 45° angle with respect to the laser (vertical) polarization, as shown in Fig. 9.1. In this way the parallel and perpendicular polarization with respect to the edge correspond to roughly the same power output from the polarizer.

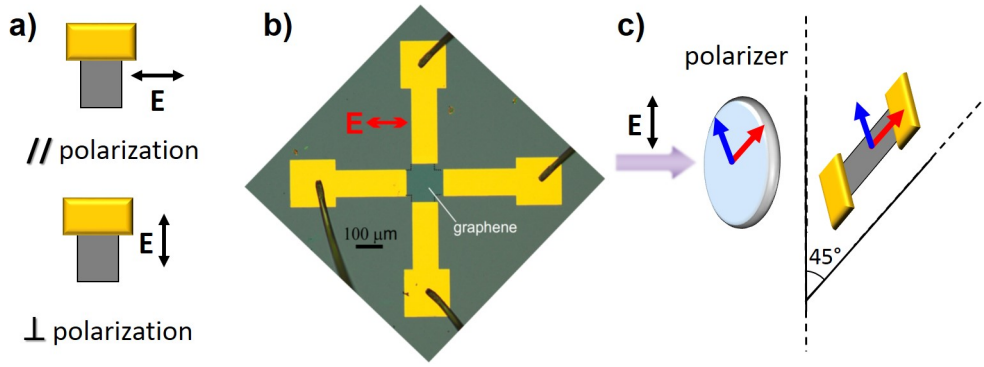

Figure 9.1: a) Sketch of what is meant in this Chapter for parallel and perpendicular polarization. In yellow the metal, in grey the graphene. b) Image of a cross-shaped 4 terminal device where the polarization effect can be tested on neighbouring electrodes. c) Sketch of the sample mounting position when using a polarizer: the sample is mounted with a 45 ° angle with respect to the laser output polarization.

9.3 Surface phonons and photocurrent at the Au/graphene edge

In this section we analyse the same type of metal-graphene-metal detectors on SiO_2 studied in the last Chapter. We measure and compare the photocurrent spectrum in parallel and perpendicular polarization, observing and enhancement of the photocurrent due to the exciation of the substrate surface phonons. We complement our experimental observations with simulations of the electric filed magnitude at the contact edge.

Photocurrent spectrum

In Fig. 9.2a we present the parallel and perpendicular spectra for a cross-shaped 4 terminal device, where we perform measurements for both polarizations without physically rotating neither the light polarization nor the sample.

In order to qualitatively compare the two measurements, that are at different electrodes, we take the photocurrent power normalized and we normalize it by the maximum of the TO phonon related peak, which we expect to be less affected by the direction of the light polarization.

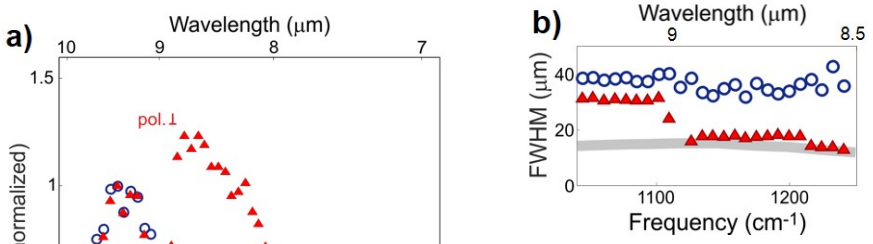

Figure 9.2: a) Photocurrent spectra for perpendicular (red triangles) and parallel (blue circles) polarization for a gate voltage away from the CNP ($V_{BG} - V_D = -90$ V). b) Fwhm of the photocurrent signal. The grey line represents the spot size width as retrieved from the transmission.

Strikingly, the spectrum of the absolute value of the photocurrent $|PC_{norm}|$ for perpendicular polarization presents two peaks: apart from the peak at the TO phonon frequency, there is a second peak at around 1170 cm^{-1}, approximately in the middle of the *reststrahlen* band.

Moreover, the spatial extent of the photocurrent signal is remarkably different for the two peak frequencies, as shown in Fig. 9.2b for the frequency range $\tilde{\nu}_{TO} \lesssim \tilde{\nu}_e \lesssim \tilde{\nu}_{LO}$. For perpendicular polarization, this spatial extent is comparable to the spot size, while for parallel polarization it is more than twice as large as the spot size. This suggests that the strong enhancement of the photoresponse for perpendicular polarization at $\tilde{\nu}_e \approx 1170$ cm^{-1} is due to a local effect.

We note that in the case presented here the two peaks also have different

signs. The reason why the photocurrent direction is opposite in the different spectral regions is not fully understood but we speculate that it is due to changes in the local Seebeck coefficient for different spatial variations of the doping level. We observe in other samples that the presence of a sign change depends strongly on the graphene intrinsic doping and also on the position along the contact.

Field enhancement and absorption

In order to better understand the origin of the second peak in the photocurrent spectrum, we perform simulations of the electric field at the interface between graphene and gold on SiO_2 by numerically solving Maxwell's equations with a finite-difference time-domain method in 2 dimensions (FDTD, using the software Lumerical). In Fig. 9.3a we show a side view of the magnitude of the electric field close to a contact for four different situations: under illumination with light with parallel polarization, with frequency far from (1040 cm^{-1}) and close (1180 cm^{-1}) to $\tilde{\nu}_{SO}$; and under illumination with light with the same two frequencies but polarization perpendicular to the contact edge.

We observe very distinct features in both field magnitude and spatial profile. In the cases where the polarization is parallel to the gold edge, there is no electric field enhancement, as expected, since the only effect of the electric field in this case would be moving charges in the parallel direction. Instead, when the light polarization is perpendicular to the edge, electric field localization occurs at the corners of the contact. When the light frequency is close to $\tilde{\nu}_{SO}$, the excitation of SO phonons results in a strong field enhancement.

The extent of the field enhancement in the graphene plane (for light polarization perpendicular to the contact edge) is presented in Fig. 9.3b for the range of frequencies spanned in the photocurrent spectrum. In turn, this field enhancement leads to an enhancement of the absorption of the incoming light in the graphene sheet near the interface, mediated by the excitation of substrate surface phonons. Indeed, the ratio of the absorption in case of perpendicular and parallel polarization is presented in Fig. 9.3c. We clearly

observe that the graphene absorption is remarkably higher in the frequency range where increased photocurrent is obtained for perpendicular polarization. This observation further supports a scenario in which the graphene absorption in proximity of the graphene/gold interface is strongly enhanced due to the electric field localization produced by the excitation of the SO phonon modes, thus resulting in an increase of the generated photocurrent.

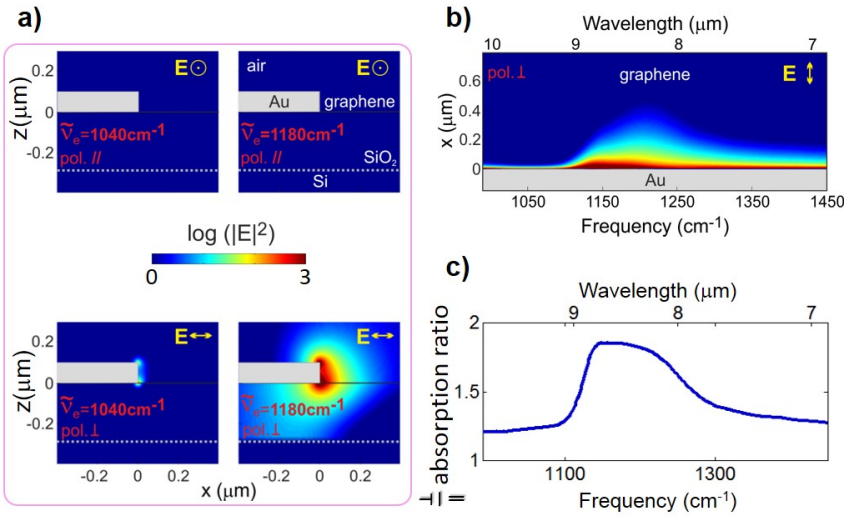

Figure 9.3: a),c) Magnitude of the electric field from FDTD simulations. The device dimensions used are 100 nm thick Au, 300 nm thick SiO_2, and semi-infinite Si. The frequency dependent permittivities of the involved materials are taken from Palik [1997], and in the case of SiO_2 it includes the phonon modes. a) Side view: from top left, clockwise: $\tilde{\nu}_e$=1040 cm^{-1} with parallel polarization; $\tilde{\nu}_e$=1180 cm^{-1} with parallel polarization; $\tilde{\nu}_e$=1180 cm^{-1} with perpendicular polarization; $\tilde{\nu}_e$=1040 cm^{-1} with perpendicular polarization. b) Magnitude of the electric field in the graphene plane from FDTD simulations under illumination with light perpendicular to the contact edge as a function of frequency and distance from the metal edge. Top view of the device. c) Ratio between the absorption obtained from the simulations in perpendicular and parallel polarization.

9.4 Surface phonons and photocurrent at a p-n junction

We now concentrate on a p-n junction device on split metallic gates. The device fabrication was performed at MIT [1] alongside with similar devices used for the measurements presented in Herring *et al.* [2014]. In Fig. 9.4a a lateral and 3D sketch of the device is presented. The p-n junction is created by depositing 30 nm-thick platinum gates separated by few hundreds of nanometres on top of a SiO_2/Si substrate, and then 60 nm of Si_3N_4 as a gate dielectric.

In Fig. 9.4a we present the resistance and photocurrent pattern as a function of the two gates for the device used in the photocurrent. Looking at the resistance, a weaker effect of *gate 2* over *gate 1* is observed in this specific case, and also a presence of gate cross-correlation of unknown origin, differently to the resistance pattern observed in other similar devices. However, this does not affect the results obtained in the following section. Comparing the photocurrent pattern to what we discussed in Chapter 6, we observe that even if the full 6-fold pattern is not present as it would required to span a larger area of the *gate 1*, *gate 2* space, the observed photocurrent pattern suggests a dominant PTE photocurrent contribution, as shown in Herring *et al.* [2014].

In this p-n junction device we focus at the junction and we want to investigate the effect of the light polarization with respect to the metallic gates on the photoresponse. Since the photocurrent signal is rather strong (on the order of 1 nA, as shown in Fig. 9.4c), we can safely use the polarizer scheme presented in Fig. 9.1c without issues due to the power reduction.

As in the case of the previous section, we will first discuss the experimental results on the polarization effect on the photocurrent and then present the results on the electric field simulations.

[1] Not to be confused with MIT, male idiot theory, as reported by Lendrem *et al.* [2014].

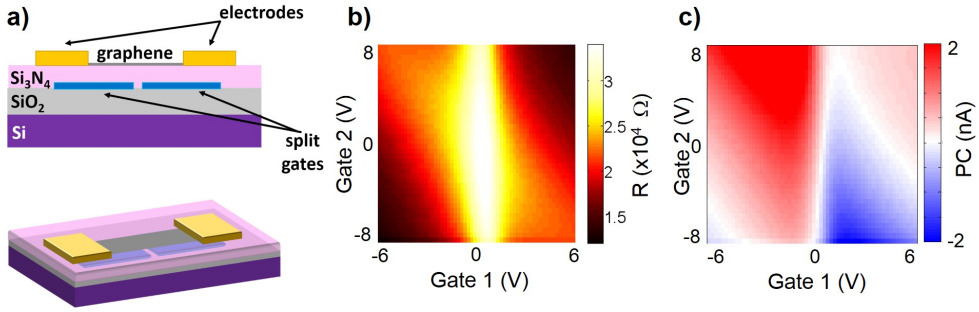

Figure 9.4: a) Sketch of the split gate pn junction device, side and 3D view. b) Resistance pattern as a function of the voltage applied to the two gates. c) Corresponding photocurrent pattern upon illumination with $\tilde{\nu}_e$=1250 cm^{-1}.

Photocurrent spectrum and polarization dependence

In Fig. 9.5a the perpendicular and parallel spectrum of the photocurrent is presented. We observe a remarkably higher photocurrent in perpendicular polarization, that peaks at ∼1220 cm^{-1}. In the inset we show for clarity the same data in logarithmic scale. The two traces differ from almost two orders of magnitude, but we point out that the values of signal revealed in the parallel case are well above the noise floor of our detection setup, and in fact they are actually higher than the standard photocurrent at contacts outside some phonon-enhancement frequency.

This spectrum has been recorded for *gate 1*=-2 V and *gate 2*=0 V, where the photocurrent at the peak is maximum. For different gate values we observe the same shape of the two spectra, but with a slight decrease of the ratio between the peak in the perpendicular polarization spectrum and the parallel photocurrent.

In Fig. 9.5b we show the full polarization dependence for selected frequencies. From the polar plot we observe that there is a strong polarization effect, and that the effect of the polarization is much stronger for $\tilde{\nu}_e$=1210 cm^{-1} and

1230 cm^{-1}.

This results suggest that the origin of the observed peak in the photocurrent is again due to some surface-phonon related electric field enhancement. However, the system of study is now more complex than the case of a metal electrode on SiO_2. Indeed, the Si_3N_4 dielectric has a bulk broad TO phonon peaking at frequencies below the spectral rage of our QCL. It does not support surface phonons as the real part of its dielectric permittivity is always positive in our spectral range. Therefore, as the position of the observed peak in the photocurrent is still compatible with the SiO_2 *reststrahlen* band, we expect an effect of the substrate underneath the gates.

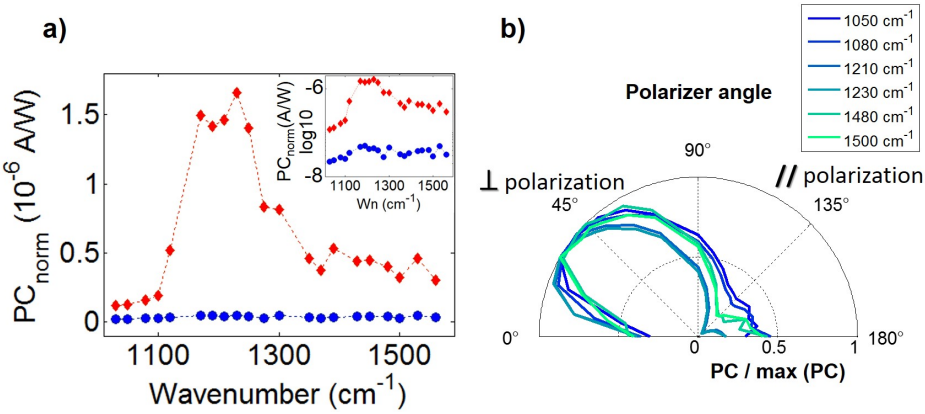

Figure 9.5: a) Photocurrent spectra of the pn junction taken for gate settings: *gate 1*=-2V *gate 2*=0V for parallel (blue dots) and perpendicular (red diamonds). In the inset the same data are plotted in logarithmic scale. b) Polarization dependence for the photocurrent at the pn junction at the same gate position as in a) for selected frequencies.

Field enhancement and absorption

In order to understand the role of the SiO_2 under the platinum gates on the enhancement of the photocurrent in perpendicular polarization, we perform FDTD simulations of the p-n junction device in a similar fashion to the previous section, using 500 nm as the gap between the gates.

The magnitude of the electric field in perpendicular polarization for two different frequencies, $\tilde{\nu}_e$=1210 cm^{-1} and 1010 cm^{-1}, is presented in Fig. 9.6a,b for a side view of the device. We clearly observe a striking difference between the two excitation frequencies. For $\tilde{\nu}_e$=1010 cm^{-1} almost no field enhancement is observed at the edge of the gates. For $\tilde{\nu}_e$=1210 cm^{-1} instead, we see an enhancement of the field, and a bigger hot-spot at the bottom edge of the platinum gate, supporting the fact that the SiO_2 surface phonons play an essential role.

The electric field magnitude in the graphene plane as a function of frequency is presented in Fig. 9.6c, showing the strongest value in the 1100-1330 cm^{-1} region, as in the case of the photocurrent spectrum. Also the absorption ratio of perpendicular an parallel polarization agrees qualitatively very well with the observed spectrum. The presence of two edges close to each other and the additional presence of Si_3N_4 that affects the dielectric environment result in a slightly different and higher ratio than the one observed in Fig. 9.3c for the SiO_2/air case.

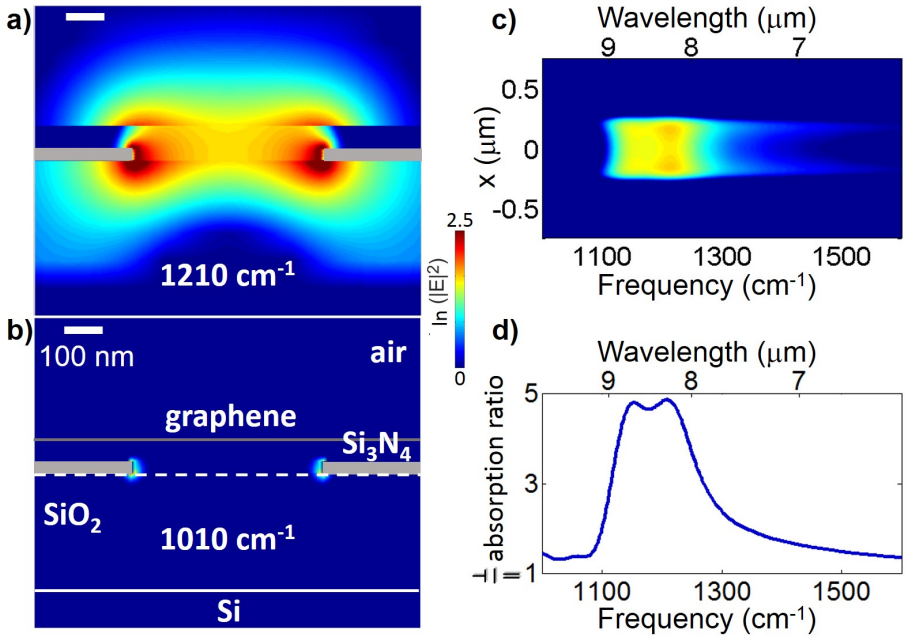

Figure 9.6: a,b) Magnitude of the electric field in the gap between the gates from FDTD simulations with light perpendicular to the gate edge. a,b) Side view. The dimensions used are 30 nm thick Pt, 60 nm thick Si_3N_4 on the Pt gates and 90 nm thick in the gap, 300 nm thick SiO_2, and semi-infinite Si. The frequency dependent permittivities of Si, SiO_2 and Pt are taken from Palik [1997], the one of Si_3N_4 is taken from Kischkat *et al.* [2012]. Top: $\tilde{\nu}_e$=1210 cm^{-1}; bottom $\tilde{\nu}_e$=1010 cm^{-1}. c) Magnitude of the electric field in the graphene plane from FDTD simulations under illumination with light perpendicular to the gate edge as a function of frequency. Top view of the device. d) Ratio between the absorption obtained from the simulations in perpendicular and parallel polarization.

9.5 Conclusions and outlook

In this Chapter we have presented a study of the graphene MIR photocurrent as a function of light polarization with respect to the metal edges present in the sample geometry. We found a strong increase of the photocurrent in the region of the substrate SO phonon frequency range when the light impinges on the metal edges with perpendicular polarization. FDTD simulations of the electric field magnitude and the graphene absorption confirm this trend. Therefore our results show how the electric field concentration due to the excitation of surface phonons of the substrate can enhance the graphene photoresponse, both in the case of a simple graphene FET and in the case of a graphene pn junction with split metallic gates.

However, even in the pn junction case, the responsivity of the devices is still far from being appealing for commercial applications. Further studies could be performed to better understand the SO phonon-graphene interaction and to open the route for an enhancement of the efficiency. For example, even if the simulations show an increase of the graphene absorption in qualitative agreement with the measured spectra, other mechanisms, such as local heating, could also play a major role.

In the case of a split gate pn junction two straightforward steps could be taken to boost the effect of the SO phonon enhancement. Firstly, relying directly on the local gate dielectric surface phonons (instead of relying on the field enhancement due to the SiO_2 substrate SO phonons as in the device presented here) would bring a considerable advantage. Also, the thinner the gate dielectric the higher would be the influence of the field enhancement at the metallic gate edge on the the graphene photoresponse. In this regard, split gate pn junctions using h-BN as the gate dielectric would be interesting systems to study. In addition, reducing the gate thickness might bring further confinement via the coupling of the hot spots at the bottom and top edge. In this respect, a pn junction using graphene as a gate would be interesting to test.

Finally, as we mentioned earlier, a way to excite surface phonons is via a

AFM tip illuminated with light matching the surface phonon resonance. Therefore, particularly important would be a near-field photocurrent study[2] on a graphene device on a substrate that has interesting and strong phonon polariton modes; for example, the choice could fall on SiC, highly crystalline substrate whose surface phonons have been studied by s-SNOM experiments [Hillenbrand *et al.*, 2002]; or h-BN, whose near-field properties have been shown to be tunable with the number of layers [Dai *et al.*, 2014]

[2] similar to the experiment presented by [Mueller *et al.*, 2009] for the visible.

Conclusions

Optoelectronics deals with the control of optical fields through electric fields, as well as with the light-induced change of electrical quantities. Taking advantage of some of the unique properties of graphene, such as the two dimensionality, the broadband absorption and the electrical tunability of the optical and electrical properties, we demonstrated devices where light is controlled, confined and detected.

In the first part of the thesis we concentrated on the electrical control and confinement of light, presenting two experiments in the field of graphene nanophotonics and plasmonics. In the second part, we focussed on light detection, presenting three mechanisms where graphene photoresponse can be enhanced thanks to the interaction with surrounding materials.

Graphene nanophotonics and plasmonics

In this part of the thesis, we exploited the tunability of the optoelectronic properties of graphene to show how it is possible to modify the environment, i.e. the optical density of states, of a dipole placed at a subwavelength distance to a graphene sheet by acting on the graphene Fermi energy.

In the first experiment presented, the dipoles consist of erbium ions embedded in a thin ($\lesssim$60 nm) oxide matrix, where graphene is deposited. The fluorescence emission at 1.5 μm is probed while the graphene Fermi energy is increased up to 1 eV via electrolyte top-gating. Our results demonstrate the graphene-mediated electrical control over the relaxation pathways of the op-

tical emitters placed in close proximity to graphene. Since graphene can behave as a semiconductor, a dielectric (when vertical interband transitions are inhibited due to Pauli blocking) and a metal, the optical flow from the emitters can be tuned through three regimes. In the first regime, for very low graphene doping, the emitters relax through the excitation of electron-hole pairs in graphene. In the second regime, the main relaxation pathway is the emission of photons. Finally in the third regime the emitter relaxation occurs via the excitation of graphene plasmons, which are shown to be very tightly confined ($\sim$10 nm) to the graphene plane.

In the second experiment, the metallized tip of an AFM operated in tapping mode and illuminated with mid-infrared light acts as a vertically oriented dipole. The tip is scanned over graphene tapered nanoribbons and launches graphene plasmons, provided that the graphene Fermi energy is sufficiently high ($E_F \gtrsim E_{\mathrm{ph}}$). The scattered light is detected, producing a map of the charge density waves along the surface, closely related to the local density of optical states. In this way it is possible to directly visualize plasmons in real space, and therefore measure the plasmon wavelength. We find, as expected, a very strong reduction of the plasmon wavelength with respect to the free space wavelength (by a factor of $\sim$40), indicating an equally strong vertical field confinement of the plasmon field. By tuning the graphene Fermi energy the plasmon properties, such as the wavelength, can be modified, and the plasmon resonance can be turned off by reaching the interband damping regime.

Discussion and outlook

These experiments open new routes in the field of light control and localization, and we envisage potential applications in the fields of active nanophotonics and sensing. The two main features present in both experiments are the on/off control of light with electric fields and the strong electric field confinement due to the graphene plasmons.

On/off control of light:

Electrical control of erbium emission Optical switches activated by electric gates are a natural perspective for the demonstrated electrical control of the emission of erbium. As the emission occurs at 1.5 μm, if implemented, such devices would have an impact on optical communications. However, as mentioned in Chapter 4, the modulation efficiency (∼66%) and speed (limited to hundreds of Hz by the topgate operation) are far from being useful. To improve these two parameters, efforts should be made in order to:

- reduce intrinsic losses;
- fabricate a thinner emitter layer;
- obtain a lower spread in the vertical distribution of the emitters;
- identify a high speed operation gating system allowing similar values of doping (i.e. at least 0.5 eV).

Mid-infrared tunable plasmons On/off control of plasmons via electric fields as shown in Chapter 5 could be the starting point for the development of active plasmonic devices, towards the miniaturization of photonics circuits. In this regard, a setback could be the small plasmon propagation length in the devices that we analysed, but more recent experiments on high quality hBN–graphene–hBN stack already showed more than five times higher figures of merit [Woessner *et al.*, 2014].

Strong field confinement: both in the near-infrared and in the mid-infrared we get an estimation of the vertical extension of the plasmon electric field, showing very high confinement to the surface.

NIR plasmons In the case of the near-infrared fluorescence probe, we tune the emitter-plasmon coupling by controlling the distance between the graphene and the emitter layer, showing a vertical confinement $\delta \sim 10$ nm. However, future studies should address a deeper investigation of the properties of near-infrared plasmon, especially for what concerns their lifetime and propagation.

MIR plasmons In the case of the mid-infrared s-SNOM experiment, we evaluate the vertical confinement $\delta \approx \lambda_p/2\pi$, from the direct measurement of the plasmon wavelength λ_p ~200 nm. The very high field confinement and the tunability of the plasmon wavelength in the mid-infrared have a very straightforward application in the field of bio-sensing. Indeed, high sensitivity mid-infrared plasmon enhanced spectroscopy has just recently been demonstrated by Rodrigo *et al.* [2015] down to the single monolayer of proteins.

Graphene-based photodetection

In this part of the thesis, we studied the use of graphene as a photodetector. As graphene is atomically thin, some of its properties can be greatly influenced by its environment. In particular, we analysed how the optical excitation of either QDs deposited on top, or the bulk or surface phonons of the substrate can lead, with different mechanisms and to different extents, to an increase of the graphene photoresponse.

The first implementation presented is a hybrid graphene-quantum dot phototransistor in the visible and near-infrared. When light is absorbed in the quantum dots holes are injected into graphene, and electrons remain trapped in the QDs for a characteristic time, during which the positive charges recirculate into the biased graphene channel. Thanks to the high mobility of graphene, carriers can circulate many times while the electrons are trapped, giving rise to gain, i.e. a higher number of generated electrons with respect to the incoming photons.

Concerning the graphene photoresponse in the mid-infrared instead, we showed how the photocurrent is generated via photothermoelectric effect after light absorption by the bulk phonons of the substrate. This results in a remarkably stronger photocurrent with respect to the photocurrent due to direct light absorption in graphene, as clearly seen in the photocurrent spectrum. Also, the spatial origin of the photocurrent generation is not restricted to the narrow region at the interface between graphene and metal contacts,

but it extends tenths of micrometres away.

Finally we saw how surface phonons of the substrate, excited by means of illumination perpendicular to a metal edge, also leads to a strong increase in the photocurrent, following a strong increase in the local electric field at the graphene position. This occurs both at the metal graphene interface in metal-graphene-metal devices and at p-n junctions fabricated using metallic split gates, where the effect is even stronger due to the presence of the gap between the two gates.

Discussion and outlook

The proposed schemes to enhance the photoresponse of graphene have very different technological perspectives given the considerably different mechanisms, spectral operation ranges, and detector responsivities. For a general comparison to our devices, commercial InGaAs detectors in the NIR have ∼1 A/W responsivity and cut-off frequencies in the MHz range.

Visible and NIR hybrid detector For the hybrid graphene-QD photodetector, the intrinsic responsivity of $\sim 10^7$ puts our detector in the high sensitivity range. This result is promising for practical applications. Indeed, a team at ICFO has been working in close contact with industries on the development of prototypes, such as cameras in the short-wavelength near infrared. The main improvements required starting from the device implementation presented in this thesis should address the the speeding up of temporal response at least to 100 Hz for video-rate operation (with changes in the QD properties to have shorter-lived electron traps) and the stability of graphene and QDs over time (with appropriate choice of substrate or encapsulation). As mentioned in Chapter 7, there is a trade-off between operation speed and gain. However, given the very high responsivity of our devices, even reducing the electron traps lifetime from ∼1 s to ∼ 1 ms could still allow to realize competitive detectors.

MIR photoresponse Concerning the photoresponse in the mid-infrared, our results open the way to more fundamental questions, for example on the different timescales of the photocurrent generation mechanisms, and on the interaction with different or more crystalline substrates. The detectors presented show low extrinsic responsivities, on the order of $\sim 10^{-8}$A/W for the TO enhanced photocurrent at a contact and $\sim 10^{-6}$A/W for the SO phonon enhanced p-n junction. Even considering that the active area may be smaller than the laser spot size, these values are not suitable for light detection applications competing with available technology. However, since we showed that graphene, via photothermoelectric effect, is sensible to the absorption of its surroundings, one could envisage biosensing applications for electrically read-out local spectroscopy.

A
Fabrication recipes

Here we report the recipes mostly used during the sample fabrication. Part of these recipes have been initially developed by different groups at ICFO[1] and other research centres[2]. They have been tested and optimized them for the specific devices needed for this thesis.

EBL

Sample preparation - etching

1. Spin coat the clean sample with PMMA 950k (concentration 2.5%). Step 1: 3000 rpm for 5s, step 2: 6000 rpm for 30s (ramp time 3.5 s).

[1] Dr. Johann Osmond from the NPL team helped with the EBL, Dr. Davide Janner from the Optoelectronics group for the UV lithography.

[2] MIT for the thermal annealing and Columbia for the polymer electrolyte

2. Bake at 160°C (5 min on the hotplate or 1h in the oven).

In order to achieve better resolution it is possible to reduce the layer thickness by diluting the PMMA with the appropriate solvent (chlorobenzene (toxic), anisole or ethyl lactate).

Sample preparation - electrodes (PMMA as sacrificial layer)

1. Spin coat the clean sample with PMMA 200k (concentration 3.5%). Step 1: 3000 rpm for 5s, step 2: 6000 rpm for 30s (ramp time 3.5 s).
2. Bake at 160°C (5 min on the hotplate or 1h in the oven).
3. Spin coat with PMMA 950k (concentration 1.5%). Step 1: 3000 rpm for 5s, step 2: 6000 rpm for 30s (ramp time 3.5 s).
4. Bake at 160°C (5 min on the hotplate or 1h in the oven).

The two different layers result in undercut that facilitates the lift-off.

Exposure-standard doped Si substrate[3]

- Micrometer and sub-micrometre areas: tension 30kV, current $\sim$ 0.045 nA (aperture size 2 on the Raith systems used), step size 10 nm or smaller, write field 100 μm or smaller, dose: 330 μC/cm^2.
- Tens or hundreds of micrometre areas: tension 30kV, current $\sim$ 3.3 nA (aperture size 6 on the Raith systems used), step size 100 nm, write field 1000 μm or smaller, dose: 330 μC/cm^2.

The dwell time t_D is obtained from: $t_D = \frac{dose*s^2}{I_{beam}}$ where s is the step size and I_{beam} is the beam current. Always check that the writing speed $v = t_D/s$ is not too high (4 mm/s is the optimum). Settling time 1ms or more.

Exposure-$LiNbO_3$[4] **substrate**

[3] the same parameters work well for SiC too.
[4] non-conducting, pyro-electric and piezo-electric material

1. Spin coat the sample (already coated with PMMA) with the conductive polymer espacer 300z: 30 s at 2000 rpm. (No baking needed)
2. Mount the sample in the SEM chamber grounding it by partially covering the surface with copper tape to avoid charge accumulation
3. Expose with: tension 10kV, dose 108 μC/cm^2. Use 5kV to image and find markers if overlay is needed.
4. Remove the espacer 300z: rinse 60 s with deionized water.

A few-nm layer of evaporated Ge can also be used as a conductive layer on top of PMMA, and can be removed by rinsing with deionized water for 2 minutes.
Development
Dip 90s in MIBK:IPA, then dip 60s in IPA to stop the development.

UV mask lithography

For this kind of photolithography we the AZ5214 resist. This resist can be used in both positive processes (where the exposed area of resist is the one that is removed after development) or negative processes (where the initially exposed area is the one that is left after development).
Positive process

1. Spin-coat the sample with AZ5214 at 4000 rpm for 60 s.
2. Bake at 100°C for 90 s on the hotplate.
3. Align the mask and expose for 5 s.

Negative process

1. Steps 1-3 of the positive process.
2. Leave the sample at room temperature for 10 minutes.

3. Bake for 100 s at 115°C on the vacuum hotplate.

4. Expose the entire sample without mask for 21 seconds.

Development
Dip 50s in MIF726, then 60s in water to stop the development.

Laser writer

Also for this photolithography the resist AZ5214 is used. The procedure for standard Si substrates is as follows:

1. Spin coat the sample with AZ5214 at 4000 rpm for 40s.

2. Bake for 90 s at 100°C.

3. Expose, typical parameters: lens 5, gain 14, filter 3, d-step 2.

4. Develop in a mixture of AZ-351 B and water (1:4 in volume) for 40-50 s according to the result.

Lift-off and cleaning

To remove the sacrificial layer dip the sample in acetone until wrinkles appear all over the metal surface (this takes 10-20 minutes according to the sample size). Then squirt some acetone gently on the sample to remove the metal and dip in IPA. Check the result before drying the IPA, and if needed repeat the procedure.
To clean the samples from residues we annealed them for 3 hours in a Mellen furnace at 300° with a 140 ml/min Ar and 28ml/min H_2 flow.

Polymer electrolyte

1. Mix Poly (Ethyl Oxide) (PEO) and $LiClO_4$ powders (Sigma Aldrich), in the weight ratio 1:0.12 in a graduated bottle. Typical values used: 0.2g of PEO, 0.024g of $LiClO_4$
2. Add methanol as a solvent. For the 0.2g of PEO typically used, add $\sim$ 10 ml (7.9 g) of methanol.
3. Ultrasonicate the suspension for 10 minutes.
4. Heat up the mixture to $\sim$ 80-90°C while stirring it with a magnetic bar for 10 minutes.
5. Pour some of the suspension in a small test tube and centrifuge the suspension at 10000 rpm for 5 minutes. The heavier particles deposited at the bottom of the tube are clearly seen as a white layer.
6. Use a pipette to extract the clear liquid from the test tube, and deposit a small drop on the sample. 1.7 μl of liquid produce a drop that is big enough to cover a 5 x 5 mm sample.
7. Heat the sample to 110°C for 5 minutes to evaporate the methanol in excess.

The mixture can be kept in the fridge up to one month and used after repeating steps 3-5 before the deposition on the sample.

Publications

The experimental Chapters of this thesis are based on the following publications:

Chapter 4: Tielrooij, K. J., Orona*, L., Ferrier*, A., Badioli*, M., Navickaite, G., Coop, S., Nanot, S., Kalinic, B., Cesca, T., Gaudreau, L., Ma, Q., Centeno, A., Pesquera, A., Zurutuza Elorza, A., de Riedmatten, H., Goldner, P., García de Abajo, F.J., Jarillo-Herrero, P. & Koppens, F.H.L., Electrical control of optical emitter relaxation pathways enabled by graphene. *Nature Physics* **11**, 281-287, (2015). * equally contributing authors.

Chapter 5: Chen*, J., Badioli*, M., Alonso-Gonzalez*, P., Thongrattanasiri*, S., Huth*, F., Osmond, J., Spasenovič, M., Centeno A., Pesquera A., Godignon P., Zurutuza Elorza, A., Camara, N., García de Abajo, F.J., Hillenbrand, R. & Koppens, F.H.L, Optical nano-imaging of gate-tunable graphene plasmons. *Nature* **487**, 77-81, (2012). * equally contributing authors.

Chapter 7: Konstantatos, G., Badioli, M., Gaudreau, L., Osmond, J., Bernechea, M., de Arquer, F.P.G., Gatti, F. & Koppens, F.H.L., Hybrid graphene-quantum dot phototransistors with ultrahigh gain. *Nature Nanotechnology* **7**, 363-368, (2012).

Chapters 8 and 9: Badioli, M., Woessner, A., Tielrooij, K. J., Nanot, S., Navickaite, G., Stauber, T., García de Abajo, F.J. & Koppens, F.H.L., Phonon-mediated mid-infrared photoresponse of graphene. *Nano letters* **14**,6374-6381, (2014).

Bibliography

A. N. Grigorenko , M. Polini, K.S.N., Graphene plasmonics. *Nat. Photonics* **6**, 749 – 758 (2012).

Abedinpour, S.H., Vignale, G., Principi, A., Polini, M., Tse, W.K. & Macdonald, A.H., Drude weight, plasmon dispersion, and ac conductivity in doped graphene sheets. *Phys. Rev. B - Condens. Matter Mater. Phys.* **84**, 045429 (2011).

Agarwal, G.S., Quantum electrodynamics in the presence of dielectrics and conductors. IV. General theory for spontaneous emission in finite geometries. *Phys. Rev. A* **12**, 1475–1497 (1975).

Allen, S.J., Tsui, D.C. & Logan, R.A., Observation of the two-dimensional plasmon in silicon inversion layers. *Phys. Rev. Lett.* **38**, 980–983 (1977).

Alonso-Gonzalez, P., Nikitin, A.Y., Golmar, F., Centeno, A., Pesquera, A., Velez, S., Chen, J., Navickaite, G., Koppens, F., Zurutuza, A., Casanova, F., Hueso, L.E. & Hillenbrand, R., Controlling graphene plasmons with resonant metal antennas and spatial conductivity patterns. *Science* **344**, 1369–1373 (2014).

Altkorn, R. & Zare, R.N., Effects of saturation on laser-induced fluorescence measurements of population and polarization. *Annu. Rev. Phys. Chem.* **35**, 265–289 (1984).

Amos, R.M. & Barnes, W.L., Modification of the spontaneous emission rate of Eu3+ ions close to a thin metal mirror. *Phys. Rev. B* **55**, 7249–7254 (1997).

Ando, T., Fowler, A.B. & Stern, F., Electronic properties of two-dimensional systems. *Rev. Mod. Phys.* **54**, 437–672 (1982).

Ando, T., Zheng, Y. & Suzuura, H., Dynamical Conductivity and Zero-Mode Anomaly in Honeycomb Lattices. *J. Phys. Soc. Japan* **71**, 1318–1324 (2002).

Andriamiadamanana, C., Ibanez, A., Ferrier, A., Joudrier, A.L., Lombez, L., Liotaud, M., Guillemoles, J.F. & Pellé, F., Erbium-doped yttria thin films prepared by metal organic decomposition for up-conversion. *Thin Solid Films* **537**, 42–48 (2013).

Ashcroft, N.W. & Mermin, N.D., *Solid State Physics*. Harcourt College Publishers, San Diego, 1976.

Babar, S. & Weaver, J.H., Optical constants of Cu , Ag , and Au revisited. *Appl. Opt.* **54**, 477–481 (2015).

Badioli, M., Woessner, A., Tielrooij, K.J., Nanot, S., Navickaite, G., Stauber, T., García de Abajo, F.J. & Koppens, F.H.L., Phonon-Mediated Mid-Infrared Photoresponse of Graphene. *Nano Lett.* **14**, 6374–6381 (2014).

Bae, S., Kim, H., Lee, Y., Xu, X., Park, J.S., Zheng, Y., Balakrishnan, J., Lei, T., Kim, H.R., Song, Y.I., Kim, Y.J., Kim, K.S., Ozyilmaz, B., Ahn, J.H., Hong, B.H. & Iijima, S., Roll–to–roll production of 30–inch graphene films for transparent electrodes. *Nat. Nanotechnol.* **5**, 574–578 (2010).

Barnes, W.L., Topical review Fluorescence near interfaces : the role of photonic mode. *J. Mod. Opt.* **45** (1998).

Barnes, W.L.W.L., Dereux, A. & Ebbesen, T.W.T.W., Surface plasmon subwavelength optics. *Nature* **424**, 824–830 (2003).

Berger, C., Song, Z., Li, T., Li, X., Ogbazghi, A.Y., Feng, R., Dai, Z., Alexei, N., Conrad, M.E.H., First, P.N. & De Heer, W.A., Ultrathin epitaxial graphite: 2D electron gas properties and a route toward graphene-based nanoelectronics. *J. Phys. Chem. B* **108**, 19912–19916 (2004).

Blake, P., Hill, E.W., Castro Neto, a.H., Novoselov, K.S., Jiang, D., Yang, R., Booth, T.J. & Geim, a.K., Making graphene visible. *Appl. Phys. Lett.* **91**, 063124 (2007).

Blanco, L.A. & Garcia de Abajo, F.J., Spontaneous light emission in complex nanostructures. *Phys. Rev. B* **69**, 205414 (2004).

Bohm, D. & Pines, D., A Collective Description of Electron Interactions: III. Coulomb Interactions in a Degenerate Electron Gas. *Phys. Rev.* **92**, 609–625 (1953).

Bonaccorso, F., Sun, Z., Hasan, T. & Ferrari, A.C., Graphene Photonics and Optoelectronics. *Nat. Photonics* **4**, 611–622 (2010).

Bostwick, A., Ohta, T., Seyller, T., Horn, K. & Rotenberg, E., Quasiparticle dynamics in graphene. *Nat. Phys.* **3**, 36–40 (2007).

Brar, V.W., Jang, M.S., Sherrott, M., Lopez, J.J. & Atwater, H.a., Highly confined tunable mid-infrared plasmonics in graphene nanoresonators. *Nano Lett.* **13**, 2541–7 (2013).

Britnell, L., Field-effect tunneling transistor based on vertical graphene heterostructures. *Science* **335**, 947–950 (2012).

Casiraghi, C., Pisana, S., Novoselov, K.S., Geim, a.K. & Ferrari, a.C., Raman fingerprint of charged impurities in graphene. *Appl. Phys. Lett.* **91**, 3 (2007).

Castro Neto, A.H., Guinea, F., Peres, N.M.R., Novoselov, K.S. & Geim, A.K., The electronic properties of graphene. *Rev. Mod. Phys.* **81**, 109–162 (2009).

Cesca, T., Maurizio, C., Kalinic, B., Perotto, G., Mazzoldi, P., Trave, E., Battaglin, G. & Mattei, G., Implantation damage effects on the Erˆ3+ luminescence in silica. *Opt. Express* **20**, 16639 (2012).

Chen, J., Badioli, M., Alonso-González, P., Thongrattanasiri, S., Huth, F., Osmond, J., Spasenović, M., Centeno, A., Pesquera, A., Godignon, P., Zurutuza Elorza, A., Camara, N., de Abajo, F.J.G., Hillenbrand, R. & Koppens, F.H.L., Optical nano-imaging of gate-tunable graphene plasmons. *Nature* **487**, 77–81 (2012).

Chen, J.H., Jang, C., Xiao, S., Ishigami, M. & Fuhrer, M.S., Intrinsic and extrinsic performance limits of graphene devices on SiO2. *Nat. Nanotechnol.* **3**, 206–209 (2008).

Chen, Z., Berciaud, S., Nuckolls, C., Heinz, T.F. & Brus, L.E., Energy transfer from individual semiconductor nanocrystals to graphene. *ACS Nano* **4**, 2964–8 (2010).

Christensen, J., Manjavacas, A., Thongrattanasiri, S., Koppens, F.H.L. & de Abajo, F.J.G., Graphene plasmon waveguiding and hybridization in individual and paired nanoribbons. *ACS Nano* **6**, 431–440 (2012).

Crassee, I., Multicomponent magneto-optical conductivity of multilayer graphene on SiC. *Phys. Rev. B* **84**, 35103 (2011).

Dai, S., Fei, Z., Ma, Q., Rodin, A.S., Wagner, M., McLeod, A.S., Liu, M.K., Gannett, W., Regan, W., Watanabe, K., Taniguchi, T., Thiemens, M., Dominguez, G., Castro Neto, A.H., Zettl, A., Keilmann, F., Jarillo-Herrero, P., Fogler, M.M. & Basov, D.N., Tunable phonon polaritons in atomically thin van der Waals crystals of boron nitride. *Science* **343**, 1125–9 (2014).

Das, A., Pisana, S., Chakraborty, B., Piscanec, S., Saha, S.K., Waghmare, U.V., Novoselov, K.S., Krishnamurthy, H.R., Geim, a.K., Ferrari, A.C. & Sood, A.K., Monitoring dopants by Raman scattering in an electrochemically top–gated graphene transistor. *Nat. Nanotechnol.* **3**, 210–215 (2008).

Das Sarma, S., Adam, S., Hwang, E.H. & Rossi, E., Electronic transport in two-dimensional graphene. *Rev. Mod. Phys.* **83**, 407–470 (2011).

Dawlaty, J.M., Shivaraman, S., Strait, J., George, P., Chandrashekhar, M., Rana, F., Spencer, M.G., Veksler, D. & Chen, Y., Measurement of the optical absorption spectra of epitaxial graphene from terahertz to visible. *Appl. Phys. Lett.* **93**, 131905 (2008).

Dean, C.R., Young, A.F., Meric, I., Lee, C., Wang, L., Sorgenfrei, S., Watanabe, K., Taniguchi, T., Kim, P., Shepard, K.L. & Hone, J., Boron nitride substrates for high-quality graphene electronics. *Nat. Nanotech.* **5**, 722–6 (2010).

Dhoot, A.S., Yuen, J.D., Heeney, M., McCulloch, I., Moses, D. & Heeger, A.J., Beyond the metal-insulator transition in polymer electrolyte gated polymer field-effect transistors. *Proc. Natl. Acad. Sci. U. S. A.* **103**, 11834–7 (2006).

Di Pietro, P., Ortolani, M., Limaj, O., Di Gaspare, a., Giliberti, V., Giorgianni, F., Brahlek, M., Bansal, N., Koirala, N., Oh, S., Calvani, P. & Lupi, S., Observation of Dirac plasmons in a topological insulator. *Nat. Nanotechnol.* **8**, 556–60 (2013).

Di Stefano, O., Fina, N., Savasta, S., Girlanda, R. & Pieruccini, M., Calculation of the local optical density of states in absorbing and gain media. *J. Phys. Condens. Matter* **22**, 315302 (2010).

Dresselhaus, M.S. & Dresselhaus, G., Intercalation compounds of graphite. *Adv. Phys.* **51**, 1–186 (2002).

Eberlein, T., Plasmon spectroscopy of free-standing graphene films. *Phys. Rev. B* **77**, 233406 (2008).

Echtermeyer, T.J., Strong plasmonic enhancement of photovoltage in graphene. *Nat. Commun.* **2**, 458 (2011).

Eckmann, A., Felten, A., Mishchenko, A., Britnell, L., Krupke, R., Novoselov, K.S. & Casiraghi, C., Probing the nature of defects in graphene by Raman spectroscopy. *Nano Lett.* **12**, 3925–30 (2012).

Engel, M., Steiner, M., Lombardo, A., Ferrari, A.C., Löhneysen, H.V., Avouris, P. & Krupke, R., Light-matter interaction in a microcavity-controlled graphene transistor. *Nat. Commun.* **3**, 906 (2012).

Engh, G.V.D. & Farmer, C., Photo-Bleaching and Photon Saturation in Flow Cytometry. *Cytometry* **677**, 669–677 (1992).

Englund, D., Faraon, A., Fushman, I., Stoltz, N., Petroff, P. & Vucković, J., Controlling cavity reflectivity with a single quantum dot. *Nature* **450**, 857–861 (2007).

Englund, D., Fattal, D., Waks, E., Solomon, G., Zhang, B., Nakaoka, T., Arakawa, Y., Yamamoto, Y. & Vučković, J., Controlling the Spontaneous Emission Rate of Single Quantum Dots in a Two-Dimensional Photonic Crystal. *Phys. Rev. Lett.* **95**, 013904 (2005).

Falkovsky, L.A., Optical properties of graphene. *J. Phys. Conf. Ser.* **129**, 012004 (2008).

Falkovsky, L.A. & Pershoguba, S., Optical far-infrared properties of graphene monolayer and multilayers. *Phys. Rev. B* **0**, 9 (2007).

Falkovsky, L.A. & Varlamov, A.A., Space-time dispersion of graphene conductivity. *Eur. Phys. J. B* **56**, 281–284 (2007).

Fang, H., Bechtel, H.A., Plis, E., Martin, M.C., Krishna, S., Yablonovitch, E. & Javey, A., Quantum of optical absorption in two-dimensional semiconductors. *Proc. Natl. Acad. Sci. U. S. A.* **110**, 11688–91 (2013a).

Fang, Z., Thongrattanasiri, S., Schlather, A., Liu, Z., Ma, L., Wang, Y., Ajayan, P.M., Nordlander, P., Halas, N.J. & García De Abajo, F.J., Gated tunability and hybridization of localized plasmons in nanostructured graphene. *ACS Nano* **7**, 2388–2395 (2013b).

Fang, Z., Wang, Y., Liu, Z., Schlather, A., Ajayan, P.M., Koppens, F.H.L., Nordlander, P. & Halas, N.J., Plasmon-induced doping of graphene. *ACS Nano* **6**, 10222–8 (2012).

Fasolino, A., Los, J.H. & Katsnelson, M.I., Intrinsic ripples in graphene. *Nat. Mater.* **6**, 858–861 (2007).

Fei, Z., Andreev, G.O., Bao, W., Zhang, L.M., S McLeod, A., Wang, C., Stewart, M.K., Zhao, Z., Dominguez, G., Thiemens, M., Fogler, M.M., Tauber, M.J., Castro-Neto, A.H., Lau, C.N., Keilmann, F. & Basov, D.N., Infrared nanoscopy of dirac plasmons at the graphene-SiO2 interface. *Nano Lett.* **11**, 4701–4705 (2011).

Fei, Z., Rodin, A.S., Andreev, G.O., Bao, W., McLeod, A.S., Wagner, M., Zhang, L.M., Zhao, Z., Thiemens, M., Dominguez, G., Fogler, M.M., Neto, A.H.C., Lau, C.N., Keilmann, F., Basov, D.N., Castro Neto, A.H., Lau, C.N., Keilmann, F., Basov, D.N. & Castro-Neto, A.H., Gate-tuning of graphene plasmons revealed by infrared nano-imaging. *Nature* **487**, 82–85 (2012).

Fei, Z., Rodin, A.S., Gannett, W., Dai, S., Regan, W., Wagner, M., Liu, M.K., McLeod, A.S., Dominguez, G., Thiemens, M., Castro Neto, A.H., Keilmann, F., Zettl, A., Hillenbrand, R., Fogler, M.M. & Basov, D.N., Electronic and plasmonic phenomena at graphene grain boundaries. *Nat. Nanotechnol.* **8**, 821–825 (2013).

Ferrari, A. & Al., Science and technology roadmap for graphene, related two-dimensional crystals, and hybrid systems. *Nanoscale* **7**, 4598–4810 (2015).

Ferrari, A. & Robertson, J., Interpretation of Raman spectra of disordered and amorphous carbon. *Phys. Rev. B* **61**, 14095–14107 (2000).

Ferrari, A.C., Raman spectroscopy of graphene and graphite: Disorder, electron–phonon coupling, doping and nonadiabatic effects. *Solid State Commun.* **143**, 47–57 (2007).

Ferrari, A.C. & Basko, D.M., Raman spectroscopy as a versatile tool for studying the properties of graphene. *Nat. Nanotechnol.* **8**, 235–46 (2013).

Ferrari, A.C., Meyer, J.C., Scardaci, V., Casiraghi, C., Lazzeri, M., Mauri, F., Piscanec, S., Jiang, D., Novoselov, K.S., Roth, S. & Geim, A.K., Raman spectrum of graphene and graphene layers. *Phys. Rev. Lett.* **97**, 187401 (2006).

Fetter, A.L. & Walecka, J.D., *Quantum Theory of Many-Particle Systems*. Dover Publications, Inc, 2003.

Frank, O., Tsoukleri, G., Riaz, I., Papagelis, K., Parthenios, J., Ferrari, A.C., Geim, A.K., Novoselov, K.S. & Galiotis, C., Development of a universal stress sensor for graphene and carbon fibres. *Nat. Commun.* **2**, 255 (2011).

Fratini, S. & Guinea, F., Substrate-limited electron dynamics in graphene. *Phys. Rev. B* **77**, 195415 (2008).

Freitag, M., Low, T. & Avouris, P., Increased responsivity of suspended graphene photodetectors. *Nano Lett.* **13**, 1644–1648 (2013a).

Freitag, M., Low, T., Martin-Moreno, L., Zhu, W., Guinea, F. & Avouris, P., Substrate-sensitive mid-infrared photoresponse in graphene. *ACS Nano* **8**, 8350–6 (2014).

Freitag, M., Low, T., Xia, F. & Avouris, P., Photoconductivity of biased graphene. *Nat. Photon.* **7**, 53–59 (2012).

Freitag, M., Low, T., Zhu, W., Yan, H., Xia, F. & Avouris, P., Photocurrent in graphene harnessed by tunable intrinsic plasmons. *Nat. Commun.* **4**, 1951 (2013b).

Furchi, M., Urich, A., Pospischil, A., Lilley, G., Unterrainer, K., Detz, H., Klang, P., Andrews, A.M., Schrenk, W., Strasser, G. & Mueller, T., Microcavity-integrated graphene photodetector. *Nano Lett.* **12**, 2773–7 (2012).

Gabor, N.M., Song, J.C.W., Ma, Q., Nair, N.L., Taychatanapat, T., Watanabe, K., Taniguchi, T., Levitov, L.S. & Jarillo-Herrero, P., Hot carrier-assisted intrinsic photoresponse in graphene. *Science* **334**, 648–52 (2011).

Gan, X., Shiue, R.J., Gao, Y., Meric, I., Heinz, T.F., Shepard, K., Hone, J., Assefa, S. & Englund, D., Chip-integrated ultrafast graphene photodetector with high responsivity. *Nat. Photonics* **7**, 883–887 (2013).

Gansen, E.J., Photon-number-discriminating detection using a quantum-dot, optically gated, field-effect transistor. *Nat. Photon.* **1**, 585–588 (2007).

García de Abajo, F.J., Graphene Plasmonics: Challenges and Opportunities. *ACS Photonics* **1**, 135–152 (2014).

Gaudreau, L., Tielrooij, K.J., Prawiroatmodjo, G.E.D.K., Osmond, J., De Abajo, F.J.G. & Koppens, F.H.L., Universal distance-scaling of nonradiative energy transfer to graphene. *Nano Lett.* **13**, 2030–2035 (2013).

Geim, A.K. & Novoselov, K.S., The rise of graphene. *Nat. Mater.* **6**, 183–191 (2007).

Gell-Mann, M. & Brueckner, K.A., Correlation Energy of an Electron Gas at High Density. *Phys. Rev.* **106**, 364–368 (1957).

George, P.A., Strait, J., Dawlaty, J., Shivaraman, S., Chandrashekhar, M., Rana, F. & Spencer, M.G., Ultrafast optical-pump terahertz-probe spectroscopy of the carrier relaxation and recombination dynamics in epitaxial graphene. *Nano Lett.* **8**, 4248–4251 (2008).

Gérard, J., Sermage, B., Gayral, B., Legrand, B., Costard, E. & Thierry-Mieg, V., Enhanced Spontaneous Emission by Quantum Boxes in a Monolithic Optical Microcavity. *Phys. Rev. Lett.* **81**, 1110–1113 (1998).

Giannini, V., Fernández-Domínguez, A.I., Sonnefraud, Y., Roschuk, T., Fernández-García, R. & Maier, S.a., Controlling light localization and light-matter interactions with nanoplasmonics. *Small* **6**, 2498–2507 (2010).

Gibertini, M., Tomadin, A., Guinea, F., Katsnelson, M.I. & Polini, M., Electron-hole puddles in the absence of charged impurities. *Phys. Rev. B - Condens. Matter Mater. Phys.* **85**, 1–5 (2012).

Glauber, R.J. & Lewenstein, M., Quantum optics of dielectric media. *Phys. Rev. A* **43**, 467–491 (1991).

Gómez-Santos, G. & Stauber, T., Fluorescence quenching in graphene: A fundamental ruler and evidence for transverse plasmons. *Phys. Rev. B* **84**, 165438 (2011).

Grimes, C.C. & Adams, G., Observation of Two-Dimensional Plasmons and Electron-Ripplon Scattering in a Sheet of Electrons on Liquid Helium. *Phys. Rev. Lett.* **36**, 145–148 (1976).

Gusynin, V.P. & Sharapov, S.G., Transport of Dirac quasiparticles in graphene: Hall and optical conductivities. *Phys. Rev. B - Condens. Matter Mater. Phys.* **73** (2006).

Hass, J., Feng, R., Li, T., Li, X., Zong, Z., de Heer, W.A., First, P.N., Conrad, E.H., Jeffrey, C.A. & Berger, C., Highly ordered graphene for two dimensional electronics. *Appl. Phys. Lett.* **89**, 143106 (2006).

Hecht, B., Bielefeldt, H., Novotny, L., Inouye, Y. & Pohl, D.W., Local excitation, scattering, and interference of surface plasmons. *Phys. Rev. Lett* **77**, 1889–1892 (1996).

Hennessy, K., Badolato, A., Winger, M., Gerace, D., Atature, M., Gulde, S., Falt, S., Hu, E.L. & Imamoglu, A., Quantum nature of a strongly-coupled single quantum dot-cavity system. *Nature* **445**, 14 (2006).

Herring, P.K., Hsu, A.L., Gabor, N.M., Shin, Y.C., Kong, J., Palacios, T. & Jarillo-Herrero, P., Photoresponse of an electrically tunable ambipolar graphene infrared thermocouple. *Nano Lett.* **14**, 901–7 (2014).

Hillenbrand, R., Taubner, T. & Keilmann, F., Phonon-enhanced light matter interaction at the nanometre scale. *Nature* **418**, 159–62 (2002).

Huang, M., Yan, H., Chen, C., Song, D., Heinz, T.F. & Hone, J., Phonon softening and crystallographic orientation of strained graphene studied by Raman spectroscopy. *Proc. Natl. Acad. Sci. U. S. A.* **106**, 7304–8 (2009).

Hwang, E. & Das Sarma, S., Acoustic phonon scattering limited carrier mobility in two-dimensional extrinsic graphene. *Phys. Rev. B* **77**, 115449 (2008).

Hwang, E.H. & Das Sarma, S., Dielectric function, screening, and plasmons in two-dimensional graphene. *Phys. Rev. B* **75**, 205418 (2007).

Hwang, E.H., Sarma, S.D. & Das Sarma, S., Surface polar optical phonon interaction induced many-body effects and hot-electron relaxation in graphene. *Phys. Rev. B* **87**, 115432 (2013).

Hwang, H.Y., Iwasa, Y., Kawasaki, M., Keimer, B., Nagaosa, N. & Tokura, Y., Emergent phenomena at oxide interfaces. *Nat. Mater.* **11**, 103–13 (2012).

Jablan, M., Buljan, H., Soljačić, M. & Soljacic, M., Plasmonics in graphene at infrared frequencies. *Phys. Rev. B* **80**, 245435 (2009).

Jablan, M., Soljacic, M. & Buljan, H., Plasmons in Graphene: Fundamental Properties and Potential Applications. *Proc. IEEE* **101**, 1689–1704 (2013).

Jiang, C., Shalygin, V.A., Panevin, V.Y., Danilov, S.N., Glazov, M.M., Yakimova, R., Lara-Avila, S., Kubatkin, S. & Ganichev, S.D., Helicity-dependent photocurrents in graphene layers excited by midinfrared radiation of a CO_{2} laser. *Phys. Rev. B* **84**, 125429 (2011).

Ju, L., Geng, B., Horng, J., Girit, C., Martin, M., Hao, Z., Bechtel, H.A., Liang, X., Zettl, A., Shen, Y.R. & Wang, F., Graphene plasmonics for tunable terahertz metamaterials. *Nat. Nanotechnol.* **6**, 630–634 (2011).

Khrapach, I., Withers, F., Bointon, T.H., Polyushkin, D.K., Barnes, W.L., Russo, S. & Craciun, M.F., Novel highly conductive and transparent graphene-based conductors. *Adv. Mater.* **24**, 2844–2849 (2012).

Kim, K.S., Zhao, Y., Jang, H., Lee, S.Y., Kim, J.M., Kim, K.S., Ahn, J.h., Kim, P., Choi, J.Y. & Hong, B.H., Large–scale pattern growth of graphene films for stretchable transparent electrodes. *Nature* **457**, 706–710 (2009).

Kischkat, J., Peters, S., Gruska, B., Semtsiv, M., Chashnikova, M., Klinkmüller, M., Fedosenko, O., Machulik, S., Aleksandrova, A., Monastyrskyi, G., Flores, Y. & Masselink, W.T., Mid-infrared optical properties of thin films of aluminum oxide, titanium dioxide, silicon dioxide, aluminum nitride, and silicon nitride. *Appl. Opt.* **51**, 6789–98 (2012).

Klekachev, A.V., Electron accumulation in graphene by interaction with optically excited quantum dots. *Phys. E* **43**, 1046–1049 (2011).

Kliewer, K.L. & Fuchs, R., Optical Modes of Vibration in an Ionic Crystal Slab Including Retardation. I. Nonradiative Region. *Phys. Rev.* **144**, 495–503 (1966).

Konstantatos, G., Ultrasensitive solution-cast quantum dot photodetectors. *Nature* **442**, 180–183 (2006).

Konstantatos, G., Hybrid graphene-quantum dot phototransistors with ultrahigh gain. *Nat. Nanotech.* **7**, 363–368 (2012).

Konstantatos, G., Levina, L., Fischer, A. & Sargent, E.H., Engineering the temporal response of photoconductive photodetectors via selective introduction of surface trap states. *Nano Lett.* **8**, 1446–1450 (2008).

Konstantatos, G. & Sargent, E.H., Nanostructured materials for photon detection. *Nat. Nanotech.* **5**, 391–400 (2010).

Koppens, F.H.L., Chang, D.E. & García de Abajo, F.J., Graphene plasmonics: a platform for strong light-matter interactions. *Nano Lett.* **11**, 3370–3377 (2011).

Koppens, F.H.L., Mueller, T., Avouris, P., Ferrari, A.C., Vitiello, M.S. & Polini, M., Photodetectors based on graphene, other two-dimensional materials and hybrid systems. *Nat. Publ. Gr.* **9**, 780–793 (2014).

Kuzmenko, A.B., van Heumen, E., Carbone, F. & van der Marel, D., Universal optical conductance of graphite. *Phys. Rev. Lett.* **100**, 117401 (2008).

Lamprecht, B., Leitner, A. & Aussenegg, F., SHG studies of plasmon dephasing in nanoparticles. *Appl. Phys. B Lasers Opt.* **68**, 419–423 (1999).

Lee, E.J.H., Balasubramanian, K., Weitz, R.T., Burghard, M. & Kern, K., Contact and edge effects in graphene devices. *Nat. Nanotechnol.* **3**, 486–90 (2008).

Lee, J.S., Kovalenko, M.V., Huang, J., Chung, D.S. & Talapin, D.V., Band-like transport, high electron mobility and high photoconductivity in all-inorganic nanocrystal arrays. *Nat. Nanotech.* **6**, 348–352 (2011).

Lemme, M.C., Koppens, F.H.L., Falk, A.L., Rudner, M.S., Park, H., Levitov, L.S. & Marcus, C.M., Gate-activated photoresponse in a graphene p-n junction. *Nano Lett.* **11**, 4134–7 (2011).

Lendrem, B.A.D., Lendrem, D.W., Gray, A. & Isaacs, J.D., CHRISTMAS 2014 : GOING TO EXTREMES The Darwin Awards : sex differences in idiotic behaviour. *BMJ* **349**, g7094 (2014).

Leu, L.Y., Gardner, J.T. & Forrest, S.R., A high gain, high bandwidth In0.53Ga0.47As/InP heterojunction phototransistor for optical communications. *J. Appl. Phys.* **69**, 1052–1062 (1991).

Li, D., Quantifying and controlling the magnetic dipole contribution to 1.5 um light emission in erbium-doped yttrium oxide. *Phys. Rev. B* **89**, 161409(R) (2014).

Li, X., Cai, W., An, J., Kim, S., Nah, J., Yang, D., Piner, R., Velamakanni, A., Jung, I., Tutuc, E., Banerjee, S.K., Colombo, L. & Ruoff, R.S., Large-area synthesis of high-quality and uniform graphene films on copper foils. *Science* **324**, 1312–4 (2009).

Li, Z.Q., Henriksen, E.A., Jiang, Z., Hao, Z., Martin, M.C., Kim, P., Stormer, H.L. & Basov, D.N., Dirac charge dynamics in graphene by infrared spectroscopy. *Nat. Phys.* **4**, 532–535 (2008).

Liu, C.H., Chang, Y.c., Norris, T.B. & Zhong, Z., Graphene photodetectors with ultra-broadband and high responsivity at room temperature. *Nat. Nanotechnol.* **9**, 273–8 (2014a).

Liu, N., Tian, H., Schwartz, G., Tok, J.B.H., Ren, T.L. & Bao, Z., Large-area, transparent, and flexible infrared photodetector fabricated using P-N junctions formed by N-doping chemical vapor deposition grown graphene. *Nano Lett.* **14**, 3702–3708 (2014b).

Liu, Y., Plasmon resonance enhanced multicolour photodetection by graphene. *Nat. Commun.* **2**, 579 (2011).

Liu, Y., Willis, R., Emtsev, K. & Seyller, T., Plasmon dispersion and damping in electrically isolated two-dimensional charge sheets. *Phys. Rev. B* **78**, 201403(R) (2008).

Lodahl, P., Floris Van Driel, A., Nikolaev, I.S., Irman, A., Overgaag, K., Vanmaekelbergh, D. & Vos, W.L., Controlling the dynamics of spontaneous emission from quantum dots by photonic crystals. *Nature* **430**, 654–7 (2004).

Low, T. & Avouris, P., Graphene plasmonics for terahertz to mid-infrared applications. *ACS Nano* **8**, 1086–1101 (2014).

Low, T., Perebeinos, V., Kim, R., Freitag, M. & Avouris, P., Cooling of photoexcited carriers in graphene by internal and substrate phonons. *Phys. Rev. B* **86**, 045413 (2012).

Lu, C., Fu, Q., Huang, S. & Liu, J., Polymer Electrolyte-Gated Carbon Nanotube Field-Effect Transistor. *Nano Lett.* **4**, 623–627 (2004).

Lui, C.H., Li, Z., Chen, Z., Klimov, P.V., Brus, L.E. & Heinz, T.F., Imaging stacking order in few-layer graphene. *Nano Lett.* **11**, 164–9 (2011).

Maier, S.a. & Atwater, H.a., Plasmonics: Localization and guiding of electromagnetic energy in metal/dielectric structures. *J. Appl. Phys.* **98**, 1–10 (2005).

Mak, K.F., Sfeir, M.Y., Wu, Y., Lui, C.H., Misewich, J.A. & Heinz, T.F., Measurement of the Optical Conductivity of Graphene. *Phys. Rev. Lett.* **101**, 196405 (2008).

Mak, K.F., Shan, J. & Heinz, T.F., Seeing many-body effects in single- and few-layer graphene: Observation of two-dimensional saddle-point excitons. *Phys. Rev. Lett.* **106**, 046401 (2011).

Martin, J., Akerman, N., Ulbricht, G., Lohmann, T., Smet, J.H., von Klitzing, K. & Yacoby, A., Observation of electron–hole puddles in graphene using a scanning single–electron transistor. *Nat. Phys.* **4**, 144–148 (2007).

Meric, I., Han, M.Y., Young, A.F., Ozyilmaz, B., Kim, P. & Shepard, K.L., Current saturation in zero–bandgap, top–gated graphene field-effect transistors. *Nat. Nanotechnol.* **3**, 654–9 (2008).

Mermin, N.D., Crystalline order in two dimensions. *Phys. Rev.* **176**, 250–254 (1968).

Meyer, J.C., Geim, A.K., Katsnelson, M.I., Novoselov, K.S., Booth, T.J. & Roth, S., The structure of suspended graphene sheets. *Nature* **446**, 60–63 (2007).

Mohiuddin, T., Lombardo, A., Nair, R., Bonetti, A., Savini, G., Jalil, R., Bonini, N., Basko, D., Galiotis, C., Marzari, N., Novoselov, K., Geim, A. & Ferrari, A., Uniaxial strain in graphene by Raman spectroscopy: G peak splitting, Grüneisen parameters, and sample orientation. *Phys. Rev. B* **79**, 205433 (2009).

Mueller, T., Xia, F. & Avouris, P., Graphene photodetectors for high-speed optical communications. *Nat. Photon.* **4**, 297–301 (2010).

Mueller, T., Xia, F., Freitag, M., Tsang, J. & Avouris, P., Role of contacts in graphene transistors: A scanning photocurrent study. *Phys. Rev. B - Condens. Matter Mater. Phys.* **79**, 245430 (2009).

Nair, R.R., Blake, P., Grigorenko, a.N., Novoselov, K.S., Booth, T.J., Stauber, T., Peres, N.M.R. & Geim, a.K., Fine structure constant defines visual transparency of graphene. *Science* **320**, 1308 (2008).

Ni, Z.H., Wang, H.M., Kasim, J., Fan, H.M., Yu, T., Wu, Y.H., Feng, Y.P. & Shen, Z.X., Graphene thickness determination using reflection and contrast spectroscopy. *Nano Lett.* **7**, 2758–63 (2007).

Ni, Z.H., Yu, T., Lu, Y.H., Wang, Y.Y., Feng, Y.P. & Shen, Z.X., Uniaxial strain on graphene: Raman spectroscopy study and band-gap opening. *ACS Nano* **2**, 2301–5 (2008).

Nicol, E.J. & Carbotte, J.P., Optical conductivity of bilayer graphene with and without an asymmetry gap. *Phys. Rev. B - Condens. Matter Mater. Phys.* **77**, 1–11 (2008).

Nikitin, A.Y., Guinea, F., Garcia-Vidal, F.J. & Martin-Moreno, L., Fields radiated by a nanoemitter in a graphene sheet. *Phys. Rev. B* **84**, 195446 (2011).

Nikitin, A.Y., Guinea, F., Garcia-Vidal, F.J. & Martin-Moreno, L., Surface plasmon enhanced absorption and suppressed transmission in periodic arrays of graphene ribbons. *Phys. Rev. B - Condens. Matter Mater. Phys.* **85**, 081405 (2012).

Nikitin, A.Y., Low, T. & Martin-Moreno, L., Anomalous reflection phase of graphene plasmons and its influence on resonators. *Phys. Rev. B - Condens. Matter Mater. Phys.* **90**, 041407 (2014).

Novoselov, K.S., Geim, A.K., Morozov, S.V., Jiang, D., Katsnelson, M.I., Grigorieva, I.V., Dubonos, S.V. & Firsov, A.A., Two-Dimensional Gas of Massless Dirac Fermions in Graphene. *Nature* **438**, 197–200 (2005a).

Novoselov, K.S., Geim, A.K., Morozov, S.V., Jiang, D., Zhang, Y., Dubonos, S.V., Grigorieva, I.V. & Firsov, A.A., Electric field effect in atomically thin carbon films. *Science* **306**, 666–669 (2004).

Novoselov, K.S., Jiang, D., Schedin, F., Booth, T.J., Khotkevich, V.V., Morozov, S.V. & Geim, a.K., Two–dimensional atomic crystals. *Proc. Natl. Acad. Sci. U. S. A.* **102**, 10451–10453 (2005b).

Novotny, L. & Hecht, B., *Principles of Nano-Optics*. Cambridge Unversity Press, 2006.

Novotny, L. & van Hulst, N.F., Antennas for light. *Nat. Photon.* **5**, 83–90 (2011).

Ocelic, N., Huber, A. & Hillenbrand, R., Pseudoheterodyne detection for background-free near-field spectroscopy. *Appl. Phys. Lett.* **89**, 101124 (2006).

Ogura, M., Hole injection type InGaAs-InP near infrared photo-FET (HI-FET). *IEEE J. Quantum Electron.* **46**, 562–569 (2010).

Olbrich, P., Drexler, C., Golub, L.E., Danilov, S.N., Shalygin, V.a., Yakimova, R., Lara-Avila, S., Kubatkin, S., Redlich, B., Huber, R. & Ganichev, S.D., Reststrahl band-assisted photocurrents in epitaxial graphene layers. *Phys. Rev. B* **88**, 245425 (2013).

Ozel, T., Gaur, A., Rogers, J.a. & Shim, M., Polymer electrolyte gating of carbon nanotube network transistors. *Nano Lett.* **5**, 905–911 (2005).

Palik, E.D., *Handbook of Optical Constants of Solids*. Elsevier, New York, 1997.

Park, J., Ahn, Y.H. & Ruiz-Vargas, C., Imaging of photocurrent generation and collection in single-layer graphene. *Nano Lett.* **9**, 1742–1746 (2009).

Pattantyus-Abraham, A.G., Kramer, I.J., Barkhouse, A.R., Wang, X., Konstantatos, G., Debnath, R., Levina, L., Raabe, I., Nazeeruddin, M.K., Grätzel, M. & Sargent, E.H., Depleted-heterojunction colloidal quantum dot solar cells. *ACS Nano* **4**, 3374–80 (2010).

Polman, A., Erbium implanted thin film photonic materials. *J. Appl. Phys.* **82**, 1 (1997).

Pospischil, A., CMOS-compatible graphene photodetector covering all optical communication bands. *Nat. Photon.* **7**, 892–896 (2013).

Principi, A., Carrega, M., Lundeberg, M.B., Woessner, A., Koppens, F.H.L., Vignale, G. & Polini, M., Plasmon losses due to electron-phonon scattering: the case of graphene encapsulated in hexagonal Boron Nitride. *Phys. Rev. B* **90**, 14 (2014).

Principi, A., Vignale, G., Carrega, M. & Polini, M., Impact of disorder on Dirac plasmon losses. *Phys. Rev. B* **88**, 121405 (2013a).

Principi, A., Vignale, G., Carrega, M. & Polini, M., Intrinsic lifetime of Dirac plasmons in graphene. *Phys. Rev. B* **88**, 195405 (2013b).

Purcell, E.M., Spontaneous emission probabilities at radio frequencies. *Phys.Rev.* **69**, 681 (1946).

Raimond, J.M., Brune, M. & Haroche, S., Colloquium: Manipulating quantum entanglement with atoms and photons in a cavity. *Rev. Mod. Phys.* **73**, 565–582 (2001).

Reich, S., Maultzsch, J., Thomsen, C. & Ordejón, P., Tight-binding description of graphene. *Phys. Rev. B* **66**, 035412 (2002).

Roddaro, S., Pingue, P., Piazza, V., Pellegrini, V. & Beltram, F., The optical visibility of graphene: interference colors of ultrathin graphite on SiO2. *Nano Lett.* **7**, 2707–10 (2007).

Rodrigo, D., Limaj, O., Janner, D., Etezadi, D., Garcia de Abajo, F.J., Pruneri, V. & Altug, H., Mid-infrared plasmonic biosensing with graphene. *Science* **349**, 165–168 (2015).

Rose, A., *Concepts in Photoconductivity and Allied Problems*. Robert E. Krieger Publishing, 1978.

Schall, D., Neumaier, D., Mohsin, M., Chmielak, B., Bolten, J., Porschatis, C., Prinzen, A., Matheisen, C., Kuebart, W., Junginger, B., Templ, W., Giesecke, A.L. & Kurz, H., 50 GBit/s Photodetectors Based on Wafer-Scale Graphene for Integrated Silicon Photonic Communication Systems. *ACS Photonics* **1**, 781–784 (2014).

Scharf, B., Perebeinos, V., Fabian, J. & Avouris, P., Effects of optical and surface polar phonons on the optical conductivity of doped graphene. *Phys. Rev. B* **87**, 035414 (2013).

Schneider, G.F., Calado, V.E., Zandbergen, H., Vandersypen, L.M.K. & Dekker, C., Wedging transfer of nanostructures. *Nano Lett.* **10**, 1912–6 (2010).

Shields, A.J., Detection of single photons using a field-effect transistor gated by a layer of quantum dots. *Appl. Phys. Lett.* **76**, 3673–3675 (2000).

Sirringhaus, H., Kawase, T., Friend, R.H., Shimoda, T., Inbasekaran, M., Wu, W. & Woo, E.P., High-resolution Inkjet Printing of All- Transistor Circuits. *Science* **290**, 2123–2126 (2000).

Slonczewski, J. & Weiss, P., Band Structure of Graphite. *Phys. Rev.* **109**, 272–279 (1958).

Snoeks, E., Lagendijk, A. & Polman, A., Measuring and modifying the spontaneous emission rate of erbium near an interface. *Phys. Rev. Lett.* **74**, 2459–2462 (1995).

Song, J.C.W., Rudner, M.S., Marcus, C.M. & Levitov, L.S., Hot carrier transport and photocurrent response in graphene. *Nano Lett.* **11**, 4688–4692 (2011).

Stauber, T., Noriega-Pérez, D. & Schliemann, J., Universal absorption of two-dimensional systems. *Phys. Rev. B* **91**, 115407 (2015).

Stauber, T., Peres, N.M.R. & Geim, a.K., Optical conductivity of graphene in the visible region of the spectrum. *Phys. Rev. B* **78**, 085432 (2008).

Sun, Z., Infrared photodetectors based on CVD-grown graphene and PbS quantum dots with ultrahigh responsivity. *Adv. Mater.* **24**, 5878–5883 (2012).

Swathi, R.S. & Sebastian, K.L., Resonance energy transfer from a dye molecule to graphene. *J. Chem. Phys.* **129**, 054703 (2008).

Tan, P.H., Han, W.P., Zhao, W.J., Wu, Z.H., Chang, K., Wang, H., Wang, Y.F., Bonini, N., Marzari, N., Pugno, N., Savini, G., Lombardo, A. & Ferrari, A.C., The shear mode of multilayer graphene. *Nat. Mater.* **11**, 294–300 (2012).

Tan, Y.W., Zhang, Y., Stormer, H.L. & Kim, P., Temperature dependent electron transport in graphene (2007).

Thomsen, C. & Reich, S., Double Resonant Raman Scattering in Graphite. *Phys. Rev. Lett.* **85**, 5214–5217 (2000).

Tielrooij, K.J., Massicotte, M., Piatkowski, L., Woessner, A., Ma, Q., Jarillo-Herrero, P., van Hulst, N.F. & Koppens, F.H.L., Hot-carrier photocurrent effects at grapheneâĂŞmetal interfaces. *J. Phys. Condens. Matter* **27**, 164207 (2015a).

Tielrooij, K.J., Orona, L., Ferrier, A., Badioli, M., Navickaite, G., Coop, S., Nanot, S., Kalinic, B., Cesca, T., Gaudreau, L., Ma, Q., Centeno, A., Pesquera, A., Zurutuza, A., de Riedmatten, H., Goldner, P., García de Abajo, F.J., Jarillo-Herrero, P. & Koppens, F.H.L., Electrical control of optical emitter relaxation pathways enabled by graphene. *Nat. Phys.* **11**, 1–7 (2015b).

Treossi, E., Melucci, M., Liscio, A., Gazzano, M., Samorì, P. & Palermo, V., High-contrast visualization of graphene oxide on dye-sensitized glass, quartz, and silicon by fluorescence quenching. *J. Am. Chem. Soc.* **131**, 15576–7 (2009).

Tsui, D.C., Stormer, H.L. & Gossard, A.C., Two-Dimensional Magnetotransport in the Extreme Quantum Limit. *Phys. Rev. Lett.* **48**, 1559–1562 (1982).

Urich, A., Unterrainer, K. & Mueller, T., Intrinsic response time of graphene photodetectors. *Nano Lett.* **11**, 2804–2808 (2011).

Vakil, A. & Engheta, N., Transformation optics using graphene. *Science* **332**, 1291–1294 (2011).

Velizhanin, K.A. & Efimov, A., Probing plasmons in graphene by resonance energy transfer. *Phys. Rev. B* **84**, 085401 (2011).

Velizhanin, K.A. & Shahbazyan, T.V., Long-range plasmon-assisted energy transfer over doped graphene. *Phys. Rev. B* **86**, 245432 (2012).

Visscher, K., Brakenhoff, G.J. & Visser, T.D., Fluorescence saturation in confocal microscopy. *J. Microsc.* **175**, 162–165 (1994).

Vollmerhausen, R.H., Driggers, R.G. & Hodgkin, V.A., Night illumination in the near- and short-wave infrared spectral bands and the potential for silicon and indium-gallium-arsenide imagers to perform night targeting. *Opt. Eng.* **52**, 043202 (2013).

Wallace, P.R., The band theory of graphite. *Phys. Rev.* **71**, 622–634 (1947).

Wang, L., Meric, I., Huang, P.Y., Gao, Q., Gao, Y., Tran, H., Taniguchi, T., Watanabe, K., Campos, L.M., Muller, D.A., Guo, J., Kim, P., Hone, J., Shepard, K.L. & Dean, C.R., One–dimensional electrical contact to a two–dimensional material. *Science* **342**, 614–7 (2013).

Wang, S. & Mahan, G., Electron Scattering from Surface Excitations. *Phys. Rev. B* **6**, 4517–4524 (1972).

Wei, P., Bao, W., Pu, Y., Lau, C. & Shi, J., Anomalous Thermoelectric Transport of Dirac Particles in Graphene. *Phys. Rev. Lett.* **102**, 166808 (2009).

Woessner, A., Lundeberg, M.B., Gao, Y., Principi, A., Alonso-González, P., Carrega, M., Watanabe, K., Taniguchi, T., Vignale, G., Polini, M., Hone, J.,

Hillenbrand, R. & Koppens, F.H.L., Highly confined low-loss plasmons in graphene–boron nitride heterostructures. *Nat. Mater.* **14**, 421–425 (2014).

Wright, P.D., Nelson, R.J. & Cella, T., High-gain InGaAsP-InP heterojunction phototransistors. *Appl. Phys. Lett.* **37**, 192–194 (1980).

Wunsch, B., Stauber, T., Sols, F. & Guinea, F., Dynamical polarization of graphene at finite doping. *New J. Phys.* **8**, 318 (2006).

Xia, F., Mueller, T., Golizadeh-Mojarad, R., Freitage, M., Lin, Y.M., Tsang, J., Perebeinos, V. & Avouris, P., Photocurrent imaging and efficient photon detection in a graphene transistor. *Nano Lett.* **9**, 1039–1044 (2009a).

Xia, F., Mueller, T., Lin, Y.m., Valdes-Garcia, A. & Avouris, P., Ultrafast graphene photodetector. *Nat. Nanotechnol.* **4**, 839–843 (2009b).

Xu, X., Gabor, N.M., Alden, J.S., van der Zande, A.M. & McEuen, P.L., Photothermoelectric effect at a graphene interface junction. *Nano Lett.* **10**, 562–566 (2010).

Xue, J., Sanchez-Yamagishi, J., Bulmash, D., Jacquod, P., Deshpande, A., Watanabe, K., Taniguchi, T., Jarillo-Herrero, P. & LeRoy, B.J., Scanning tunnelling microscopy and spectroscopy of ultra-flat graphene on hexagonal boron nitride. *Nat. Mater.* **10**, 282–285 (2011).

Yan, H., Low, T., Zhu, W., Wu, Y., Freitag, M., Li, X., Guinea, F., Avouris, P. & Xia, F., Damping pathways of mid-infrared plasmons in graphene nanostructures. *Nat. Photonics* **7**, 394–399 (2013).

Yan, H., Xia, F., Zhu, W., Freitag, M., Dimitrakopoulos, C., Bol, A.A., Tulevski, G. & Avouris, P., Infrared spectroscopy of wafer-scale graphene. *ACS Nano* **5**, 9854–9860 (2011).

Yan, J., Kim, M.h., Elle, J.A., Sushkov, A.B., Jenkins, G.S., Milchberg, H.M., Fuhrer, M.S. & Drew, H.D., Dual-gated bilayer graphene hot-electron bolometer. *Nat. Nanotechnol.* **7**, 472–8 (2012).

Yan, J., Zhang, Y., Kim, P. & Pinczuk, A., Electric field effect tuning of electron-phonon coupling in graphene. *Phys. Rev. Lett.* **98**, 166802 (2007).

Yao, Y., Shankar, R., Rauter, P., Song, Y., Kong, J., Loncar, M. & Capasso, F., High-responsivity mid-infrared graphene detectors with antenna-enhanced photocarrier generation and collection. *Nano Lett.* **14**, 3749–54 (2014).

Yu, W.J., Highly efficient gate-tunable photocurrent generation in vertical heterostructures of layered materials. *Nat. Nanotech.* **8**, 952–958 (2013).

Yu, Y.J., Zhao, Y., Ryu, S., Brus, L.E., Kim, K.S. & Kim, P., Tuning the graphene work function by electric field effect. *Nano Lett.* **9**, 3430–4 (2009).

Zhang, W., Chuu, C.P., Huang, J.K., Chen, C.H., Tsai, M.L., Chang, Y.H., Liang, C.T., Chen, Y.Z., Chueh, Y.L., He, J.H., Chou, M.Y. & Li, L.J., Ultrahigh-gain photodetectors based on atomically thin graphene-MoS2 heterostructures. *Sci. Rep.* **4**, 3826 (2014).

Zhang, Y., Tan, Y.W., Stormer, H.L. & Kim, P., Experimental observation of the quantum Hall effect and Berry's phase in graphene. *Nature* **438**, 201–4 (2005).

Zhou, W., Atomically localized plasmon enhancement in monolayer graphene. *Nat. Nanotechnol* **7**, 161–165 (2012).

Ziegler, K., Minimal conductivity of graphene: Nonuniversal values from the Kubo formula. *Phys. Rev. B* **75**, 233407 (2007).

Zuev, Y., Chang, W. & Kim, P., Thermoelectric and Magnetothermoelectric Transport Measurements of Graphene. *Phys. Rev. Lett.* **102**, 96807 (2009).